# Molecular Mechanisms Determining Bacterial Cell Shape:

# Role of Cardiolipin

by

**Ti-Yu Lin**

A dissertation submitted in partial fulfillment

of the requirements for the degree of

Doctor of Philosophy

(Biochemistry)

at the

UNIVERSITY OF WISCONSIN - MADISON

2018

Date of final oral examination: 05/25/2018

This dissertation is approved by the following members of the Final Oral Committee:
Qiang Cui, Professor, Chemistry
Timothy J. Donohue, Professor, Bacteriology
David J. Pagliarini, Associate Professor, Biochemistry
Alessandro Senes, Associate Professor, Biochemistry
Douglas B. Weibel, Professor, Biochemistry, Chemistry, Biomedical Engineering

# TABLE OF CONTENTS

# Acknowledgements

A decade has passed since I made up my mind to go to graduate school. Before coming to the U.S., I had meet a lot of wonderful people that helped me prepare for the challenging graduate life. I would like to thank Dr. Shyh-Jye Lee and Dr. Chien-Yuan Pan for their advices and encouragement in my rugged pre-graduate life as a research assistant. I thank Ming-Shan Chien for being such a great mentor and selflessly teaching me the skills to perform molecular cloning. I thank Dr. Yu-Ling Shih for teaching me the techniques to investigate protein-lipid interactions and inciting my interest in the study of membrane biology. I thank Borran Li and Chien-Wei Chen for introducing me to the research of biosensor development. I would also like to thank Ami Shih and Hui-Hsing Hung for their solid friendship that helped me get through the tough times during my early research career in Taiwan.

I was fortunate to begin my graduate life on such a vibrant campus at the UW-Madison filled with a school pride that I've never experienced before. I would like to thank my advisor Doug Weibel for seeing my potential and recruiting me to the school, which had allowed me to start a new page of my life in a different country. I enjoy pursuing my Ph.D. with Doug, who has been a supportive and inspiring mentor. Doug always gave me the freedom to explore my scientific interests and encouraged me to learn new skills essential for my future. Under his supervision, I can always envision the endless opportunities in science.

I would also like to thank my committee member: Drs. Qiang Cui, Tim Donohue, Dave Pagliarini, Alessandro Senes for their input in the annual meetings over the years. I am especially grateful to Dr. Tim Donohue and Wayne Kontur for sharing their expertise in *Rhodobacter sphaeroides*. I also thank Dr. Alessandro Senes for his advice on my seminar presentation and future career. Thank you all for your support. Your knowledge, guidance, and insights have made this dissertation possible.

I enjoy working with all the members in the Weibel lab throughout my graduate years. Friday evening hangout on the terrace with you guys will remain imprinted on my memory. I am particularly thankful to my mentor Thiago Santos for introducing me to the lab and teaching me how to study microbiology. I thank George Auer for his technical assistance with peptidoglycan experiments. I am also grateful to Sandy Tseng, Na Yin, Matt Stilwell, Rishi Trivedi, and Julia Nepper for their friendship and all the fun time playing foosball. Thank you all for making my graduate life an enjoyable journey.

I am extremely lucky to have Will Gross and Landen Nickel as my undergraduate students. Working with you guys has been a mutual learning experience. I especially appreciate Will's help with some of the most critical experiments in this dissertation. I am impressed by your dedication to science and am glad to see you growing up into a young scientist. I am also thankful to you for all the conversation lessons that you offered. Those really helped improving my English. Thank you for your company in the last year of my graduate life.

I wouldn't have gone this far without the support from my family. Despite the culture of “silent gratitude” in our family, I would like to take this chance to “say” thank you. I am grateful to my parents for their education and encouragement whenever I feel confused about stuff in my life. I also appreciate your support for my decision of not going to medical school. I would like to thank my siblings for growing up and being friends with me. We have been through lots of hard and good times together in our childhood. I also thank you for taking care of mom and dad when I am chasing my dream far away from home. Again, I am grateful beyond words.

Finally, I would like to thank my kindly grandparents. Thank you for always being proud of me on every accomplishment I’ve made. I am regretful that I was not able to make this one earlier. But, I can feel you somewhere and would like to dedicate this dissertation to you.

# Molecular Mechanisms Determining Bacterial Cell Shape:
# Role of Cardiolipin

Ti-Yu Lin

Under the supervision of Douglas B. Weibel, Ph.D.

Department of Biochemistry

University of Wisconsin-Madison, Madison, WI

Bacteria exhibit a variety of shapes, including: cocci, bacilli, and spirochetes. Cell shape influences the spatial and temporal dynamics of processes that are essential for growth and replication in bacteria and is connected to pathogenicity and evasion of the mammalian immune system. Several bacterial cell-shape determinants have been proposed, including: 1) the cytoskeleton as an internal scaffolding, and 2) the peptidoglycan layer of the cell wall that resists osmotic pressure and maintains cell shape. However, some bacteria lack these subcellular components and yet retain distinct cellular shapes. This observation raises the question of whether bacteria use other shape-determining strategies and provides an opportunity to explore the biochemical evolution of cell shape across bacteria. The phospholipid membrane is another cellular structure that may regulate the shape of bacteria, and yet the impact of this cellular structure on bacterial morphology has been largely overlooked. Bacterial cell membranes consist of the three major families of phospholipids: phosphatidylethanolamine is zwitterionic, and phosphatidylglycerol and cardiolipin are anionic. The composition of cell membranes plays a fundamental role in bacterial cell biology. This dissertation describes how cardiolipin regulates cell morphology and influences bacterial adaptation to environmental stress. We observed that a cardiolipin deficiency in *Rhodobacter sphaeroides* changes the shape of cells and impairs biofilm formation. We demonstrated that cardiolipin participates in bacterial cell shape determination by regulating peptidoglycan precursor biosynthesis. In this dissertation, we also developed a new method for optimizing the production of recombinant proteins in *Escherichia coli* by engineering its cell shape. The insights gained from these studies will enable a wide range of applications spanning the identification of novel antibiotic targets and the optimization of biomaterials production by bacterial cells.

# CHAPTER 1

# Introduction to organization and function of anionic phospholipids in bacteria

This chapter was adapted from:

Ti-Yu Lin and Douglas B. Weibel. Organization and function of anionic phospholipids in bacteria. Applied Microbiology and Biotechnology, 100 (10), 4255-4267, 2016

# ABSTRACT

In addition to playing a central role as a permeability barrier for controlling the diffusion of molecules and ions in and out of bacterial cells, phospholipid (PL) membranes regulate the spatial and temporal position and function of membrane proteins that play an essential role in a variety of cellular functions. Based on the very large number of membrane-associated proteins encoded in genomes, an understanding of the role of PLs may be central to understanding bacterial cell biology. This area of microbiology has received considerable attention over the past two decades, and the local enrichment of anionic PLs has emerged as a candidate mechanism for biomolecular organization in bacterial cells. In this review, we summarize the current understanding of anionic PLs in bacteria, including their biosynthesis, subcellular localization, and physiological relevance, discuss evidence and mechanisms for enriching anionic PLs in membranes, and conclude with an assessment of future directions for this area of bacterial biochemistry, biophysics, and cell biology.

# INTRODUCTION

Bacterial membranes primarily consist of phospholipids (PLs) that contain a hydrophilic phosphate head group and two hydrophobic acyl chains (tails). The amphipathic characteristic of PLs is responsible for their formation of bilayer structures in aqueous environments that create a physical barrier and localize and concentrate molecules and materials within cells (i.e., in the cytoplasm) from the extracellular environment. Bacteria synthesize a diverse collection of PLs that differ in the number and length of acyl chains, the number, position, and geometry of unsaturated bonds, and the structure, polarity, and charge of head groups. Figure 1 depicts chemical structures of the three major families of PLs in bacterial membranes: phosphatidylethanolamine (PE) is zwitterionic, and phosphatidylglycerol (PG) and cardiolipin (CL) are anionic. In addition to the major PLs listed above, bacteria produce additional PLs that are less prevalent, including phosphatidylcholine (PC) and phosphatidylinositol (PI), and a spectrum of lipids that lack phosphorus, such as ornithine (OL) and sulfoquinovosyl diacylglycerol (SQDG) (1).

The Gram staining technique is a fundamental method for differentiating bacteria, classifies cells according to cell wall structure, and reveals that the majority of bacteria separate into two large groups. Gram-positive bacteria contain a cytoplasmic membrane surrounded by a thick (~30-100-nm thick) layer of peptidoglycan; in contrast, gram-negative bacteria contain two distinct bilayer membranes—the cytoplasmic and outer membrane—surrounding a thin layer of peptidoglycan (~3-5-nm thick) (Figure 2). The cytoplasmic membrane of gram-positive bacteria generally contains lipoteichoic acids, PG, and CL. In contrast, the cytoplasmic membrane of gram-negative bacteria is primarily composed of PE, PG, and CL. The outer membrane and cytoplasmic membranes of gram-negative bacteria have a similar phospholipid profile; the primary difference between the two membranes is the presence of lipopolysaccharides in the outer membrane (1, 2).

Several lines of experimental evidence support PL heterogeneity in bacterial membranes and a connection between lipid composition and biomolecular function (3, 4). Concentrated regions of anionic PLs in membranes have been hypothesized to sort proteins into different regions in bacterial cells and regulate a variety of processes, including: ATP synthesis, chromosomal replication, cell division, protein translocation across membranes, DNA repair, and cell shape determination (5-12). There are conceptual parallels between this phenomena and 'lipid rafts' in eukaryotic membranes, in which local differences in lipid concentration are hypothesized to arise from the formation of phase-ordered regions that sort proteins and localize cellular processes (13). The characterization of mechanisms underlying the formation of localized regions of anionic PLs and their physiological relevance in bacteria is an active area of research. In this review, we provide a current outlook of the biosynthesis, localization, and function of anionic PLs in bacterial cells, discuss what remains unknown, and provide suggestions for next steps in this field.

## Biosynthesis of bacterial anionic PLs

Figure 3 highlights the common biosynthetic pathways for the major anionic PLs in bacteria (i.e., PG and CL). In most bacteria, cytidine diphosphate-diacylglycerol (CDP-DAG) is the precursor of anionic PLs and is formed by incorporating cytidine triphosphate (CTP) into phosphatidic acid (PA) through CDP-DAG synthase (CdsA). CDP-DAG can be converted to either PE or PG and CL through two distinct pathways. In the pathway to PE, phosphatidylserine synthase (PssA) converts CDP-DAG to PS using L-serine as the phosphatidyl acceptor, and phosphatidylserine decarboxylase (PsdA) decarboxylates PS to form PE. In the pathway to PG and CL, PG synthase (PgsA) catalyzes the transfer of the phosphatidyl group from CDP-DAG to glycerol-3-phosphate (G3P) to form PG phosphate (PGP), which is subsequently dephosphorylated by phosphatidylglycerophosphate phosphatase (Pgp) to produce PG. CL synthase (Cls) catalyzes the condensation of two PG molecules to form CL. A family of Cls enzymes have been classified into prokaryotic and eukaryotic types. In contrast to the mechanisms for CL synthesis in most bacteria, eukaryotic cells synthesize CL through a CDP-DAG-dependent Cls that uses CDP-DAG as the phosphatidyl donor and PG as the acceptor. This “eukaryotic-like” Cls has recently been identified in many actinobacteria, including *Streptomyces coelicolor* (14).

Many bacteria possess a single version of PgsA. Knocking out *cls* and detecting that CL was still present indicated that some bacteria contain multiple isoforms of Cls. For example, three Cls have been identified in *Escherichia coli*; ClsA, ClsB, and ClsC show sequence homology and contain two phospholipase D domains, which represent a characteristic biochemical feature of bacterial Cls. ClsA produces CL in the log phase and stationary phase, while ClsB and ClsC only synthesize CL in the stationary phase. Similar to the Cls enzymes in other bacteria, ClsA and ClsB synthesize CL from two molecules of PG. In contrast, ClsC catalyzes the formation of CL by transferring a phosphatidyl moiety from PE to PG (15). *E. coli* PssA catalyzes the formation of PS, contains a phospholipase D domain, and is hypothesized to have Cls activity; however this hypothesis is untested, and an *E. coli* Δ*clsABC* mutant does not produce any detectable CL, thereby making this concept unlikely (15, 16). *Staphylococcus aureus* contains two Cls isoforms—referred to as Cls1 and Cls2—that synthesize CL from two molecules of PG. Cls2 contributes the majority of CL produced by *S. aureus* during growth in both log and stationary phase as measured by thin-layer chromatography (TLC). No CL synthesis is detected when both *cls1* and *cls2* are deleted (17, 18).

Bacteria maintain the compositional balance between zwitterionic and anionic PLs in membranes by biochemically regulating the two families of PL synthases. Table 1 summarizes the major PL compositions in the membranes of widely studied model bacteria. In *E. coli*, the membrane composition is balanced by a feedback mechanism between the PssA−PsdA and PgsA−Pgp pathways: PssA is a peripheral membrane protein that enzymatically synthesizes PS and is activated by interacting with PG and CL in the membrane. PsdA performs the enzymatic step for conversion of PS to PE. As the concentration of PE in the membrane increases due to the

PssA−PsdA pathway, the membrane association and activity of PssA decreases, which slows the rate of PE production, thereby accelerating the rate of PG/CL formation through the PgsA−Pgp pathway. This feedback mechanism enables the cell to control the PL composition in membranes (19-21).

The concentrations of anionic PLs in bacterial membranes vary in response to growth phase, salinity, pH, osmolality, and organic solvents (15, 18, 22-28). The overall CL concentration in bacterial membranes can vary by a factor of ~2; for example the concentration of CL can increase by ~200% as cells enter stationary phase compared to cells in the log phase of cell growth (15). *S. aureus* cells generally have an increase in their CL content after they are engulfed by neutrophils (18). Changes in Cls enzyme activity or its expression level alters the amount of CL in the membrane and these mechanisms are hypothesized to be important for bacterial adaptation to environmental stress. In vitro enzyme assays using purified *E. coli* Cls suggest that its activity is product inhibited and thereby regulated by CL concentration (29). Product inhibition of Cls may play an important role in regulating CL synthesis under normal growth conditions (i.e., in the absence of extracellular stress).

### Subcellular distribution of anionic PLs in bacterial membranes

The fluid mosaic model of the membrane was originally formulated upon the model of PLs distributed homogeneously (30), and has been modified to account for observations of PL domains in cell membranes. Several studies have demonstrated the presence of lateral PL heterogeneity or PL domains in bacterial membranes (3). For example, the segregation of PE and PG into different domains in *E. coli* membranes was demonstrated utilizing the biophysical properties of pyrene–lipid probes (31). Several fluorescent lipophilic probes display a heterogeneous distribution in mycobacterial cells, reflecting lateral PL heterogeneity in membranes (32).

The anionic PL-specific fluorescent dye 10-N-nonyl acridine orange (NAO) has been used to visualize anionic PL-enriched membrane domains. NAO is hypothesized to bind to anionic PLs through: (i) an electrostatic interaction between the positive charge on the acridine amino moiety and the negative phosphate groups of anionic PLs; and (ii) hydrophobic interactions between the hydrophobic region of the acridine ring and the aliphatic region of the bilayer (33). CL was proposed to orient NAO such that excitation produces an excimer that red-shifts the emission wavelength of the fluorophore (for NAO bound to CL, $\lambda$ex,max=474 nm, and $\lambda$em,max=640 nm; for NAO bound to other anionic PLs, $\lambda$ex,max=495 nm and $\lambda$em,max=525 nm) (33, 34). This spectroscopic signature was widely applied to characterizing CL in bacteria and mitochondria. For example, the accumulation of the red-shifted fluorescence signal at the cell poles and division septum in NAO-treated rod-shaped bacteria led to the hypothesis that CL is concentrated at these regions of the membrane (35, 36). In *Bacillus subtilis* cells, regions of similar fluorescence were observed in engulfment membranes and forespore membranes during sporulation and attributed to CL localization (36). The polar localization of

CL was verified in a dye-independent manner using *E. coli* strains with point mutations in the MinC, MinD, or MinE proteins that produced minicells with membranes that largely represented the polar regions of the cell due to misplacement of the division site. Quantifying the PL compositions in the membranes of minicells (poles) and vegetative cells (whole cells) using TLC and mass spectrometry demonstrated that CL is concentrated at the cell poles (37, 38).

A recent study demonstrated that NAO binds promiscuously to all anionic PLs in vitro, including PG, CL, PS, and PA, and displays spectroscopic changes (i.e., the 'diagnostic' red shift) previously considered to be unique for the interaction between NAO and CL (38). Cells of the triple *cls* knockout *E. coli* strain BKT12—containing no measurable CL by mass spectrometry—treated with NAO retained red-shifted fluorescence localized at the cell poles and septa. Presumably another member(s) of the anionic PL family is enriched at these regions of the cells. Mass spectrometric analysis of *E. coli* minicells demonstrated that the polar membranes are enriched in PG and CL and contain small amounts of different anionic PLs. Removing CL (e.g., in *E. coli* strain BKT12), increased the concentration of polarly localized PG (Figure 4).

PG has been hypothesized to form spiral structures in membranes that extend along the long axis of *B. subtilis* cells based on the pattern of the fluorescent lipophilic dye FM4-64, which is a cationic styryl compound that has been suggested to preferentially associate with anionic PLs (39). The spiral lipid structures are absent in cells lacking PG; however, a recent study suggests that this is likely due to depolarization of the membrane potential and the FM dye may not be an indicator for PG (40). The absence of spiral patterns of FM4-64 localization in *B. subtilis* protoplasts and cells depleted of MurG suggests that they may be connected to peptidoglycan assembly and structure (41). Spiral PL domains have not been observed in *E. coli;* however, FM dyes display a heterogeneous pattern of membrane labeling (42). The interaction between FM4-64 and specific PLs has yet to be determined at a level of detail that enables the conclusively determination of the observations of cells labeled with this fluorophore.

## Mechanisms of localizing anionic PLs

### *Clustering of CL*

CL was first isolated from bovine heart and its structure was determined in a complex with the photoreaction center in *Rhodobacter sphaeroides* using X-ray crystallography (43). The volume of the CL head group is small relative to the volume occupied by its four large acyl tails, creating a large intrinsic negative curvature ($-1.3\ nm^{-1}$) and influencing the structure, physical properties, and dynamics of the membrane. A recent study of planar supported lipid bilayers (SLBs) suggests that CL induces double bilayers or nonlamellar structures having a large local mean curvature (44). The same study also found that CL increases the fluidity and decreases the mechanical stability of planar SLBs probably through decreasing the packing of PLs in membranes. CL can also cause local curvature changes in the membrane of giant unilamellar vesicles (45). In the presence of divalent cations, CL forms a hexagonal phase with a curvature of ~ -1.3 nm$^{-1}$ due to the interaction of cations with the phosphate groups on CL (46). Divalent cations also bind to the head group of PE and produce a curvature of ~ -0.48 nm$^{-1}$ (47). Atomic force microscopy imaging of planar SLBs indicates that CL and PE can self-associate into domains that differ in height from the rest of the membrane, thereby illustrating the role of the intrinsic curvature of PLs in the formation of membrane domains (48-50).

Computational model has been used to explain the preferential localization of CL at the cell poles in rod-shaped bacteria by considering the large osmotic pressure across the cell wall arising due to the mismatch in the concentration of solutes inside and outside of bacterial cells. One model suggests that the large osmotic pressure (~3-5 kPa) (51) pins the cytoplasmic membrane (bilayer stiffness of ~20 $k_BT$) (52) against the stiff layer of peptidoglycan (stiffness of ~25-45 MPa) (53) that surrounds the cytoplasmic cell membrane, thereby creating elastic strain that is stored in the membrane (54, 55). In this model, short-range interactions between molecules of CL create small domains that localize at regions of the membrane with largest negative mean curvature (e.g., the poles), dissipate the elastic strain on the membrane, and reduce the surface energy potential imposed by bending the bilayer. Because of its large negative curvature, CL is hypothesized to preferentially localize in the inner leaflet of the cytoplasmic membrane and concentrate at the polar membranes due to the enhanced curvature of these cellular regions relative to the cylindrical mid-cell. A repulsion arising from the osmotic force pinning the membrane to the cell wall prevents CL from forming large aggregates. Instead, CL forms finite sized domains that are large enough to reduce membrane elastic stress and localize at the cell poles. In agreement with the curvature model, several studies have demonstrated the relationship between curvature and CL localization (56, 57). This model also predicts a critical concentration for the microphase separation of CL below which the entropy of lipid mixing prevents the formation of CL domains, which is consistent with an observation that CL is not concentrated at the cell poles of a *clsA* deletion strain of *E. coli* with reduced CL concentration (24). One caveat to these studies is that CL localization was indirectly measured using NAO, and recent studies indicate that this fluorophore may not distinguish between different anionic PLs (38); consequently, membrane localization of CL domains may partially or entirely consist of other anionic PLs. An aggregation-induced emission-active fluorophore with high selectivity to CL versus other mitochondrial membrane PLs has been reported; however, this probe has yet to be tested in bacteria (58).

### *Interactions of PLs with proteins*

Labeling *B. subtilis* cells with the PE-specific fluorescent cyclic peptide Ro09-0198 (Ro) leads to the accumulation of fluorescence at regions of the cell with the largest mean curvature (i.e., poles, septa and forespores) (59). Although PE favors membranes with a negative curvature (47), the curvature-mediated mechanism proposed above is not sufficient to explain the cellular localization of PE due to its small intrinsic curvature. Similarly, the model is insufficient to explain the polar/septal localization of PG that occurs in cells of *E. coli* strain BKT12 (i.e., lacking

CL), as PG has a smaller curvature than PE (~-0.1 $nm^{-1}$ for PG) (60). The curvature-based model provides a model for explaining the preferential localization of CL in rod-shaped bacteria; however, a caveat to this model is that one osmotic-mechanical model suggests that the cytoplasm and periplasm are isoosmotic and that the relevant osmotic pressure in bacteria primarily occurs between the periplasm and the extracellular space (61). In this model, the difference in solute concentration in the cytoplasm and periplasm is insufficient to create a large force to pin the cytoplasmic membrane against the peptidoglycan layer. In addition, the curvature model is not applicable to cocci-shaped bacteria in which membrane curvature is the same throughout the cell. Membrane domains enriched in anionic PLs have been observed in the spherical bacterium *Streptococcus pyogenes* using NAO (62), suggesting that other mechanisms and strategies are involved in localizing anionic PLs to specific regions of cells.

The interaction of proteins with specific PLs provides another mechanism for concentrating lipids in membranes. One possible hypothesis is that membrane domain formation in bacteria is triggered by the coupled transcription-translation-insertion (transertion) of proteins into membranes (63). This hypothesis is based on the transertion of membrane proteins occurring at a high frequency (64) and many integral membrane proteins (e.g., ATP synthase, NADH dehydrogenase) that have been characterized to bind to specific PLs (e.g., PG, CL) (65, 66). As a result, compact membrane regions (domains) enriched in specific proteins and PLs are formed. As predicted by the model, drugs (e.g., rifampicin, chloramphenicol, puromycin) that interfere the transertion process of membrane proteins cause dissipation of membrane domains (67).

In principal, peripheral membranes proteins can also trigger the formation of PL domains through the interaction of charged residues in the proteins and PLs. An example in support of this hypothesis is the phase separation of CL in model membranes induced by mitochondrial creatine kinase (68). Creatine kinase contains clusters of cationic residues that interact with CL, neutralize membrane charge, and reduce the electrostatic repulsion between negatively charged head groups on anionc PLs, thereby promoting the concentration of CL into domains. Another example is the cationic antimicrobial peptide Ltc1 isolated from the Latarcin family, which induces PG domain formation in model bacterial membranes (69). A recent study provides evidence that the peripheral membrane protein MreB induces PL domains along the cylindrical walls of rod-shaped bacteria based on the protein binding to the membrane (40). This study suggests that the length of acyl chains is responsible for the formation of PL domains—likely arising from the energetics of chain packing—however, the mechanism underlying this protein-lipid interaction remains unsolved. Several groups have demonstrated that the positioning of MreB in rod-shaped bacterial cells is curvature dependent (57, 70). Despite uncertainty regarding the mechanisms involved in PL localization, the existence of PL domains in bacterial membranes has gained strong traction through biophysical and optical measurements. These regions of the membrane provide specialized environments for the function of membrane proteins. Although the historic view of bacteria is that they do not contain subcellular compartments for organizing biomolecules, membrane heterogeneity and other structural features of cells may instead provide this function.

## Functional roles of anionic PLs

### *ATP synthesis*

CL is found in archaea, bacteria and eukarya and its head group contains two phosphate groups with different pKa values ($pKa_1 = 2.8$ and $pKa_2 = 7.5\text{-}9.5$). CL is reported to have a net charge of -1 at physiological pH because the second phosphate gets protonated and forms an intra-molecular hydrogen bond with the hydroxyl group of the central glycerol moiety (71). CL is an essential component of energy-transducing membranes as it can serve as a proton trap for energy-transducing complexes that create and operate off of the cellular ΔpH. In addition, CL interacts tightly with energy-transducing complexes in membranes, fills clefts at the interface between proteins and membranes, and stabilizes protein complexes and regulates their function (5). CL has been observed to bind to several bacterial proteins in X-ray structures, including the *R. sphaeroides* bacterial reaction center (43), and *R. sphaeroides* cytochrome *c* oxidase (C*c*O) (72), *E. coli* formate dehydrogenase (73), and *E. coli* succinate dehydrogenase (74). Compared to other PLs, CL more effectively restores the activity of several purified respiratory complexes, such as lactate dehydrogenase (75), NADH dehydrogenase (65), succinate dehydrogenase (76), and nitrate reductase (NarGHI) (77). Although the interaction of CL and these energy-transducing complexes is considered to be essential for their assembly and function, this dependency has not yet been established in vivo. A previous study of the NarGHI complex demonstrated that a PE-deficient mutant of *E. coli* that contains a high level of anionic PLs has enhanced NarGHI activity (77). The dependence of NarGHI binding to CL on the protein structure and function may also be applicable to other respiratory complexes. However, a previous study demonstrated that a CL deficiency in *R. sphaeroides* does not impair the structure and function of C*c*O or cause significant growth defects (72). Hence, it remains unclear whether CL is essential for the structure and function of these complexes of bacterial respiratory proteins.

### *Chromosomal replication*

Anionic PLs play a role in chromosomal replication by regulating DnaA (6). An *E. coli* strain deficient in anionic PLs has impaired growth and inhibited chromosomal replication with a concomitant reduction in the amount of cellular DNA (78). Anionic PLs bind DnaA through electrostatic interactions and are proposed to promote the conversion of ADP-DnaA to ATP-DnaA, which binds to *oriC* and initiates the replication of DNA at the mid-cell. After transcriptional initiation, the origin moves towards the cell poles and anionic PLs inhibit the interaction of DnaA and *oriC*, thus preventing the re-initiation of chromosomal replication. CL is the most effective of the anionic PLs at promoting the conversion of ADP-DnaA to ATP-DnaA and inhibiting the DnaA-*oriC* interaction (79-83). This crosstalk between DnaA and anionic PLs assures initiation occurs only once per cell cycle. DnaA forms helical structures along the longitudinal axis of *E. coli* cells (84). It remains unclear how anionic PLs that accumulate at polar/septal regions assist in defining the subcellular localization of DnaA and the DNA replication site.

*Protein translocation*

The subcellular distribution of anionic PLs provides a mechanism for positioning the protein translocon. The Sec machinery is reportedly organized into spiral-like structures in *B. subtilis* that disappear in a strain depleted of PG. PG increases the ATPase activity of SecA and forms spiral structures in *B. subtilis*, suggesting that PG may determine the subcellular sites for exporting proteins through the SecA-YEG pathway in this bacterium (85, 86). In contrast, the Sec translocon in *S. pyogenes* forms a single ExPortal membrane domain for protein secretion that is enriched in PG (62). In gram-negative bacteria the subcellular localization of the Sec machinery appears to be CL-dependent. The *Vibrio cholera* Eps system exports cholera toxin across the outer membrane and localizes at the cell poles. CL interacts with the EpsE/EpsL complex and stimulates its ATPase activity through stabilizing the oligomerization state of EpsE (87). In *E. coli,* CL binds tightly to the SecYEG protein complex, stabilizes its dimeric form, and stimulates the ATPase activity of SecA. The SecYEG complex is arranged in spiral-like structures in *E. coli* cells. SecYEG spirals are observed less frequently in a CL deficient strain, suggesting that the spatial distribution of the *E. coli* protein translocon relies on CL

(8). The connection between CL, its organization at the cell poles, and protein export remains a puzzle.

*Cell division*

Anionic PLs have been hypothesized to play an important role in determining the cell division site by regulating the subcellular distribution of FtsA and MinD. Both of these proteins contain an amphipathic helix enriched in positively charged amino acids and preferentially interact with anionic PLs, in particular CL (7, 88). FtsA is a bacterial homolog of eukaryotic actin that recruits the bacterial tubulin homolog FtsZ to the membrane, where it polymerizes into a ring structure (Z-ring) and creates a constriction force at the division site. MinD is a component of the Min system that prevents the placement of the Z-ring at the cell poles. After its association with the *E. coli* membrane, MinD polymerizes into a dynamic helical structure that attaches to MinC and oscillates between the cell poles. MinC is a FtsZ inhibitor that prevents Z-ring formation. MinE is another component of the *E. coli* Min system that interacts with MinD and promotes its ATP hydrolysis activity, resulting in detachment of MinD from the membrane. MinE interacts with the membrane through an N-terminal helix that has a preference for binding to anionic PLs, especially for CL (89, 90). MinD and MinE have differential affinities for binding to anionic PLs that may affect their retention times on the membrane (91, 92). In a model of the Min system, MinE forms a ring structure (E-ring) near the mid-cell and confines the MinCD complex to the polar regions of the cell, enabling Z-ring formation at the mid-cell (93). Anionic PL domains may play a role in MinD nucleation at the cell poles and stabilize the ring structure of MinE and FtsA/FtsZ at the septal region of the cell (94) In support of this model, a recent study demonstrated that the dynamic oscillation of MinCDE proteins can be reconstituted in an artificial cell-shaped compartment in which a negatively charged membrane containing PG or CL was required to create protein gradients that position FtsZ at the middle of the cell-like compartment (95).

MinD does not oscillate between the *B. subtilis* cell poles; instead, it co-localizes with PG spirals positioned along the long axis of the cell (39). Similar to MinD, FtsA/FtsZ is also reported to form helical structures that are positioned along the length of cells (96). During cell division, the DivIVA/MinJ complex—that is functionally synonymous to MinE in *E. coli*—recruits MinCD to the cell poles, enabling Z-ring formation at the mid-cell (97, 98). Polar localization of DivIVA depends on negative membrane curvature of the cell poles instead of CL domains (99, 100).

### *Adaptation to environmental stress*

A growing body of evidence suggests that anionic PLs play a fundamental role in the adaptation of bacteria to environmental stress. For example, CL accumulates in *E. coli* cells in response to osmotic stress and promotes the polar localization of ProP, an osmosensory transporter that senses a high osmolality and regulates the concentrations of organic osmolytes in the cytoplasm. In a CL-deficient strain, the localization of ProP to the cell poles is reduced, causing impaired growth of this mutant under osmotic stress (24, 101). The requirement of CL for osmoadaptation has been found in other bacteria, including *R. sphaeroides* (102), *S. aureus* (22) and *B. subtilis* (28). The concentration of CL also increases when bacterial cells enter the stationary phase of growth or low-pH environments. Cells deficient in CL have reduced survival under stress conditions. It has been suggested that bacteria require additional energy to grow in the presence of environmental stress and an increase in the amount of CL may enhance the activity of respiratory complexes and increase ATP production. Recent studies have found that the PhoPQ system transports CL from the cytoplasmic membrane to the outer membrane in the gastrointestinal pathogen *Salmonella typhimurium*, during its response to a decrease in pH and the presence of cationic antimicrobial peptides in the hosts. An increase in CL in the outer membrane may contribute to constructing the barrier necessary for bacterial survival within host tissues (103, 104). Recent studies demonstrate that anionic PLs facilitate DNA repair by stabilizing RecA filament bundles in *E. coli* (9), the concentration of CL in *R. sphaeroides* cells correlates with their shape and plays an important role in forming biofilms (10), and that a CL-deficient mutant of *Pseudomonas putida* is susceptible to several antibiotics (105). These data suggest that anionic PLs enable bacteria to adapt to changes in their environments and survive.

## Future directions

Several decades of studies have demonstrated that anionic PLs play roles in bacterial functions. These lipids appear to provide mechanisms of positioning and regulating biochemical machinery in cells, which can be viewed as having some similarities to the function of organelles in eukaryotic cells. Among the anionic PLs, CL has a unique molecular shape and high binding affinity for many proteins that plays an important role in regulating the position and function of proteins in cells. Bacterial strains lacking CL are stable and do not display any growth or obvious physiological abnormalities, suggesting that this PL is not essential (106). Several studies have demonstrated that PG can override the absence of CL in *E. coli* and restore the interaction of proteins with the membrane (25, 38, 107). It is possible that different families of anionic PLs provide a mechanism of redundancy; a *pgsA* null *E. coli* strain lacking PG and CL (UE54) remains viable, yet only if the outer membrane lipoprotein is mutated or removed. NAO labeled cells of strain UE54 display fluorescence at the polar/septal regions of cells, indicative of concentrated regions of anionic PLs. Analysis of PL composition of UE54 minicells demonstrated that the anionic PLs N-acyl-PE and PA are enriched at the cell poles (108). Polar localization of PG, PA, and N-acyl-PE in bacteria suggests that they maintain the anionic character of polar membranes in the absence of CL. It remains unclear whether these anionic PLs have interchangeable functions in regulating bacterial biochemistry. In vitro studies using liposomes or planar SLBs containing different anionic PLs may be useful in understanding their effects on the structure and function of bacterial proteins.

CL is a major component of the inner membrane of mitochondria and plays an important role in the function of a range of proteins in mitochondrial energy-transducing membranes. CL has been suggested to cluster into domains and interacts with ATP synthase at the apex of mitochondrial cristae (109). In addition, CL binds the mitofilin/MINOS protein complex at the mitochondrial cristae junctions (110). The localization of CL at these highly curved membrane regions may provide a mechanism for controlling mitochondrial cristae morphology. In support of this hypothesis, a *Saccharomyces cerevisiae* mutant lacking CL shows an aberrant morphology of mitochondrial cristae (109). Large changes in membrane shape and the formation of membrane invaginations are also observed in bacteria. Photosynthetic bacteria such as *R. sphaeroides* form intracytoplasmic membranes (ICMs)—by delamination of the cytoplasmic membrane from the peptidoglycan layer of the cell wall—and accommodate the photosynthetic apparatus (111). Membrane invaginations can also be induced by overexpression of several membrane proteins in *E. coli*, including the ATP synthase. Interestingly, *E. coli* intracellular membranes are enriched in CL (112). An understanding of the physiological, biochemical, and biophysical mechanisms underlying membrane internalization in bacteria and its connection to the organization of anionic PLs may provide insight into the endosymbiotic theory of mitochondria evolving from $\alpha$-proteobacteria.

# ACKNOWLEDGMENTS

T.-Y. Lin acknowledges a Dr. James Chieh-Hsia Mao Wisconsin Distinguished Graduate Fellowship from the Department of Biochemistry, University of Wisconsin-Madison. Research in this area of our lab is supported by the National Science Foundation (under award DMR-1121288), the National Institutes of Health (1DP2OD008735), and the United States Department of Agriculture (WIS01594).

**Figure 1. Chemical structures of the major PLs in bacteria.** For simplicity, PLs are shown with unsaturated 18-carbon tails; however, these molecules can have various acyl chains that differ in the length, number, position, and geometry of unsaturated bonds. Phospholipid head groups are bold and highlighted in red. CL contains two phosphate groups; it is reported to have a net charge of -1 at physiological pH as one phosphate is protonated and forms an intra-molecular hydrogen bond with the secondary hydroxyl group on the glycerol head group. This figure was reproduced with permission from the following reference (38). Copyright © American Society for Microbiology.

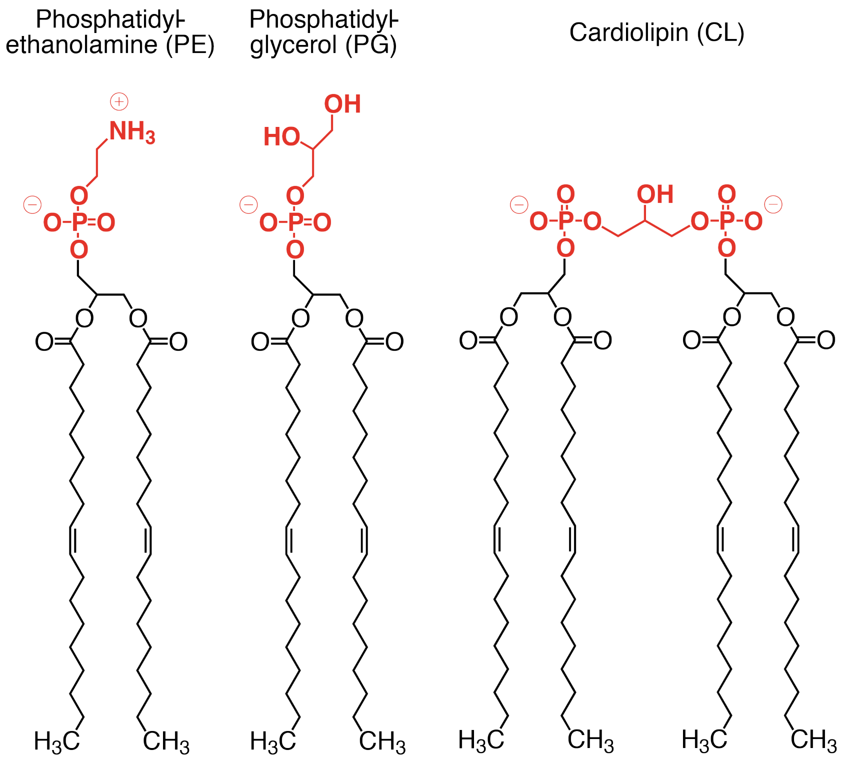
Phosphatidyl-
ethanolamine (PE)
Phosphatidyl-
glycerol (PG)
Cardiolipin (CL)
NH3
OH
HO
O-P=O
O-P-O
OH
H3C
CH3

**Figure 1**

**Figure 2. A cartoon depicting the structure of the cell envelope of gram-positive and gram-negative bacteria.** The cell envelope of gram-positive bacteria contains a cytoplasmic membrane surrounded by a thick layer of peptidoglycan. In contrast the cell envelope of gram-negative bacteria consists of a cytoplasmic membrane and outer membrane, with a thin layer of peptidoglycan positioned between the membranes. This figure was reproduced with permission from the following reference (113). Copyright © 2011 American Chemical Society.

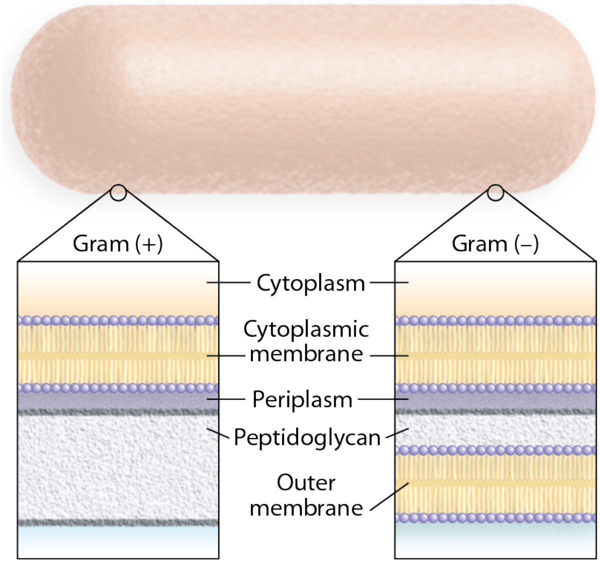
Gram (+)
Gram (–)
Cytoplasm
Cytoplasmic membrane
Periplasm
Peptidoglycan
Outer membrane

**Figure 2**

**Figure 3. Biosynthesis of bacterial PLs.** This figure depicts the most common pathways and enzymes for the biosynthesis of PLs in bacteria. See the text for an explanation of the pathways. CMP, cytidine monophosphate; CTP, cytidine triphosphate; EA, ethanolamine; euCls, eukaryotic-type Cls; G3P, glycerol-3-phosphate; Gly, glycerol; L-ser, L-serine; PPi, pyrophosphate; Pi, inorganic phosphate. For simplicity, a red P surrounded by a circle represents the glycerol phosphate head group of the PLs, black zigzag lines represent acyl portions of PLs, and the unique chemistry of each head groups is shown.

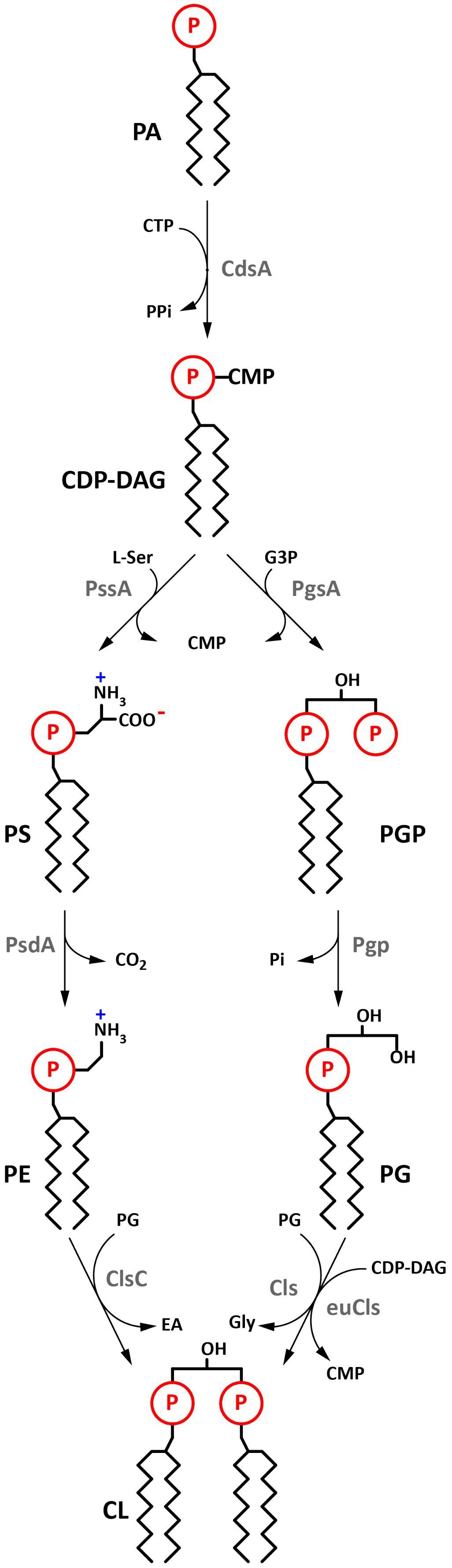
P
PA
CTP
CdsA
PPi
P
CMP
CDP-DAG
L-Ser
PssA
G3P
PgsA
CMP
NH3+
COO-
P
OH
P
P
PS
PGP
PsdA
CO2
Pi
Pgp
NH3+
P
OH
OH
P
PE
PG
PG
PG
ClsC
Cls
CDP-DAG
euCls
EA
Gly
OH
CMP
P
P
CL

Figure 3

**Figure 4.** (A) Microscopy images of *E. coli* wild-type and *ΔclsABC* (BKT12) cells labeled with NAO. NAO red fluorescence concentrates at the cell poles and septa. Scale bar, 5 µm. (B) Red fluorescence intensity profiles of cells labeled with NAO versus cell length. The shaded space surrounding the NAO red fluorescence intensity profiles indicates the standard error of the intensity at each point. Dividing cells were intentionally excluded from the analysis. (C) Percent abundances of PE, PG, CL, and PA determined by liquid chromatography-mass spectrometry (LC-MS) of minicell-producing *E. coli* wild-type and ΔclsABC strains (ns, nonsignificant; *, $P < 0.05$; **, $P < 0.01$; ***, $P < 0.001$; ****, $P < 0.0001$). PG and CL localize at the cell poles of wild-type cells. The polar membranes of *ΔclsABC* cells are enriched in PG. This figure was reproduced with permission from the following reference (38). Copyright © American Society for Microbiology.

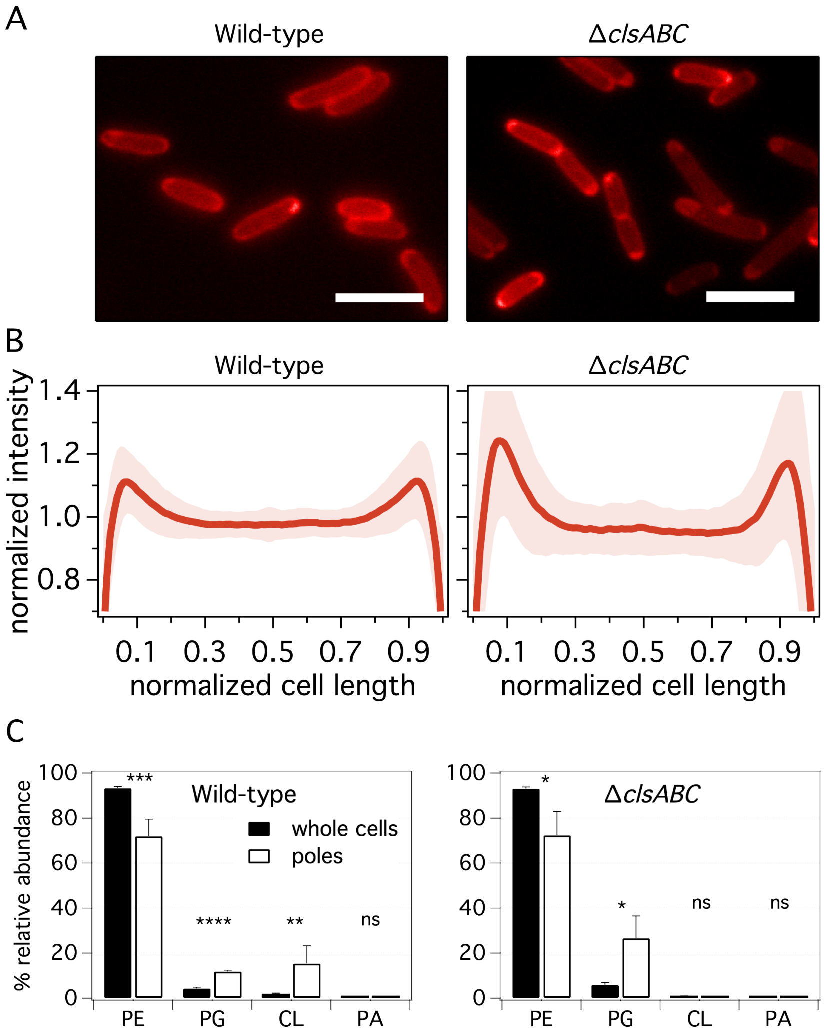
A
Wild-type
ΔclsABC
B
Wild-type
ΔclsABC
normalized intensity
1.4
1.2
1.0
0.8
0.1 0.3 0.5 0.7 0.9
normalized cell length
0.1 0.3 0.5 0.7 0.9
normalized cell length
C
% relative abundance
100
80
60
40
20
0
Wild-type
whole cells
poles
***
****
**
ns
PE
PG
CL
PA
ΔclsABC
*
*
ns
ns
PE
PG
CL
PA

**Figure 4**

**Table 1. Major PL compositions in membranes of different model bacteria.**

| | Percentage of total PLs in membranes (%)[a] | | | |
|---|---|---|---|---|
| Bacterial strain | PE | PG | CL | Reference |
| **Gram-negative bacteria** | | | | |
| *Escherichia coli* | 80 | 15 | 5 | (24) |
| *Caulobacter crescentus* | ND[b] | 78 | 9 | (114) |
| *Pseudomonas aeruginosa* | 60 | 21 | 11 | (115) |
| *Proteus mirabilis* | 76 | 13 | 6 | (116) |
| **Gram-positive bacteria** | | | | |
| *Bacillus subtilis* | 49 | 25 | 8 | (28) |
| *Staphylococcus aureus* | ND[b] | 50 | 32 | (22) |
| *Streptococcus pneumonia* | ND[b] | 60 | 40 | (117) |

[a] Percentage calculated according to the phosphate contents of PLs extracted from cells in log phase. PLs were separated and quantified on TLC plates (see references for details).

[b] Not detected.

**Table 2. Summary of bacterial processes regulated by specific anionic PLs and their interacting proteins.**

| Bacterial process | Anionic PL | Protein |
|---|---|---|
| ATP synthesis | CL | Energy-transducing proteins[a] |
| DNA replication | CL | DnaA |
| Protein translocation | PG[b] | SecA |
|  | CL[c] | EpsE/EpsL, SecYEG |
| Cell division | PG[b] | MinD, FtsA/FtsZ |
|  | CL[c] | FtsA, MinD, MinE |
| Osmo-adaptation | CL | ProP |
| DNA repair | PG, CL | RecA |

[a] CL promotes the activity of several energy-transducing proteins. See text for details.

[b] PG regulates protein translocation and cell division in gram-positive bacteria. See text for references.

[c] CL regulates protein translocation and cell division in gram-negative bacteria. See text for references.

## REFERENCES

1. **Sohlenkamp C, Geiger O.** 2016. Bacterial membrane lipids: diversity in structures and pathways. FEMS Microbiol Rev **40:**133-159.

2. **Silhavy TJ, Kahne D, Walker S.** 2010. The bacterial cell envelope. Cold Spring Harb Perspect Biol **2:**a000414.

3. **Matsumoto K, Kusaka J, Nishibori A, Hara H.** 2006. Lipid domains in bacterial membranes. Mol Microbiol **61:**1110-1117.

4. **Barak I, Muchova K.** 2013. The role of lipid domains in bacterial cell processes. Int J Mol Sci **14:**4050-4065.

5. **Arias-Cartin R, Grimaldi S, Arnoux P, Guigliarelli B, Magalon A.** 2012. Cardiolipin binding in bacterial respiratory complexes: structural and functional implications. Biochim Biophys Acta **1817:**1937-1949.

6. **Saxena R, Fingland N, Patil D, Sharma AK, Crooke E.** 2013. Crosstalk between DnaA protein, the initiator of *Escherichia coli* chromosomal replication, and acidic phospholipids present in bacterial membranes. Int J Mol Sci **14:**8517-8537.

7. **Mileykovskaya E, Dowhan W.** 2005. Role of membrane lipids in bacterial division-site selection. Curr Opin Microbiol **8:**135-142.

8. **Gold VA, Robson A, Bao H, Romantsov T, Duong F, Collinson I.** 2010. The action of cardiolipin on the bacterial translocon. Proc Natl Acad Sci U S A **107:**10044-10049.

9. **Rajendram M, Zhang L, Reynolds BJ, Auer GK, Tuson HH, Ngo KV, Cox MM, Yethiraj A, Cui Q, Weibel DB.** 2015. Anionic Phospholipids Stabilize RecA Filament Bundles in *Escherichia coli*. Mol Cell **60:**374-384.

10. **Lin TY, Santos TM, Kontur WS, Donohue TJ, Weibel DB.** 2015. A Cardiolipin-Deficient Mutant of *Rhodobacter sphaeroides* Has an Altered Cell Shape and Is Impaired in Biofilm Formation. J Bacteriol **197:**3446-3455.

11. **Jyothikumar V, Klanbut K, Tiong J, Roxburgh JS, Hunter IS, Smith TK, Herron PR.** 2012. Cardiolipin synthase is required for *Streptomyces coelicolor* morphogenesis. Mol Microbiol **84:**181-197.

12. **de Vrije T, de Swart RL, Dowhan W, Tommassen J, de Kruijff B.** 1988. Phosphatidylglycerol is involved in protein translocation across *Escherichia coli* inner membranes. Nature **334:**173-175.

13. **Lingwood D, Simons K.** 2010. Lipid rafts as a membrane-organizing principle. Science **327:**46-50.

14. **Sandoval-Calderon M, Geiger O, Guan Z, Barona-Gomez F, Sohlenkamp C.** 2009. A eukaryote-like cardiolipin synthase is present in *Streptomyces coelicolor* and in most actinobacteria. J Biol Chem **284:**17383-17390.

15. **Tan BK, Bogdanov M, Zhao J, Dowhan W, Raetz CR, Guan Z.** 2012. Discovery of a cardiolipin synthase utilizing phosphatidylethanolamine and phosphatidylglycerol as substrates. Proc Natl Acad Sci U S A **109:**16504-16509.

16. **Nishijima S, Asami Y, Uetake N, Yamagoe S, Ohta A, Shibuya I.** 1988. Disruption of the *Escherichia coli cls* gene responsible for cardiolipin synthesis. J Bacteriol **170:**775-780.

17. **Kuhn S, Slavetinsky CJ, Peschel A.** 2015. Synthesis and function of phospholipids in *Staphylococcus aureus*. Int J Med Microbiol **305:**196-202.

18. **Koprivnjak T, Zhang D, Ernst CM, Peschel A, Nauseef WM, Weiss JP.** 2011. Characterization of *Staphylococcus aureus* cardiolipin synthases 1 and 2 and their contribution to accumulation of cardiolipin in stationary phase and within phagocytes. J Bacteriol **193:**4134-4142.

19. **Zhang YM, Rock CO.** 2008. Membrane lipid homeostasis in bacteria. Nat Rev Microbiol **6:**222-233.

20. **Linde K, Grobner G, Rilfors L.** 2004. Lipid dependence and activity control of phosphatidylserine synthase from *Escherichia coli*. FEBS Lett **575:**77-80.

21. **Salamon Z, Lindblom G, Rilfors L, Linde K, Tollin G.** 2000. Interaction of phosphatidylserine synthase from *E. coli* with lipid bilayers: coupled plasmon-waveguide resonance spectroscopy studies. Biophys J **78:**1400-1412.

22. **Tsai M, Ohniwa RL, Kato Y, Takeshita SL, Ohta T, Saito S, Hayashi H, Morikawa K.** 2011. *Staphylococcus aureus* requires cardiolipin for survival under conditions of high salinity. BMC Microbiol **11:**13.

23. **Ohniwa RL, Kitabayashi K, Morikawa K.** 2013. Alternative cardiolipin synthase Cls1 compensates for stalled Cls2 function in *Staphylococcus aureus* under conditions of acute acid stress. FEMS Microbiol Lett **338:**141-146.

24. **Romantsov T, Helbig S, Culham DE, Gill C, Stalker L, Wood JM.** 2007. Cardiolipin promotes polar localization of osmosensory transporter ProP in *Escherichia coli*. Mol Microbiol **64:**1455-1465.

25. **Shibuya I, Miyazaki C, Ohta A.** 1985. Alteration of phospholipid composition by combined defects in phosphatidylserine and cardiolipin synthases and physiological consequences in *Escherichia coli*. J Bacteriol **161:**1086-1092.

26. **Dowhan W.** 1997. Molecular basis for membrane phospholipid diversity: why are there so many lipids? Annu Rev Biochem **66:**199-232.

27. **Hiraoka S, Matsuzaki H, Shibuya I.** 1993. Active increase in cardiolipin synthesis in the stationary growth phase and its physiological significance in *Escherichia coli.* FEBS Lett **336:**221-224.

28. **Lopez CS, Alice AF, Heras H, Rivas EA, Sanchez-Rivas C.** 2006. Role of anionic phospholipids in the adaptation of *Bacillus subtilis* to high salinity. Microbiology **152:**605-616.

29. **Ragolia L, Tropp BE.** 1994. The effects of phosphoglycerides on *Escherichia coli* cardiolipin synthase. Biochim Biophys Acta **1214:**323-332.

30. **Singer SJ, Nicolson GL.** 1972. The fluid mosaic model of the structure of cell membranes. Science **175:**720-731.

31. **Vanounou S, Parola AH, Fishov I.** 2003. Phosphatidylethanolamine and phosphatidylglycerol are segregated into different domains in bacterial membrane. A study with pyrene-labelled phospholipids. Mol Microbiol **49:**1067-1079.

32. **Christensen H, Garton NJ, Horobin RW, Minnikin DE, Barer MR.** 1999. Lipid domains of mycobacteria studied with fluorescent molecular probes. Mol Microbiol **31:**1561-1572.

33. **Petit JM, Maftah A, Ratinaud MH, Julien R.** 1992. 10N-nonyl acridine orange interacts with cardiolipin and allows the quantification of this phospholipid in isolated mitochondria. Eur J Biochem **209:**267-273.

34. **Petit JM, Huet O, Gallet PF, Maftah A, Ratinaud MH, Julien R.** 1994. Direct analysis and significance of cardiolipin transverse distribution in mitochondrial inner membranes. Eur J Biochem **220:**871-879.

35. **Mileykovskaya E, Dowhan W.** 2000. Visualization of phospholipid domains in *Escherichia coli* by using the cardiolipin-specific fluorescent dye 10-N-nonyl acridine orange. J Bacteriol **182:**1172-1175.

36. **Kawai F, Shoda M, Harashima R, Sadaie Y, Hara H, Matsumoto K.** 2004. Cardiolipin domains in Bacillus subtilis marburg membranes. J Bacteriol **186:**1475-1483.

37. **Koppelman CM, Den Blaauwen T, Duursma MC, Heeren RM, Nanninga N.** 2001. *Escherichia coli* minicell membranes are enriched in cardiolipin. J Bacteriol **183:**6144-6147.

38. **Oliver PM, Crooks JA, Leidl M, Yoon EJ, Saghatelian A, Weibel DB.** 2014. Localization of anionic phospholipids in *Escherichia coli* cells. J Bacteriol **196:**3386-3398.

39. **Barak I, Muchova K, Wilkinson AJ, O'Toole PJ, Pavlendova N.** 2008. Lipid spirals in *Bacillus subtilis* and their role in cell division. Mol Microbiol **68:**1315-1327.

40. **Strahl H, Burmann F, Hamoen LW.** 2014. The actin homologue MreB organizes the bacterial cell membrane. Nat Commun **5:**3442.

41. **Muchova K, Wilkinson AJ, Barak I.** 2011. Changes of lipid domains in *Bacillus subtilis* cells with disrupted cell wall peptidoglycan. FEMS Microbiol Lett **325:**92-98.

42. **Fishov I, Woldringh CL.** 1999. Visualization of membrane domains in *Escherichia coli*. Mol Microbiol **32:**1166-1172.

43. **McAuley KE, Fyfe PK, Ridge JP, Isaacs NW, Cogdell RJ, Jones MR.** 1999. Structural details of an interaction between cardiolipin and an integral membrane protein. Proc Natl Acad Sci U S A **96:**14706-14711.

44. **Unsay JD, Cosentino K, Subburaj Y, Garcia-Saez AJ.** 2013. Cardiolipin effects on membrane structure and dynamics. Langmuir **29:**15878-15887.

45. **Tomsie N, Babnik B, Lombardo D, Mavcic B, Kanduser M, Iglic A, Kralj-Iglic V.** 2005. Shape and size of giant unilamellar phospholipid vesicles containing cardiolipin. J Chem Inf Model **45:**1676-1679.

46. **Powell GL, Hui SW.** 1996. Tetraoleoylpyrophosphatidic acid: a four acyl-chain lipid which forms a hexagonal II phase with high curvature. Biophys J **70:**1402-1406.

47. **Hamai C, Yang T, Kataoka S, Cremer PS, Musser SM.** 2006. Effect of average phospholipid curvature on supported bilayer formation on glass by vesicle fusion. Biophys J **90:**1241-1248.

48. **Sennato S, Bordi F, Cametti C, Coluzza C, Desideri A, Rufini S.** 2005. Evidence of domain formation in cardiolipin-glycerophospholipid mixed monolayers. A thermodynamic and AFM study. J Phys Chem B **109:**15950-15957.

49. **Domenech O, Sanz F, Montero MT, Hernandez-Borrell J.** 2006. Thermodynamic and structural study of the main phospholipid components comprising the mitochondrial inner membrane. Biochim Biophys Acta **1758:**213-221.

50. **Domenech O, Morros A, Cabanas ME, Montero MT, Hernandez-Borrell J.** 2007. Thermal response of domains in cardiolipin content bilayers. Ultramicroscopy **107:**943-947.

51. **Koch AL, Pinette MF.** 1987. Nephelometric determination of turgor pressure in growing gram-negative bacteria. J Bacteriol **169:**3654-3663.

52. **Phillips R, Ursell T, Wiggins P, Sens P.** 2009. Emerging roles for lipids in shaping membrane-protein function. Nature **459:**379-385.

53. **Yao X, Jericho M, Pink D, Beveridge T.** 1999. Thickness and elasticity of gram-negative murein sacculi measured by atomic force microscopy. J Bacteriol **181:**6865-6875.

54. **Huang KC, Mukhopadhyay R, Wingreen NS.** 2006. A curvature-mediated mechanism for localization of lipids to bacterial poles. PLoS Comput Biol **2:**e151.

55. **Mukhopadhyay R, Huang KC, Wingreen NS.** 2008. Lipid localization in bacterial cells through curvature-mediated microphase separation. Biophys J **95:**1034-1049.

56. **Renner LD, Weibel DB.** 2011. Cardiolipin microdomains localize to negatively curved regions of *Escherichia coli* membranes. Proc Natl Acad Sci U S A **108:**6264-6269.

57. **Renner LD, Eswaramoorthy P, Ramamurthi KS, Weibel DB.** 2013. Studying biomolecule localization by engineering bacterial cell wall curvature. PLoS One **8:**e84143.

58. **Leung CW, Hong Y, Hanske J, Zhao E, Chen S, Pletneva EV, Tang BZ.** 2014. Superior fluorescent probe for detection of cardiolipin. Anal Chem **86:**1263-1268.

59. **Nishibori A, Kusaka J, Hara H, Umeda M, Matsumoto K.** 2005. Phosphatidylethanolamine domains and localization of phospholipid synthases in *Bacillus subtilis* membranes. J Bacteriol **187:**2163-2174.

60. **Alley SH, Ces O, Barahona M, Templer RH.** 2008. X-ray diffraction measurement of the monolayer spontaneous curvature of dioleoylphosphatidylglycerol. Chem Phys Lipids **154:**64-67.

61. **Cayley DS, Guttman HJ, Record MT, Jr.** 2000. Biophysical characterization of changes in amounts and activity of *Escherichia coli* cell and compartment water and turgor pressure in response to osmotic stress. Biophys J **78:**1748-1764.

62. **Rosch JW, Hsu FF, Caparon MG.** 2007. Anionic lipids enriched at the ExPortal of *Streptococcus pyogenes*. J Bacteriol **189:**801-806.

63. **Norris V.** 1995. Hypothesis: chromosome separation in *Escherichia coli* involves autocatalytic gene expression, transertion and membrane-domain formation. Mol Microbiol **16:**1051-1057.

64. **Kennell D, Riezman H.** 1977. Transcription and translation initiation frequencies of the *Escherichia coli* lac operon. J Mol Biol **114:**1-21.

65. **Dancey GF, Shapiro BM.** 1977. Specific phospholipid requirement for activity of the purified respiratory chain NADH dehydrogenase of *Escherichia coli*. Biochim Biophys Acta **487:**368-377.

66. **Laage S, Tao Y, McDermott AE.** 2015. Cardiolipin interaction with subunit c of ATP synthase: solid-state NMR characterization. Biochim Biophys Acta **1848:**260-265.

67. **Binenbaum Z, Parola AH, Zaritsky A, Fishov I.** 1999. Transcription-and translation-dependent changes in membrane dynamics in bacteria: testing the transertion model for domain formation. Mol Microbiol **32:**1173-1182.

68. **Epand RF, Tokarska-Schlattner M, Schlattner U, Wallimann T, Epand RM.** 2007. Cardiolipin clusters and membrane domain formation induced by mitochondrial proteins. J Mol Biol **365:**968-980.

69. **Polyansky AA, Volynsky RRPE, Sbalzarini IF, Marrink SJ, Efremov RG.** 2010. Antimicrobial peptides induce growth of phosphatidylglycerol domains in a model bacterial membrane. J Phys Chem Lett **1:**3108–3111.

70. **Ursell TS, Nguyen J, Monds RD, Colavin A, Billings G, Ouzounov N, Gitai Z, Shaevitz JW, Huang KC.** 2014. Rod-like bacterial shape is maintained by feedback between cell curvature and cytoskeletal localization. Proc Natl Acad Sci U S A **111:**E1025-1034.

71. **Kates M, Syz JY, Gosser D, Haines TH.** 1993. pH-dissociation characteristics of cardiolipin and its 2'-deoxy analogue. Lipids **28:**877-882.

72. **Zhang X, Tamot B, Hiser C, Reid GE, Benning C, Ferguson-Miller S.** 2011. Cardiolipin deficiency in *Rhodobacter sphaeroides* alters the lipid profile of membranes and of crystallized cytochrome oxidase, but structure and function are maintained. Biochemistry **50:**3879-3890.

73. **Jormakka M, Tornroth S, Byrne B, Iwata S.** 2002. Molecular basis of proton motive force generation: structure of formate dehydrogenase-N. Science **295:**1863-1868.

74. **Yankovskaya V, Horsefield R, Tornroth S, Luna-Chavez C, Miyoshi H, Leger C, Byrne B, Cecchini G, Iwata S.** 2003. Architecture of succinate dehydrogenase and reactive oxygen species generation. Science **299:**700-704.

75. **Tanaka Y, Anraku Y, Futai M.** 1976. *Escherichia coli* membrane D-lactate dehydrogenase. Isolation of the enzyme in aggregated from and its activation by Triton X-100 and phospholipids. J Biochem **80:**821-830.

76. **Esfahani M, Rudkin BB, Cutler CJ, Waldron PE.** 1977. Lipid-protein interactions in membranes: interaction of phospholipids with respiratory enzymes of *Escherichia coli* membrane. J Biol Chem **252:**3194-3198.

77. **Arias-Cartin R, Grimaldi S, Pommier J, Lanciano P, Schaefer C, Arnoux P, Giordano G, Guigliarelli B, Magalon A.** 2011. Cardiolipin-based respiratory complex activation in bacteria. Proc Natl Acad Sci U S A **108:**7781-7786.

78. **Fingland N, Flatten I, Downey CD, Fossum-Raunehaug S, Skarstad K, Crooke E.** 2012. Depletion of acidic phospholipids influences chromosomal replication in *Escherichia coli*. Microbiologyopen **1:**450-466.

79. **Kitchen JL, Li Z, Crooke E.** 1999. Electrostatic interactions during acidic phospholipid reactivation of DnaA protein, the *Escherichia coli* initiator of chromosomal replication. Biochemistry **38:**6213-6221.

80. **Crooke E, Castuma CE, Kornberg A.** 1992. The chromosome origin of *Escherichia coli* stabilizes DnaA protein during rejuvenation by phospholipids. J Biol Chem **267:**16779-16782.

81. **Sekimizu K, Kornberg A.** 1988. Cardiolipin activation of dnaA protein, the initiation protein of replication in *Escherichia coli*. J Biol Chem **263:**7131-7135.

82. **Yung BY, Kornberg A.** 1988. Membrane attachment activates dnaA protein, the initiation protein of chromosome replication in *Escherichia coli*. Proc Natl Acad Sci U S A **85:**7202-7205.

83. **Castuma CE, Crooke E, Kornberg A.** 1993. Fluid membranes with acidic domains activate DnaA, the initiator protein of replication in *Escherichia coli*. J Biol Chem **268:**24665-24668.

84. **Boeneman K, Fossum S, Yang Y, Fingland N, Skarstad K, Crooke E.** 2009. *Escherichia coli* DnaA forms helical structures along the longitudinal cell axis distinct from MreB filaments. Mol Microbiol **72:**645-657.

85. **Campo N, Tjalsma H, Buist G, Stepniak D, Meijer M, Veenhuis M, Westermann M, Muller JP, Bron S, Kok J, Kuipers OP, Jongbloed JD.** 2004. Subcellular sites for bacterial protein export. Mol Microbiol **53:**1583-1599.

86. **Lill R, Dowhan W, Wickner W.** 1990. The ATPase activity of SecA is regulated by acidic phospholipids, SecY, and the leader and mature domains of precursor proteins. Cell **60:**271-280.

87. **Camberg JL, Johnson TL, Patrick M, Abendroth J, Hol WG, Sandkvist M.** 2007. Synergistic stimulation of EpsE ATP hydrolysis by EpsL and acidic phospholipids. EMBO J **26:**19-27.

88. **Mileykovskaya E, Fishov I, Fu X, Corbin BD, Margolin W, Dowhan W.** 2003. Effects of phospholipid composition on MinD-membrane interactions in vitro and in vivo. J Biol Chem **278:**22193-22198.

89. **Hsieh CW, Lin TY, Lai HM, Lin CC, Hsieh TS, Shih YL.** 2010. Direct MinE-membrane interaction contributes to the proper localization of MinDE in *E. coli*. Mol Microbiol **75:**499-512.

90. **Shih YL, Huang KF, Lai HM, Liao JH, Lee CS, Chang CM, Mak HM, Hsieh CW, Lin CC.** 2011. The N-terminal amphipathic helix of the topological specificity factor MinE is associated with shaping membrane curvature. PLoS One **6:**e21425.

91. **Vecchiarelli AG, Li M, Mizuuchi M, Mizuuchi K.** 2014. Differential affinities of MinD and MinE to anionic phospholipid influence Min patterning dynamics in vitro. Mol Microbiol **93:**453-463.

92. **Renner LD, Weibel DB.** 2012. MinD and MinE interact with anionic phospholipids and regulate division plane formation in *Escherichia coli*. J Biol Chem **287:**38835-38844.

93. **Drew DA, Osborn MJ, Rothfield LI.** 2005. A polymerization-depolymerization model that accurately generates the self-sustained oscillatory system involved in bacterial division site placement. Proc Natl Acad Sci U S A **102:**6114-6118.

94. **Shih YL, Le T, Rothfield L.** 2003. Division site selection in *Escherichia coli* involves dynamic redistribution of Min proteins within coiled structures that extend between the two cell poles. Proc Natl Acad Sci U S A **100:**7865-7870.

95. **Zieske K, Schwille P.** 2014. Reconstitution of self-organizing protein gradients as spatial cues in cell-free systems. Elife **3**.

96. **Ben-Yehuda S, Losick R.** 2002. Asymmetric cell division in *B. subtilis* involves a spiral-like intermediate of the cytokinetic protein FtsZ. Cell **109:**257-266.

97. **Bramkamp M, Emmins R, Weston L, Donovan C, Daniel RA, Errington J.** 2008. A novel component of the division-site selection system of *Bacillus subtilis* and a new mode of action for the division inhibitor MinCD. Mol Microbiol **70:**1556-1569.

98. **Edwards DH, Errington J.** 1997. The *Bacillus subtilis* DivIVA protein targets to the division septum and controls the site specificity of cell division. Mol Microbiol **24:**905-915.

99. **Lenarcic R, Halbedel S, Visser L, Shaw M, Wu LJ, Errington J, Marenduzzo D, Hamoen LW.** 2009. Localisation of DivIVA by targeting to negatively curved membranes. EMBO J **28:**2272-2282.

100. **Ramamurthi KS, Losick R.** 2009. Negative membrane curvature as a cue for subcellular localization of a bacterial protein. Proc Natl Acad Sci U S A **106:**13541-13545.

101. **Romantsov T, Stalker L, Culham DE, Wood JM.** 2008. Cardiolipin controls the osmotic stress response and the subcellular location of transporter ProP in *Escherichia coli*. J Biol Chem **283:**12314-12323.

102. **Catucci L, Depalo N, Lattanzio VM, Agostiano A, Corcelli A.** 2004. Neosynthesis of cardiolipin in *Rhodobacter sphaeroides* under osmotic stress. Biochemistry **43:**15066-15072.

103. **Dalebroux ZD, Matamouros S, Whittington D, Bishop RE, Miller SI.** 2014. PhoPQ regulates acidic glycerophospholipid content of the *Salmonella Typhimurium* outer membrane. Proc Natl Acad Sci U S A **111:**1963-1968.

104. **Dalebroux ZD, Edrozo MB, Pfuetzner RA, Ressl S, Kulasekara BR, Blanc MP, Miller SI.** 2015. Delivery of cardiolipins to the *Salmonella* outer membrane is necessary for survival within host tissues and virulence. Cell Host Microbe **17:**441-451.

105. **Bernal P, Munoz-Rojas J, Hurtado A, Ramos JL, Segura A.** 2007. A *Pseudomonas putida* cardiolipin synthesis mutant exhibits increased sensitivity to drugs related to transport functionality. Environ Microbiol **9:**1135-1145.

106. **Matsumoto K.** 2001. Dispensable nature of phosphatidylglycerol in *Escherichia coli*: dual roles of anionic phospholipids. Mol Microbiol **39:**1427-1433.

107. **Romantsov T, Guan Z, Wood JM.** 2009. Cardiolipin and the osmotic stress responses of bacteria. Biochim Biophys Acta **1788:**2092-2100.

108. **Mileykovskaya E, Ryan AC, Mo X, Lin CC, Khalaf KI, Dowhan W, Garrett TA.** 2009. Phosphatidic acid and N-acylphosphatidylethanolamine form

membrane domains in *Escherichia coli* mutant lacking cardiolipin and phosphatidylglycerol. J Biol Chem **284:**2990-3000.

109. **Mileykovskaya E, Dowhan W.** 2009. Cardiolipin membrane domains in prokaryotes and eukaryotes. Biochim Biophys Acta **1788:**2084-2091.

110. **Weber TA, Koob S, Heide H, Wittig I, Head B, van der Bliek A, Brandt U, Mittelbronn M, Reichert AS.** 2013. APOOL is a cardiolipin-binding constituent of the Mitofilin/MINOS protein complex determining cristae morphology in mammalian mitochondria. PLoS One **8:**e63683.

111. **Chory J, Donohue TJ, Varga AR, Staehelin LA, Kaplan S.** 1984. Induction of the photosynthetic membranes of *Rhodopseudomonas sphaeroides*: biochemical and morphological studies. J Bacteriol **159:**540-554.

112. **Arechaga I.** 2013. Membrane invaginations in bacteria and mitochondria: common features and evolutionary scenarios. J Mol Microbiol Biotechnol **23:**13-23.

113. **Foss MH, Eun YJ, Weibel DB.** 2011. Chemical-biological studies of subcellular organization in bacteria. Biochemistry **50:**7719-7734.

114. **Contreras I, Shapiro L, Henry S.** 1978. Membrane phospholipid composition of *Caulobacter crescentus*. J Bacteriol **135:**1130-1136.

115. **Conrad RS, Gilleland HE, Jr.** 1981. Lipid alterations in cell envelopes of polymyxin-resistant *Pseudomonas aeruginosa* isolates. J Bacteriol **148:**487-497.

116. **Gmeiner J, Martin HH.** 1976. Phospholipid and lipopolysaccharide in *Proteus mirabilis* and its stable protoplast L-form. Difference in content and fatty acid composition. Eur J Biochem **67:**487-494.

117. **Trombe MC, Laneelle MA, Laneelle G.** 1979. Lipid composition of aminopterin-resistant and sensitive strains of *Streptococcus pneumoniae*. Effect of aminopterin inhibition. Biochim Biophys Acta **574:**290-300.

# CHAPTER 2

# A cardiolipin-deficient mutant of *Rhodobacter sphaeroides* has an altered cell shape and is impaired in biofilm formation

This chapter was adapted from:

Ti-Yu Lin, Thiago M. A. Santos, Wayne S. Kontur, Timothy J. Donohue, Douglas B. Weibel. A cardiolipin-deficient mutant of *Rhodobacter sphaeroides* has an altered cell shape and is impaired in biofilm formation. Journal of Bacteriology, 197 (21), 3446-3455, 2015

# ABSTRACT

Cell shape has been suggested to play an important role in regulating bacterial attachment to surfaces and the formation of communities associated with surfaces. We found that a cardiolipin synthase mutant (Δ*cls*) of the rod-shaped bacterium *Rhodobacter sphaeroides*—in which synthesis of the anionic, highly curved phospholipid cardiolipin (CL) is reduced by 90%—produces ellipsoidal-shaped cells that are impaired in forming biofilms. Reducing the concentration of CL did not cause significant defects in *R. sphaeroides* cell growth, swimming motility, lipopolysaccharide and exopolysaccharide production, surface adhesion protein expression, and membrane permeability. Complementation of the CL-deficient mutant by ectopically expressing CL synthase restored cells to their rod shape and increased biofilm formation. Treating *R. sphaeroides* cells with a low concentration (10 μg/mL) of the small molecule MreB inhibitor, S-(3,4-dichlorobenzyl)isothiourea (A22), produced ellipsoidal-shaped cells that had no obvious growth defect, yet reduced *R. sphaeroides* biofilm formation. This study demonstrates that CL plays a role in *R. sphaeroides* cell shape determination, biofilm formation, and the ability of this bacterium to adapt to its environment.

# INTRODUCTION

Many bacteria have evolved mechanisms of community-based living based on attachment to surfaces and growth into biofilms. Biofilm formation occurs through several stages. In the first stage, bacterial cells attach to surfaces, replicate, and accumulate to form multilayered cell communities. During biofilm maturation, bacteria secrete a layer of extracellular polymeric substances that encapsulates cells and protects them from environmental stress. At a later stage, planktonic bacterial cells are released into the bulk fluid, attach to new surfaces, replicate, and seed the formation of new biofilms. Biofilms are a central mechanism that bacteria use to adapt to changes in their environment, are prevalent in ecology, and present challenges in industrial applications and medicine due to biofouling and antibiotic resistance (1-3). For example, the North-American Centers for Disease Control and Prevention (CDC) estimates that 65% of all human infections by bacteria involve biofilms (4).

The shape of bacterial cells has been hypothesized to affect their attachment to surfaces and biofilm development (5). During the initial step for biofilm formation, cell attachment requires that the adhesive force between cells and surfaces (measured to be 0.31-19.6 pN) overcomes the shear force of flowing fluids that are present in many environments (6). Based on the mechanisms that cells typically use to attach to surfaces (e.g., fimbriae, flagella, surface adhesion proteins, exopolysaccharides (EPS), and non-specific, non-covalent forces between the outer membrane lipopolysaccharides (LPS) and surfaces), cell adhesion has been hypothesized to scale with the surface area for contact between a cell and surface (5, 7). For bacteria with an identical diameter, rod-shaped cells (surface area, 6.28 $\mu m^2$) have a higher contact area than spherical cells (surface area, 3.14 $\mu m^2$). We hypothesize that rod-shaped bacterial cells attach to surfaces more tightly than spherical-shaped cells by maximizing contact area and lead to an increase in biofilm formation due to a higher initial biomass. This hypothesis is challenging to study because it requires using different strains of rod- and spherical-shaped bacteria, which typically have differences in growth rates, cell physiology, and the production of extracellular polymeric substances. In principle this hypothesis can be studied using an organism in which shape can be altered without changing key phenotypes that play a central role in biofilm formation.

To test this hypothesis, we turned our attention to *Rhodobacter sphaeroides*. *R. sphaeroides* is a rod-shaped, Gram-negative, member of the alpha-proteobacteria that is metabolically diverse and capable of growing in environments in which the concentration of salts and nutrients is high, such as soil, mud, sludge, and anoxic zones of waters. *R. sphaeroides* and other *Rhodobacter* species are the primary surface colonists in coastal waters and are known to form biofilms (8, 9). A fascinating characteristic of *R. sphaeroides*, is that its cytoplasmic membrane undergoes unusual gymnastics during photosynthetic growth that facilitates the formation of chromatophores, which are the light harvesting organelles in cells (10). *R. sphaeroides* membranes contain the same three primary classes of phospholipids found in the majority of Gram-negative bacteria: phosphatidylethanolamine, phosphatidylglycerol, and cardiolipin (CL) (11). Bacterial membranes have been historically considered to play a passive role in cell shape determination. For example, CL has been hypothesized to concentrate at regions of large membrane curvature—that is shaped by the peptidoglycan sacculus—to dissipate elastic strain and reduce the membrane free energy (12). The physiological role of CL in *R. sphaeroides* remains largely unexplored, and yet *R. sphaeroides* has been considered a candidate for the origin of mitochondria in which the shape of the inner membrane changes dramatically—as it does in *R. sphaeroides*—and CL is essential (13-15).

In this study, we tested for a previously unrealized connection between CL and cellular adaptation using *R. sphaeroides*. We demonstrate that a CL-deficient mutant of *R. sphaeroides* results in cells with an ellipsoidal shape that are impaired in biofilm formation, particularly in early stages in which cell/surface attachment is key. We also show that chemical tools that induce the formation of ellipsoidal cells also produce a defect in biofilm formation. These studies support the hypothesis that rod-shaped bacterial cells have enhanced attachment to surfaces compared to spherical-shaped cells and produce biofilms with higher cell volumes.

# RESULTS

## CL deficiency in *R. sphaeroides* changes the shape of cells.

A CL-deficient mutant of *R. sphaeroides* (herein referred to as *R. sphaeroides* CL3) was created previously by deletion of the *CL synthase* (*cls*) gene and produces 90% less CL than wild-type cells (16). We were unable to remove CL from *R. sphaeroides* completely using genomic tools to identify and knockout potential homologs of CL synthase (see Supporting Information), and instead relied on *R. sphaeroides* strain CL3 for our studies. In contrast to rod-shaped wild-type *R. sphaeroides* cells, CL3 cells were ellipsoidal, had a characteristic decrease (35%) in their aspect ratio (Figure 1), and yet displayed no significant differences in growth compared to the wild-type strain (16). We observed the change in *R. sphaeroides* cell shape in both the log phase and stationary phase, thereby suggesting that this phenotype is growth phase-independent.

## Complementation of CL synthase in *R. sphaeroides* strain CL3 restores the rod shape of cells.

To confirm the role of CL in the change in cell shape that we observed for the CL synthase deletion mutant, we performed a plasmid-based complementation of CL synthase in the CL3 strain. Using thin-layer chromatogram (TLC) analyses, we found that phospholipids extracted from CL3 cells expressing the *R. sphaeroides* CL synthase from plasmid *cls*-pIND5sp displayed a 7-fold increase in the amount of CL compared to phospholipids extracted from cells of *R. sphaeroides* CL3 harboring the empty vector pIND5sp (Figures 2B&C). Complementing CL biosynthesis in CL3 cells increased the cell aspect ratio by 31% and restored cells to their rod-shaped phenotype (Figure 2A). These results demonstrate that CL plays a role in the establishment and maintenance of the rod shape of cells of *R. sphaeroides*.

### Reducing the concentration of CL alters *R. sphaeroides* biofilm formation.

Cell shape has been suggested to play an important role in the attachment of cells to surfaces, in part because the dominant forces of adhesion between cells and surfaces are sensitive to the amount of surface area in contact (5). To investigate the effect of cell shape on surface attachment and subsequent biofilm development of *R. sphaeroides*, we cultivated biofilms of wild-type and CL3 cells in growth medium containing the cell-permeable, lipophilic fluorescent dye, Nile Red. We used Nile Red in these experiments as it labels the cell membrane and makes it possible to visualize cells using epifluorescence/confocal microscopy, is biocompatible, and does not change cell shape and impede cell growth (17) (Figure S1). We performed these experiments in static growth conditions (i.e., no flow), which is an ideal system for the study of biofilm formation in early stages in which cell/surface attachment is key (18). In addition, static conditions enable us to reproduce and quantify experiments with different *R. sphaeroides* strains. In static cultures, wild-type *R. sphaeroides* cells formed biofilms after 72 h with a mean thickness of 20 μm; however, CL3 cells incubated for 72 h produced only small microcolonies on surfaces, were 9-μm thick, and did not form biofilms that extended over larger surface areas (Figure 3A&S2). To measure cell attachment to surface directly, we imaged surface-attached cells at 1, 24, 48 and 72 h after incubation and counted the number of cells attached to surfaces at the time point of 1 h (Figure 3B&S3). Cell adherence was significantly reduced, from $3.6 \pm 0.3 \times 10^4$ cells/mm$^2$ in the wild-type strain, to $1.7 \pm 0.2 \times 10^4$ cells/mm$^2$ in the CL3 mutant (Figure 3B), suggesting that cells of the *R. sphaeroides* CL3 mutant displayed reduced attachment to surfaces than did wild-type cells. We observed that wild-type cells attached to surfaces increased in cell length over time when attached to surfaces. CL3 cells that attached to surfaces changed in shape and length from ellipsoids to a rod shape (Figure 3C). To quantify early stages of biofilm formation in which biofilm differences may be most pronounced because of the potential impact of cell shape on surface attachment, we cultivated biofilms for 72 h in microtiter dishes with polystyrene surfaces and labeled cells with crystal violet (CV). *R. sphaeroides* strain CL3 displayed a 54% reduction in biofilm formation compared with the wild-type strain after 72 h of incubation (Figure 3D), which was materials-independent and occurred on both polystyrene and glass surfaces (Figure S4). Figure 3E demonstrates that there is no significant difference in planktonic growth between wild-type and CL3 cells. Although a ~0.1 difference in absorbance ($\lambda$, 600 nm) was observed at stationary phase, the colony-forming units (CFUs) of the wild-type and CL3 strains were not significantly different (wild-type: $1.6 \times 10^9$ CFU/mL, CL3: $1.5 \times 10^9$ CFU/mL), suggesting that impaired biofilm formation was not a result of a growth defect.

### CL deficiency in *R. sphaeroides* does not cause defects in swimming motility, LPS production, *fasciclin I domain protein (fdp)* gene expression, EPS production, and membrane permeability.

Swimming motility plays an important role in biofilm formation in *R. sphaeroides* and other bacterial species (9, 19-22). It has been hypothesized that motility enables cells to overcome surface repulsion forces, contact surfaces, and adsorb. In close physical proximity to surfaces, flagella make it possible for bacterial cells to adsorb and attach to surfaces (7, 21). To examine whether the CL3 strain has motility defects, we assessed the motility of wild-type and CL3 cells in motility agar. After 72 h of incubation at 30°C, CL3 cells displayed comparable swimming diameters with wild-type cells (Figure 4A&B). In addition, we measured the proportion of motile cells in wild-type and CL3 cell cultures in phase-contrast microscopy videos and found no significant difference (wild-type: 4.3 ± 2%, CL3: 4.2 ± 1%). We also measured single cell velocities of wild-type and CL3 cells using a particle-tracking algorithm and found no significant difference in the swimming velocity of cells between the two strains (wild-type: 30 ± 4 μm/s, CL3: 29 ± 5 μm/s) (Figure 4C). To confirm these results, we compared the expression of the primary flagellar protein, FliC in CL3 and wild-type *R. sphaeroides* cells. Using a real-time quantitative polymerase chain reaction (qPCR) assay, we found no significant difference between the expression levels of *fliC* gene in wild-type and CL3 cells (Figure 4D). These results suggest that the reduction in CL3 biofilms was unlikely to be due to defects in motility or flagella assembly.

LPS has been implicated in the attachment of bacterial cells to surfaces (23-25). The O-antigen of LPS controls cell surface hydrophobicity and surface charge and influences the interaction of cells with substrates (26). It is unknown whether alterations in membrane composition—specifically the reduction in the concentration of CL—have an impact on LPS production. To determine whether the CL3 strain has a defect in LPS production, we extracted and compared LPS from wild-type and CL3 cells. LPS from both *R. sphaeroides* strains displayed similar banding patterns of O-antigen repeats and was present in similar amounts as evidenced by quantification of the bands on the gel (Figure 4E&F). These results suggest that the impaired biofilm formation we observed in the CL3 strain was unlikely to be due to defects in LPS production.

*R. sphaeroides* Fdp has been suggested to function as a surface adhesion protein. Fdp knockout mutants of *R. sphaeroides* lose the ability to adhere to surfaces and form defective biofilms (27). We compared the transcription of the *fdp* gene in *R.*

*sphaeroides* wild-type and CL3 strains and found no significant difference between *fdp* transcription in wild-type and CL3 cells (Figure 4G). These results indicate that impaired CL3 biofilm formation is not attributed to changes in Fdp production.

EPS is a key component of the extracellular polymeric substances produced by many biofilm-forming bacteria and required for cellular attachment to surfaces and subsequent biofilm formation (28). To investigate whether the CL3 mutant has defects in producing EPS, we extracted EPS from planktonic cultures of wild-type and CL3 cells and analyzed them on an SDS-polyacrylamide gel (Figure S5). EPS produced from the both *R. sphaeroides* strains was present in similar amounts as evidenced by quantification of the EPS on the gel (Figure 4H). These results suggest that the reduction in CL3 biofilms is unlikely to be due to defects in EPS production.

Membrane permeability is connected to a variety of different processes in the cell, including the transport of nutrients, ions and charged molecules, and quorum sensing compounds. Transport properties have been shown to alter biofilm formation in many bacterial species (29, 30). For example, bacterial quorum sensing is important for the construction of biofilms and the membrane permeability of biofilm cells may play a role in the release of quorum-sensing signals required for biofilm development (29-31). To investigate whether a CL deficiency alters membrane permeability, we used propidium iodide (PI), which labels the DNA of cells with disrupted membranes. We found that *R. sphaeroides* wild-type and CL3 cells displayed comparable PI fluorescence intensities (Figure 4I), suggesting that a CL deficiency does not alter membrane integrity, and that altered biofilm formation in CL3 was unlikely due to defects in membrane permeability.

### ***R. sphaeroides*** **cell shape impacts biofilm formation**

To further evaluate whether cell shape regulates biofilm formation, we quantified the effect of CL complementation on the ability of CL3 cells to form biofilms. We expressed *R. sphaeroides* CL synthase from plasmid *cls*-pIND5sp in CL3 cells and the empty vector pIND5sp in wild-type cells. Complementing CL biosynthesis in CL3 cells increased the cell aspect ratio by 20% compared to wild-type cells harboring the empty vector (Figure 5A). TLC analyses of lipids showed that the complementation increased the amount of CL by 60% in CL3 cells compared to wild-type cells harboring the empty vector (Figure 5B). Both strains (CL3 containing *cls*-pIND5sp or wild-type containing pIND5sp) showed no difference in planktonic growth (Figure 5D). *R. sphaeroides* strain CL3 containing *cls*-pIND5sp restored biofilm formation by 26% (measured by CV labeling) compared to wild-type cells (compare Figure 5C and Figure 3D).

We used a chemical biological approach to independently test if a change in cell shape could cause altered formation of *R. sphaeroides* biofilms. S-(3,4-dichlorobenzyl)isothiourea (referred to as A22) is a small molecule that disrupts the MreB cytoskeleton, causes MreB filaments to depolymerize, and creates rounded cells in many species of bacteria (32, 33). *R. sphaeroides* cells treated with A22 at a concentration of 10 μg/mL [we found that the minimum inhibitory concentration (MIC) for *R. sphaeroides* is 60 μg/mL] became round (Figure 6A), however no significant changes in planktonic growth were observed over 72 h of growth (Figure 6C). Although the A22 treatment caused a ~0.1 decrease in absorbance ($\lambda$, 600 nm) at stationary phase, it did not significantly reduce the number of viable cells present (DMSO control: $1.7 \times 10^9$ CFU/mL, A22: $1.6 \times 10^9$ CFU/mL). The alteration in *R. sphaeroides* cell shape from A22 treatment caused a 70% reduction in biofilm formation (measured by CV labeling) compared to wild-type cells (Figure 6B). These results confirm our observation that CL influences *R. sphaeroides* cell shape and affects biofilm formation.

# DISCUSSION

CL plays an essential role in the adaptation of many bacterial species to environmental stresses, including high salinity and low pH (34-37). CL has also been implicated in playing an important role in regulating essential processes in bacteria, including: cell division, ATP synthesis, and protein translocation across membranes (38-41). Remarkably little is known about CL function in *R. sphaeroides*. The interaction of *R. sphaeroides* cytochrome *c* oxidase (C*c*O) and CL is essential for full activity of the enzyme (42-45). However, a previous study demonstrated that a CL deficiency in *R. sphaeroides* does not impair the structure and function of C*c*O, or cause any significant growth defects (16). Several groups have demonstrated that phosphatidylglycerol (PG) can override the absence of CL in *Escherichia coli* and restore the interaction of proteins with the membrane, which may explain the results of these previous studies with *R. sphaeroides* C*c*O (46-48).

In *E. coli*, three *cls* genes have been identified: *clsA*, *clsB*, and *clsC* share DNA sequence homology and belong to the phospholipase D superfamily. Individual knockout strains of each protein still produce some CL, however the triple *cls* knockout *E. coli* strain BKT12 does not produce any detectable CL (49). To completely remove CL from *R. sphaeroides* cells, we used computational tools to identify homologous genes coding for other CL synthases. Our analysis identified the phospholipase D family protein RSP_0113, which may be responsible for the residual CL in the CL3 strain (see Supporting Information). However, we found that RSP_0113 does not catalyze the synthesis of CL in *R. sphaeroides* as ectopically expressing it in the CL3 strain did not change the relative concentration of CL present. We are unsure of the origins of the residual CL in *R. sphaeroides* strain CL3, which may come from promiscuity of another phospholipid synthase, such as phosphatidylserine synthase, as has been reported in other cells (16).

Although the CL3 strain shows no significant defects in growth, it exhibits a characteristic ellipsoidal cell shape phenotype in both log phase and stationary phase. Rod-shaped bacteria can undergo a similar morphological change when the rate of cell division is faster than the rate of cell mass production. The CL3 strain has a similar division rate (Figure 3E) (16) and cell volume (~1.3 $\mu m^3$) as the wild-type strain (~1.2 $\mu m^3$), which suggests that the alteration in its shape is not due to a change in cell volume or decoupling growth rate and division. As cells of *E. coli* and many other rod-shaped bacterial species enter stationary phase, they often adopt a spherical-like morphology (50, 51). We did not observe a similar growth phase-dependent change in wild-type *R. sphaeroides* cell shape (i.e., cells remain rod-shaped). Our results are consistent with a change in the shape of cells of the CL3 strain that is not related to growth conditions.

Bacterial cell shape has been hypothesized to play an important role in regulating the attachment of cells to surfaces, which occurs at early stages of biofilm formation. Cell shape determines the amount of cell body in contact with surfaces and has been suggested to regulate subsequent biofilm development (5). We hypothesized that a CL deficiency in *R. sphaeroides* can cause a reduction in biofilm formation (compared to wild-type cells), as the ellipsoidal cells have a reduced surface area that limits surface attachment. Bacterial cell length and curvature are primary determinants for maximizing the amount of contact between bacterial cells and surfaces. Due to our inability to measure mean cell curvature accurately, we do not include a formal analysis of curvature on cell attachment, however papers in other areas of biology have described the connection between cell curvature and maximizing surface contact (52). To test the hypothesis regarding *R. sphaeroides* cell geometry and surface attachment, we compared biofilms of wild-type and CL3 *R. sphaeroides* strains grown in static cultures. Static growth conditions do not promote biofilm maturation typically associated with flow cell systems and are effective at identifying factors required for cell/surface attachment (18). *R. sphaeroides* CL3 strain displayed reduced attachment to surfaces compared to the wild-type strain and formed defective biofilms, which is consistent with the observation that a *rodA* mutant of *Burkholderia cepacia* forms spherical cells and shows impaired biofilm formation (53). The hypothesis that bacteria can increase the strength of their attachment to surfaces by altering cell shape has been proposed previously (e.g., a rod-shaped cell elongating into a filament, and a spherical cell increasing its length and becoming rod-shaped), yet has been untested (5). We found that cells of both *R. sphaeroides* wild-type and CL3 strains increase in length when attached to surfaces, suggesting that they may be maximizing surface contact.

Cell shape also plays a role in regulating bacterial motility, which is important for the initial attachment of cells to surfaces and subsequent biofilm development (20, 54). We found that a CL deficiency in *R. sphaeroides* alters cell shape but not swimming motility, which is interesting. However, *R. sphaeroides* cells are unlike most rod-shaped bacteria in terms of the location of its individual flagellum (not polar like most bacteria) and its biophysics and motility mechanism. Consequently, much of what we know about the influence of the shape of bacterial cells on their motility may not be applicable to *R. sphaeroides*.

LPS is the major component of the outer membrane of Gram-negative bacteria and has been shown to regulate cell attachment to surfaces (23-26). Fdp is a surface adhesion protein that is localized at the inner membranes of *R. sphaeroides,* facilitates the attachment of cells to surfaces and thus development of biofilms (27). EPS is important for cell/surface attachment and is often referred to as a primary glue or cement for biofilms (28). Our data indicate that the CL3 strain is not defective in any of these primary factors for initiation of biofilm formation. A CL deficiency may cause a change in the anionic composition of membranes that affects surface charge of cells and their attachment to surfaces. However, the level of PG is increased in the CL3 mutant and thereby retains the negatively charged character of membranes (16).

Quorum sensing occurs between cells in biofilms and signals biofilm development in several species of bacteria (29). Changes in bacterial membrane permeability could alter quorum sensing—and a variety of other cellular processes that are influenced by changes in molecular transport into the cell—and affect biofilm formation. We found that membrane permeability is unchanged in CL3 cells (compared to wild-type). *R. sphaeroides* produces acylhomoserine lactone, a quorum-sensing signal that regulates EPS production (55). Since CL3 cells produce a similar amount of EPS as wild-type cells, it is unlikely that quorum-sensing system is impaired in CL3 biofilms. These data suggest that a change in cell shape caused by CL deficiency is the primary factor that impairs biofilms formation for the *R. sphaeroides* CL3 strain, and not other physiological consequences that accompany a change in cell shape.

To further evaluate whether cell shape regulates biofilm formation, we quantified the effect of CL complementation on the ability of the CL3 strain to form biofilms, and found it restored a rod shape morphology and recovered its ability to form biofilms. Complementation was unable to completely recover biofilm formation of the CL3 strain, which we attribute is due to our inability to restore native levels of CL and completely recover the rod-shape of CL3 cells. These results correlate CL concentration to cell shape and biofilm formation.

MreB is a bacterial cytoskeletal protein that is homologous to eukaryotic actin (56). In rod-shaped bacteria, MreB polymerizes into dynamic filaments that move circumferentially around the cytoplasmic membrane of cells, interacts with cell wall synthesis machinery, and plays a role in maintaining cell shape (57-59). A22 is a small molecule inhibitor that binds MreB, disassembles filaments, causes the protein to mislocalize in cells, and produces cells with a spherical shape (32, 33). Treating *R. sphaeroides* cells with A22 produced round cells and suggests that the MreB-mediated rod shape formation model in many Gram-negative bacteria is conserved in *R. sphaeroides*. We quantified the effect of low concentrations of A22 on *R. sphaeroides* cells, found that it produced spherical cells, did not alter cell growth, and reduced biofilm formation similar to our experiments reducing CL.

In conclusion, we demonstrated that conditions that alter *R. sphaeroides* cell shape (a CL deficiency or a compound that blocks MreB activity) impede its ability to form biofilms. We suggest that cell shape affects biofilm formation by reducing the surface area for cell attachment to surfaces. The *R. sphaeroides* CL3 mutant is the first example that we are aware of in which cell membrane composition alters cell morphology and influences its adaptation by reducing its ability to form multicellular structures. Future studies will extend these results to other bacteria explore the molecular mechanisms that connect CL to bacterial cell shape.

## EXPERIMENTAL PROCEDURES

### Bacterial strains and growth conditions

*R. sphaeroides* strains were grown aerobically in Sistrom's succinate medium (60) at 30°C with shaking at 200 rpm. When required, ampicillin (50 μg/mL), kanamycin (25 μg/mL), or spectinomycin (5 μg/mL) was added to the medium. *E. coli* strains were grown in LB broth at 37°C with shaking at 200 rpm. When required, ampicillin (50 μg/mL), kanamycin (25 μg/mL), or spectinomycin (50 μg/mL) was added to the medium. The bacterial strains and plasmids used in this study are outlined in Table 1.

For growth curves, cell cultures in stationary phase were standardized to an absorbance of 1.0 (λ, 600 nm). The standardized cultures were inoculated 1/100 in 1 mL of Sistrom's succinate medium in glass test tubes and grown with shaking for 72 h at 30°C. The absorbance (λ, 600 nm) of cell cultures was measured at the indicated time points.

### CL synthase expression plasmid (*cls*-pIND5sp) construction

*cls* was amplified by PCR from *R. sphaeroides* 2.4.1 genomic DNA and cloned into pIND5sp at the NdeI and BglII sites using In-Fusion Cloning (Clontech), following the user manual. Primers used were: NdeI-*cls* (5'-GGA GAA ATT AAC ATA TGA TCG ACG ACT GGC TGG GC-3'), *cls*-BglII (5'-GAT GGT GAT GAG ATC TGA GGT AGC TCT GGA TCG G-3'). pIND5sp is a derivative of pIND4sp (a variant of pIND4 (61) with a spectinomycin resistance cassette) in which the NcoI site is replaced with an NdeI site using the Stratagene QuikChange XL Site-Directed Mutagenesis Kit, following the manufacturer's protocol. Primers used were: pIND5sp (5'-GTG ATG GTG ATG AGA TCT GGA TCC TCC ATA TGT TAA TTT

CTC CTC TTT AAT TCT AGA TG-3'), pIND5sp-anti (5'-CAT CTA GAA TTA AAG AGG AGA AAT TAA CAT ATG GAG GAT CCA GAT CTC ATC ACC ATC AC-3').

**Complementation of the CL3 strain**

The pIND5sp and *cls*-pIND5sp plasmids were transformed into *E. coli* S17-1 (62) and subsequently mobilized via conjugation into the recipient *R. sphaeroides* wild-type or CL3 strain, as described previously (63). The strains harboring these plasmids were incubated for 72 h at 30°C with 1 mM isopropyl β-D-1 thiogalactopyranoside (IPTG) to induce expression.

**Analysis of cell morphology**

An aliquot (4 μL) of cell cultures was dropped on a 2% (w/v) agarose pad prepared in phosphate-buffered saline (PBS) buffer [137 mM NaCl, 2.7 mM KCl, 10 mM $Na_2HPO_4$, 1.76 mM $KH_2PO_4$, pH 7.4], covered with a glass coverslip and imaged using an inverted Nikon Eclipse TE2000 microscope equipped with a shuttered black and white Andor iXonEM+ DU-897 electron-multiplying charge-coupled-device (EMCCD) camera (Andor Technology, South Windsor, CT). Images were acquired using a ×100 objective (Nikon Plan Apo 100×/1.40 oil DM) and the Metamorph software program (Version 7.5.6.0) (MDS Analytical Technologies, Downington, PA). Cell width and length were determined using ImageJ.

**Lipid extraction**

Polar lipids were extracted from cells using a procedure modified from the original Bligh-Dyer method (64). Briefly, 50 mL of cell cultures was grown for 72 h at 30°C. Cells were then collected by centrifugation and resuspended in 5 mL PBS. 7.5 mL of methanol-chloroform (2:1, v/v) was added to the cell suspension and the mixture was shaken for 1 h at 25°C. Two phases were created by adding 2.5 mL of chloroform and 2.5 mL of 0.1 N HCl, followed by centrifugation at 1,000 g, 4°C for 10 min. The bottom chloroform phase was collected by means of a glass Pasteur pipette and dried under nitrogen in a small glass vial. The extracted lipids were weighed, redissolved in chloroform, and stored at -20°C.

### TLC

Total lipid extracts were analyzed by TLC on silica gel (TLC silica gel 60, catalog number HX259108; EMD Millipore). The plate was developed with the solvent chloroform-methanol-acetic acid-water (85:15:10:3.5, v/v) (65), and developed in a vapor of iodine until the bands became visible. The content of CL was quantified by densitometry using ImageJ. The densitometry was performed without saturation for any phospholipids in the image.

### Biofilm formation assays

Static biofilm formation was assayed as described previously (18). Cell cultures in stationary phase were standardized to an absorbance of 1.0 ($\lambda$, 600 nm). The standardized cultures were inoculated 1/100 in 100 μL of Sistrom's succinate medium in a 96-well polystyrene microtiter plate that was incubated for 72 h at 30°C. Thereafter, the wells were washed with water to remove planktonic cells, and biofilms were labeled with 0.1% CV for 10 min at 25°C. After labeling, the wells were washed with water, and the retained CV was solubilized in 30% acetic acid. The amount of biofilm formed in each well was quantified by measuring the absorbance at $\lambda$, 550 nm.

To image biofilms, standardized cultures were inoculated 1/100 in Sistrom's succinate medium containing 5 μg/mL of Nile Red in a chamber slide with hydrophobic plastic surfaces (ibidi, Verona, WI) that was incubated for 72 h at 30°C. After washed with water, biofilms were imaged on an inverted Nikon Eclipse TE2000 epifluorescence microscope equipped with a shuttered black and white Andor iXonEM+ DU-897 EMCCD camera (Andor Technology, South Windsor, CT). Images were acquired using a ×40 objective (Nikon Plan Fluor ELWD 40×/0.60 DM) and the Metamorph software program (Version 7.5.6.0) (MDS Analytical Technologies, Downington, PA).

### Imaging bacterial cell attachment to surfaces

Stationary phase cell cultures were standardized to an absorbance of 1.0 (λ, 600 nm). The standardized cultures were inoculated 1/100 (~$1.25 \times 10^7$ cells) in Sistrom's succinate medium in a chamber slide with hydrophobic plastic surfaces (ibidi, Verona, WI) and incubated at 30°C. Cells attached to the surface were imaged at time 1, 24, 48 and 72 h after inoculation. Images were acquired as described in the previous section.

### Motility assays

Cell cultures in stationary phase were standardized to an absorbance of 1.0 (λ, 600 nm). 5 μL samples of the standardized cultures were placed on the surface of plates containing Sistrom's minimal medium with 0.25% agar (66). Diameters of swimming colonies were measured after incubation for 72 h at 30°C.

### Cell velocity measurements

Cell cultures in stationary phase were diluted 1/100 in Sistrom's succinate medium and a 20 μL aliquot of the diluted suspension was placed inside a ring of Apiezon M grease on pre-cleaned glass slides and sealed with a #1.5 mm glass cover slip. We imaged cell motility using a Nikon Eclipse 80i phase contrast upright microscope and a black and white Andor LucaS EMCCD camera (Andor Technology). Images were acquired using a ×40 ELWD dry objective (Nikon Plan Fluor 40/0.60 dry Ph2 DM). We collected videos consisting of 300 frames with a 33 ms exposure time at a rate of 30 frames/sec. Microscopy data were analyzed using MATLAB (MathWorks) by identifying the center of mass of each bacterium in successive frames and grouping those points together to create a cell trajectory from which we determined the mean cell velocity. We only used tracks that had more than 30 frames (i.e., more than 1 sec)—a minimal total length of 10 μm, and a minimal displacement of 5 μm. Cells that moved in a constant tumbling or wobbling manner or stuck to the coverslip were discarded from the analysis.

**qPCR**

Cells were grown to log phase and RNA was isolated as previously described (67). The RNA samples were then treated with RNase-free DNase (QIAGEN, Valencia, CA) and further purified using an RNeasy CleanUp kit (QIAGEN, Valencia, CA). cDNA synthesis was performed using a High Capacity RNA-to-cDNA Kit (Applied Biosystems, Foster city, CA). 5 ng of cDNA was used for a qPCR reaction. The Applied Biosystems 7500 Real-Time PCR System (Applied Biosystems, Foster city, CA) with SYBR Green chemistry was used to monitor amplification and to quantify the amount of PCR products. Relative quantitation of gene expression was calculated using the ΔΔCt method in which expression level of the *rpoZ* gene (encoding the Ω subunit of RNA polymerase) was used as an internal control. Primers used were: *rpoZ* forward (5′-TGA CAA GAA CCC TGT CGT G-3′), *rpoZ* reverse (5′-GCA GCT TCT CTT CGG ACA T-3′), *fliC* forward (5′-CTG ATT GAG ACC CAT GAC CT-3′), *fliC* reverse (5′-GTG AAC GAC CAG TTC AAC AC-3′), *fdp* forward (5′-GAG ATC GAC ACG CCA TTC A-3′), *fdp* reverse (5′-ACC GAG ATC CTG ACC TAT CA-3′).

**LPS extraction**

LPS was extracted as described previously (68). Briefly, cell cultures in stationary phase were standardized to an absorbance of 1.0 (λ, 600 nm). 1.5 mL of the standardized cultures was then collected by centrifugation and resuspended in 200 μL of sodium dodecyl sulfate (SDS)-buffer [2% β-mercaptoethanol (BME), 2% SDS and 10% glycerol in 50 mM Tris-HCl, pH 6.8]. Bacteria were boiled for 15 min and treated with proteinase K at 59°C for 3 h. 200 μL of ice-cold Tris-saturated phenol was added to the sample and the mixture was incubated at 65°C for 15 min with vortexing occasionally. 1 mL of diethyl ether was added to the mixture and two phases were created by centrifugation at 16,100 g for 10 min. The bottom layer containing LPS was collected, mixed with 200 μL of 2x SDS-buffer, and run on a 12% SDS-polyacrylamide gel. LPS was visualized by silver staining and quantitation of LPS content was performed using ImageJ.

**EPS extraction**

Cell cultures in stationary phase were standardized to an absorbance of 1.0 (λ, 600 nm). The standardized cultures were inoculated 1/100 in 1 mL of Sistrom's succinate medium in glass test tubes that were incubated for 72 h at 30°C with shaking. The cell cultures were centrifuged at 10,000 g for 20 min and the supernatants were mixed with three volumes of absolute ethanol for 2 h at -20°C to precipitate EPS. The precipitates were collected by centrifugation at 3,000 g for 30 min, washed once with 75% ethanol, and dried at room temperature overnight. The precipitated EPS was dissolved in water, separated on a 12% SDS-polyacrylamide gel using electrophoresis, and visualized by silver staining. The quantitation of EPS content was performed using ImageJ.

**Measurement of membrane permeability using fluorescence microscopy**

0.5 mL samples of *R. sphaeroides* cell cultures in stationary phase were collected, concentrated by centrifugation, and resuspended in 0.5 mL of 0.85% NaCl. PI at a final concentration of 20 μM was added to the cell suspension and samples were incubated for 10 min at 25°C. An aliquot (4 μL) of the cell suspension was imaged as described in the previous section. Measurement of the fluorescence intensity of each cell was performed using ImageJ.

**A22 treatment**

Cell cultures in stationary phase were standardized to an absorbance of 1.0 (λ, 600 nm). The standardized cultures were inoculated 1/100 in Sistrom's succinate medium containing 10 μg/mL A22, or dimethyl sulfoxide (DMSO) as a solvent control. The cells were grown in glass test tubes for 72 h at 30°C with shaking for cell shape analysis, or incubated in polystyrene microtiter plates for 72 h at 30°C for biofilm formation assays.

# ACKNOWLEDGMENTS

We thank the Ferguson-Miller laboratory (Michigan State University) for strain CL3 and the Raetz laboratory (Duke University) for strain BKT12. We thank Dr. Brian Burger and Rachelle Lemke for construction and provision of pIND4sp. This project leveraged technical assistance and input from George Auer, Manohary Rajendram, Julia Nepper and Piercen Oliver. T.-Y. Lin acknowledges a William H. Peterson fellowship from the Department of Biochemistry, University of Wisconsin-Madison. The National Science Foundation (MCB-1120832, DMR-1121288), NIH (1DP2OD008735), USDA (WIS01594), and the DOE Office of Science (BER DE-FC02-07ER64494) supported this research.

**Figure 1. Morphology of *R. sphaeroides* wild-type (WT) and CL3 cells at different growth phases.** *R. sphaeroides* WT and CL3 cells were grown aerobically in Sistrom's succinate medium at 30°C with shaking at 200 rpm until reaching log phase (absorbance of ~0.5; λ, 600 nm) or stationary phase (absorbance of ~1.3; λ, 600 nm). Each data point was determined by imaging 300 cells using phase contrast brightfield microscopy and using ImageJ to determine cell width and length. The values represent mean values ± standard deviations. Differences of the cell shape parameters between the two strains were analyzed by Student's *t test*. The P value for all parameters measured was $< 0.001$. Scale bar, 2 μm.

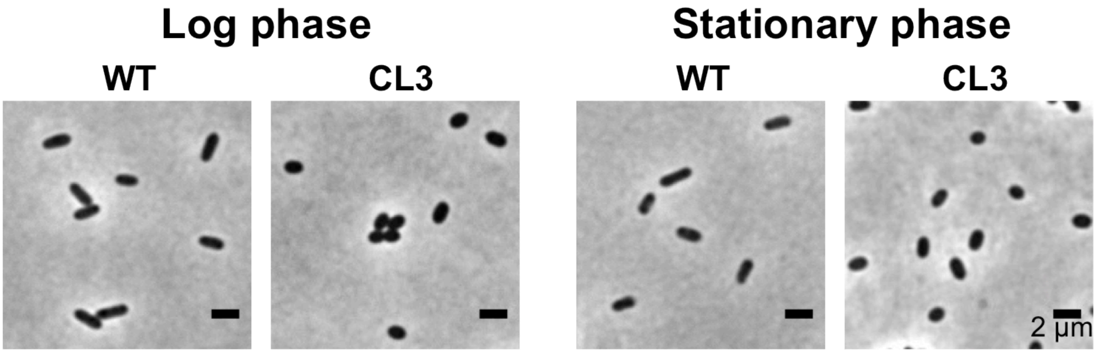

| | | | | |
|---|---|---|---|---|
| Length (µm) | 1.8 ± 0.3 | 1.4 ± 0.2 | 1.7 ± 0.4 | 1.4 ± 0.2 |
| Width (µm) | 0.8 ± 0.0 | 1.0 ± 0.1 | 0.7 ± 0.1 | 0.9 ± 0.1 |
| Aspect ratio | 2.3 ± 0.4 | 1.5 ± 0.2 | 2.3 ± 0.6 | 1.5 ± 0.3 |

**Figure 1**

**Figure 2. Complementation of the CL3 strain restores the rod shape of cells.** (A) Images depicting the morphology of CL3 cells harboring the empty vector pIND5sp (Ctrl), or expressing CL synthase from *cls*-pIND5sp (Cls). Each data point was determined by imaging 300 cells using phase contrast brightfield microscopy and using ImageJ to determine cell width and length. The values represent mean values ± standard deviations. Differences of the cell shape parameters between the two strains were analyzed by Student's *t test*. The P value for all parameters measured was < 0.001. Scale bar, 2 μm. (B) TLC analyses of lipids extracted from CL3 cells harboring the empty vector pIND5sp (Ctrl), or expressing CL synthase from *cls*-pIND5sp (Cls). (C) Levels of CL in CL3 cells harboring the empty vector pIND5sp (Ctrl), or expressing CL synthase from *cls*-pIND5sp (Cls). Each data point was determined from a TLC plate by quantifying the optical densitometry signal using ImageJ. The values represent mean values ± standard deviations obtained from three independent experiments. PE, phosphatidylethanolamine; PC, phosphatidylcholine; PG, phosphatidylglycerol; SQDG, sulfoquinovosyldiacylglycerol.

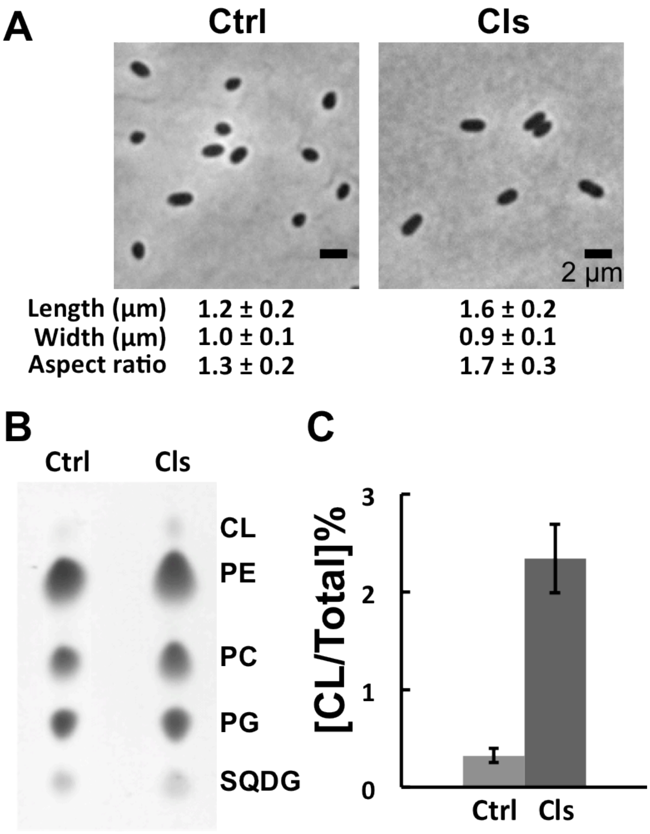

| | Ctrl | Cls |
|---|---|---|
| Length (µm) | 1.2 ± 0.2 | 1.6 ± 0.2 |
| Width (µm) | 1.0 ± 0.1 | 0.9 ± 0.1 |
| Aspect ratio | 1.3 ± 0.2 | 1.7 ± 0.3 |

**Figure 2**

**Figure 3. *R. sphaeroides* strain CL3 forms defective biofilms.** (A) Representative fluorescence micrographs of *R. sphaeroides* WT and CL3 biofilms grown on a chamber slide with hydrophobic plastic surfaces for 72 h at 30°C in Sistrom's succinate medium containing 5 μg/mL Nile Red. Scale bar, 5 μm. (B&C) *R. sphaeroides* WT and CL3 cells were grown on a chamber slide with hydrophobic plastic surfaces at 30°C in Sistrom's succinate medium. Images were acquired at 1 (see Figure S3), 24, 48 and 72 h after incubation using phase contrast brightfield microscopy. Image insets are magnified views of representative cells that demonstrate changes in cell length. Scale bar, 2 μm. The number of surface-attached cells was quantified at a time point of 1 h. The values represent mean values ± standard deviations obtained from three independent experiments. (D) Quantification of *R. sphaeroides* WT and CL3 biofilms, grown in wells of a polystyrene microtiter plate for 72 h at 30°C in Sistrom's succinate medium, followed by labeling with crystal violet (CV) Biofilm formation was quantified by measuring the absorbance of CV at $\lambda$, 550 nm. The values represent mean values ± standard deviations obtained from three independent experiments, each performed in 8 replicates. (E) Growth curves of *R. sphaeroides* WT and CL3 cells grown with shaking in glass test tubes at 30°C in Sistrom's succinate medium. The values represent mean values ± standard deviations obtained from three independent experiments.

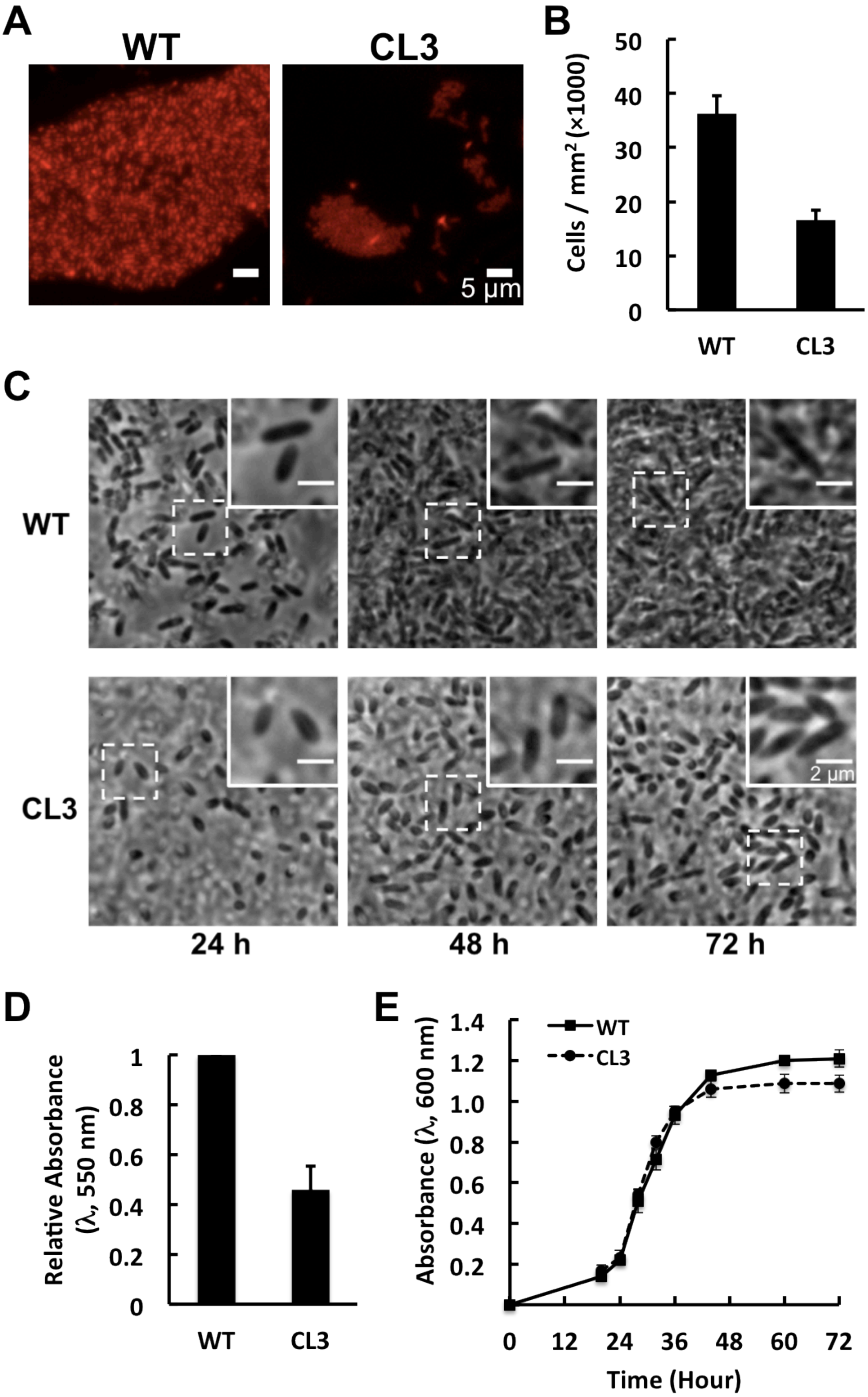
A
WT
CL3
5 µm
B
Cells / mm² (×1000)
50
40
30
20
10
0
WT
CL3
C
WT
CL3
2 µm
24 h
48 h
72 h
D
Relative Absorbance (λ, 550 nm)
1
0.8
0.6
0.4
0.2
0
WT
CL3
E
Absorbance (λ, 600 nm)
1.4
1.2
1.0
0.8
0.6
0.4
0.2
WT
CL3
0
12
24
36
48
60
72
Time (Hour)

Figure 3

**Figure 4. CL deficiency in *R. sphaeroides* does not cause defects in swimming motility, LPS production, *fdp* gene expression, EPS production, and membrane permeability.** (A) Motility of the *R. sphaeroides* WT and CL3 strains was assessed using the same soft-agar swimming plate. Scale bar, 10 mm. (B) Diameter of swimming colonies of the *R. sphaeroides* WT and CL3 strains on soft-agar swim plates. The values represent mean values ± standard deviations obtained from three independent experiments. (C) Box-and-whisker plots depicting the swimming velocities of individual *R. sphaeroides* WT and CL3 cells (n = 12). The extent of the box encompasses the interquartile range of the velocity, whiskers extend to maximum and minimum velocities, and the line within each box represents the median. (D) *fliC* gene expression in *R. sphaeroides* WT and CL3 cells assayed by qPCR. The values represent mean values ± standard deviations obtained from three independent experiments, each performed in triplicate. (E) LPS from *R. sphaeroides* WT and CL3 cells separated on an SDS-polyacrylamide gel and visualized by silver staining. (F) The LPS content of cells was quantified by densitometry using ImageJ. The values represent mean values ± standard deviations obtained from three independent experiments. (G) *fdp* gene expression in *R. sphaeroides* WT and CL3 cells assayed by qPCR. The values represent mean values ± standard deviations obtained from three independent experiments, each performed in triplicate. (H) The distribution of EPS extracted from planktonic cultures of *R. sphaeroides* WT and CL3 cells, separated on an SDS-polyacrylamide gel, and quantified by densitometry using ImageJ. The values represent mean values ± standard deviations obtained from three independent experiments. (I) Box-and-whisker plots depicting the membrane permeability measured for *R. sphaeroides* WT and CL3 strains using PI staining (n ≥ 100). The extent of the box encompasses the interquartile range of the PI fluorescence intensity, whiskers extend to maximum and minimum fluorescence

intensities, and the line within each box represents the median. Differences of the parameters between the *R. sphaeroides* WT and CL3 strains were analyzed by Student's *t test*. The P value for all parameters measured was > 0.5.

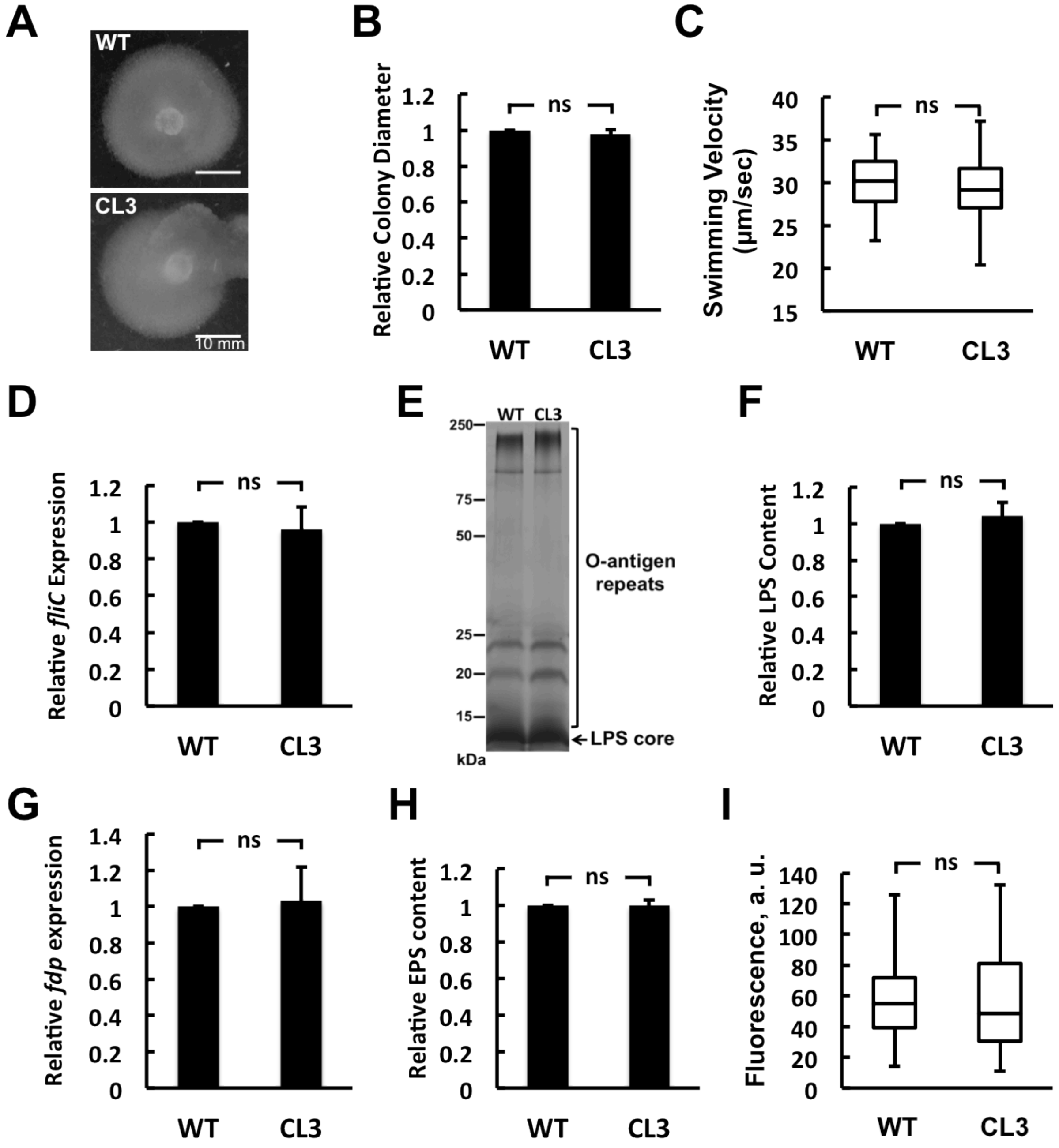
A
WT
CL3
10 mm
B
Relative Colony Diameter
1.2
1
0.8
0.6
0.4
0.2
0
ns
WT
CL3
C
Swimming Velocity (µm/sec)
40
35
30
25
20
15
ns
WT
CL3
D
Relative *fliC* Expression
1.2
1
0.8
0.6
0.4
0.2
0
ns
WT
CL3
E
WT
CL3
250
75
50
25
20
15
kDa
O-antigen repeats
LPS core
F
Relative LPS Content
1.2
1
0.8
0.6
0.4
0.2
0
ns
WT
CL3
G
Relative *fdp* expression
1.4
1.2
1
0.8
0.6
0.4
0.2
0
ns
WT
CL3
H
Relative EPS content
1.2
1
0.8
0.6
0.4
0.2
0
ns
WT
CL3
I
Fluorescence, a. u.
140
120
100
80
60
40
20
0
ns
WT
CL3

**Figure 4**

**Figure 5. Complementation of the CL3 strain restores biofilm formation.** (A) Images depicting the morphology of *R. sphaeroides* WT cells harboring the empty vector pIND5sp (Ctrl/WT), and CL3 cells expressing CL synthase from *cls*-pIND5sp (Cls/CL3). Each data point was determined by imaging 300 cells using phase contrast brightfield microscopy and using ImageJ to determine cell width and length. The values represent mean values ± standard deviations. Scale bar, 2 μm. (B) Levels of CL in *R. sphaeroides* WT cells harboring the empty vector pIND5sp (Ctrl/WT), and CL3 cells expressing CL synthase from *cls*-pIND5sp (Cls/CL3). Each data point was determined from a TLC plate by densitometry using ImageJ. The values represent mean values ± standard deviations obtained from three independent experiments. (C) Quantification of biofilms formed by *R. sphaeroides* WT cells harboring the empty vector pIND5sp (Ctrl/WT), and CL3 cells expressing CL synthase from *cls*-pIND5sp (Cls/CL3). Biofilms were grown on a polystyrene microtiter plate for 72 h at 30°C in Sistrom's succinate medium, followed by staining with CV. The extent of biofilm formation was determined by the absorbance of CV at $\lambda$, 550 nm. The values represent mean values ± standard deviations obtained from three independent experiments, each performed in 8 replicates. (D) Growth curves of *R. sphaeroides* WT cells harboring the empty vector pIND5sp (Ctrl/WT), and CL3 cells expressing CL synthase from *cls*-pIND5sp (Cls/CL3). Cells were grown with shaking in glass test tubes at 30°C in Sistrom's succinate medium. The values represent mean values ± standard deviations obtained from three independent experiments.

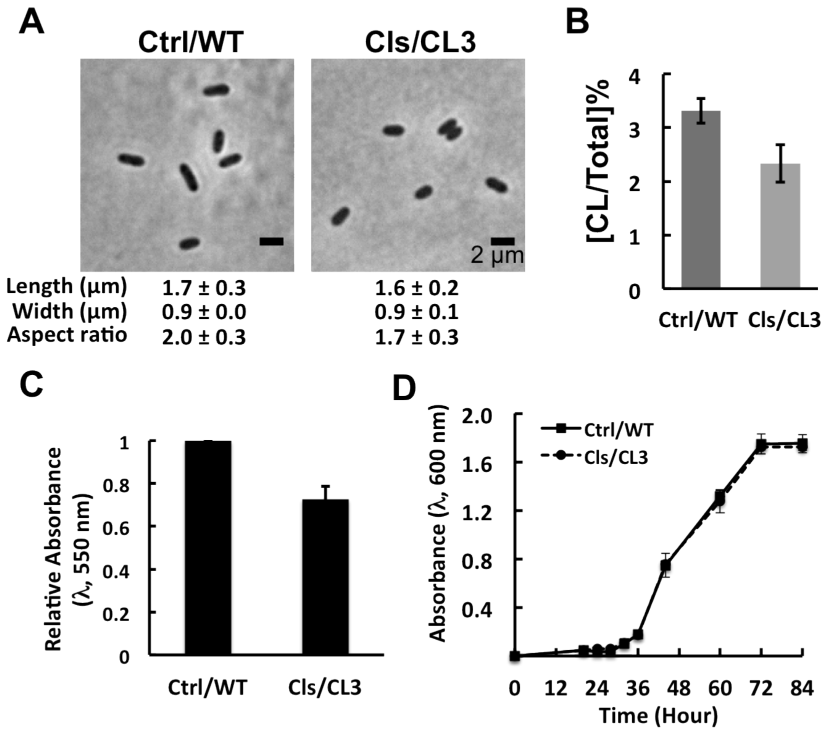
A
Ctrl/WT
Cls/CL3
2 µm
Length (µm) 1.7 ± 0.3 1.6 ± 0.2
Width (µm) 0.9 ± 0.0 0.9 ± 0.1
Aspect ratio 2.0 ± 0.3 1.7 ± 0.3
B
[CL/Total]%
0
1
2
3
4
Ctrl/WT
Cls/CL3
C
Relative Absorbance (λ, 550 nm)
0
0.2
0.4
0.6
0.8
1
Ctrl/WT
Cls/CL3
D
Absorbance (λ, 600 nm)
0.4
0.8
1.2
1.6
2.0
0
12
24
36
48
60
72
84
Time (Hour)
Ctrl/WT
Cls/CL3

**Figure 5**

**Figure 6. A22 treatment impairs biofilm formation.** (A) Images depicting the morphology of *R. sphaeroides* WT cells treated with DMSO or 10 µg/mL A22. Each data point was determined by imaging 300 cells using phase contrast brightfield microscopy and using ImageJ to determine cell width and length. The values represent mean values ± standard deviations. Differences of the cell shape parameters between the two treatments were analyzed by Student's *t test*. The P value for all parameters measured was < 0.001. Scale bar, 2 µm. (B) Quantification of biofilms formed by *R. sphaeroides* WT cells treated with DMSO or 10 µg/mL A22. Biofilms were grown on a polystyrene microtiter plate for 72 h at 30°C in Sistrom's succinate medium containing DMSO or 10 µg/mL A22, followed by staining with CV. The extent of biofilm formation was determined by the absorbance of CV at λ, 550 nm. The values represent mean values ± standard deviations obtained from three independent experiments, each performed in 8 replicates. (C) Growth curves of *R. sphaeroides* WT cells treated with DMSO or 10 µg/mL A22. Cells were grown with shaking in glass test tubes at 30°C in Sistrom's succinate medium containing DMSO or 10 µg/mL A22. The values represent mean values ± standard deviations obtained from three independent experiments.

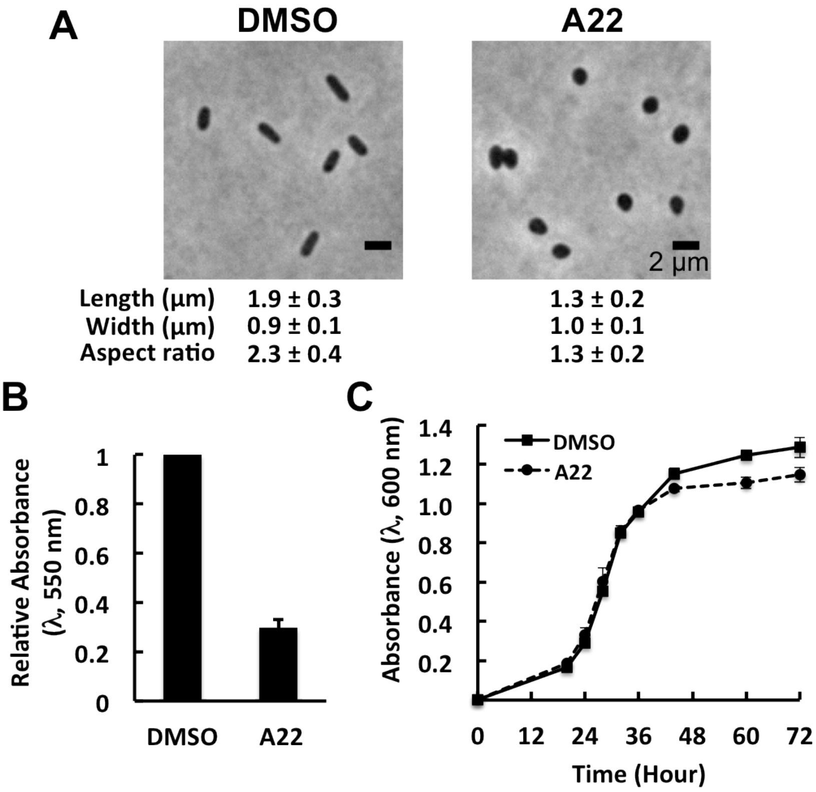

| | DMSO | A22 |
|---|---|---|
| Length (µm) | 1.9 ± 0.3 | 1.3 ± 0.2 |
| Width (µm) | 0.9 ± 0.1 | 1.0 ± 0.1 |
| Aspect ratio | 2.3 ± 0.4 | 1.3 ± 0.2 |

**Figure 6**

## Table 1. Bacterial strains and plasmids used in this study

| Strain or plasmid | Genotype or Description | Source or reference |
|---|---|---|
| ***E. coli* strains** | | |
| DH5α | *recA1 endA1 gyrA96 thi-1 hsdR17 supE44 relA1 deoR Δ(lacZYA-argF)U169 λ (φ80d lacZΔM15)* | Laboratory collection, CGSC#12384 |
| S17-1 | *recA pro hsdR* RP4-2-Tc::Mu-Km::Tn7 | 62 |
| ***R. sphaeroides* strains** | | |
| 2.4.1 | Wild-type | ATCC 17023 |
| CL3 | 2.4.1 containing a kanamycin resistance cassette in place of the genomic *cls* | 16 |
| **Plasmids** | | |
| pIND4 | IPTG-inducible expression vector for *R. sphaeroides*, kanamycin resistance | 61 |
| pIND4sp | A variant of pIND4 with a spectinomycin resistance cassette in place of the kanamycin resistance cassette | Unpublished |
| pIND5sp | A derivative of pIND4sp in which the NcoI site is replaced with an NdeI site. | This study |
| *cls*-pIND5sp | pIND5sp containing *cls* | This study |

## REFERENCES

1. **Garrett TR, Bhakoo M, Zhang Z.** 2008. Bacterial adhesion and biofilms on surfaces. Prog Nat Sci **18:**1049-1056.

2. **Dunne WM.** 2002. Bacterial Adhesion: Seen Any Good Biofilms Lately? Clin Microbiol Rev **15:**155-166.

3. **Renner LD, Weibel DB.** 2011. Physicochemical regulation of biofilm formation. MRS Bull **36:**347-355.

4. **Potera C.** 1999. Forging a link between biofilms and disease. Science **283:**1837, 1839.

5. **Young KD.** 2006. The selective value of bacterial shape. Microbiol Mol Biol Rev **70:**660-703.

6. **Boks NP, Norde W, van der Mei HC, Busscher HJ.** 2008. Forces involved in bacterial adhesion to hydrophilic and hydrophobic surfaces. Microbiology **154:**3122-3133.

7. **Tuson HH, Weibel DB.** 2013. Bacteria-surface interactions. Soft Matter **9:**4368-4380.

8. **Dang H, Lovell CR.** 2002. Numerical Dominance and Phylotype Diversity of Marine *Rhodobacter* Species during Early Colonization of Submerged Surfaces in Coastal Marine Waters as Determined by 16S Ribosomal DNA Sequence Analysis and Fluorescence In Situ Hybridization. Appl Environ Microbiol **68:**496-504.

9. **Wilkinson DA, Chacko SJ, Venien-Bryan C, Wadhams GH, Armitage JP.** 2011. Regulation of flagellum number by FliA and FlgM and role in biofilm formation by *Rhodobacter sphaeroides*. J Bacteriol **193:**4010-4014.

10. **Chory J, Donohue TJ, Varga AR, Staehelin LA, Kaplan S.** 1984. Induction of the photosynthetic membranes of *Rhodopseudomonas sphaeroides*: biochemical and morphological studies. J Bacteriol **159:**540-554.

11. **Russell NJ, Harwood JL.** 1979. Changes in the acyl lipid composition of photosynthetic bacteria grown under photosynthetic and non-photosynthetic conditions. Biochem J **181:**339-345.

12. **Huang KC, Mukhopadhyay R, Wingreen NS.** 2005. A curvature-mediated mechanism for localization of lipids to bacterial poles. PLoS Comput Biol doi:10.1371/journal.pcbi.0020151.eor:e151.

13. **Woese CR.** 1987. Bacterial evolution. Microbiol Rev **51:**221-271.

14. **Yeliseev AA, Krueger KE, Kaplan S.** 1997. A mammalian mitochondrial drug receptor functions as a bacterial "oxygen" sensor. Proc Natl Acad Sci U S A **94:**5101-5106.

15. **Mileykovskaya E, Dowhan W.** 2009. Cardiolipin membrane domains in prokaryotes and eukaryotes. Biochim Biophys Acta **1788:**2084-2091.

16. **Zhang X, Tamot B, Hiser C, Reid GE, Benning C, Ferguson-Miller S.** 2011. Cardiolipin deficiency in *Rhodobacter sphaeroides* alters the lipid profile of membranes and of crystallized cytochrome oxidase, but structure and function are maintained. Biochemistry **50:**3879-3890.

17. **Spiekermann P, Rehm BH, Kalscheuer R, Baumeister D, Steinbuchel A.** 1999. A sensitive, viable-colony staining method using Nile red for direct screening of bacteria that accumulate polyhydroxyalkanoic acids and other lipid storage compounds. Arch Microbiol **171:**73-80.

18. **O'Toole GA.** 2011. Microtiter dish biofilm formation assay. J Vis Exp doi:10.3791/2437.

19. **Merritt PM, Danhorn T, Fuqua C.** 2007. Motility and chemotaxis in *Agrobacterium tumefaciens* surface attachment and biofilm formation. J Bacteriol **189:**8005-8014.

20. **O'Toole GA, Kolter R.** 1998. Flagellar and twitching motility are necessary for *Pseudomonas aeruginosa* biofilm development. Mol Microbiol **30:**295-304.

21. **Pratt LA, Kolter R.** 1998. Genetic analysis of *Escherichia coli* biofilm formation: roles of flagella, motility, chemotaxis and type I pili. Mol Microbiol **30:**285-293.

22. **Anderson JK, Smith TG, Hoover TR.** 2010. Sense and sensibility: flagellum-mediated gene regulation. Trends Microbiol **18:**30-37.

23. **Walker SL, Redman JA, Elimelech M.** 2004. Role of Cell Surface Lipopolysaccharides in *Escherichia coli* K12 adhesion and transport. Langmuir **20:**7736-7746.

24. **Abu-Lail NI, Camesano TA.** 2003. Role of lipopolysaccharides in the adhesion, retention, and transport of *Escherichia coli* JM109. Environ Sci Technol **37:**2173-2183.

25. **Kannenberg EL, Carlson RW.** 2001. Lipid A and O-chain modifications cause *Rhizobium* lipopolysaccharides to become hydrophobic during bacteroid development. Mol Microbiol **39:**379-391.

26. **Makin SA, Beveridge TJ.** 1996. The influence of A-band and B-band lipopolysaccharide on the surface characteristics and adhesion of *Pseudomonas aeruginosa* to surfaces. Microbiology **142 ( Pt 2):**299-307.

27. **Moody RG, Williamson MP.** 2013. Structure and function of a bacterial Fasciclin I Domain Protein elucidates function of related cell adhesion proteins such as TGFBIp and periostin. FEBS Open Bio **3:**71-77.

28. **Costerton JW, Cheng KJ, Geesey GG, Ladd TI, Nickel JC, Dasgupta M, Marrie TJ.** 1987. Bacterial biofilms in nature and disease. Annu Rev Microbiol **41:**435-464.

29. **Parsek MR, Greenberg EP.** 2005. Sociomicrobiology: the connections between quorum sensing and biofilms. Trends Microbiol **13:**27-33.

30. **Li YH, Tian X.** 2012. Quorum sensing and bacterial social interactions in biofilms. Sensors (Basel) **12:**2519-2538.

31. **McDougald D, Rice SA, Barraud N, Steinberg PD, Kjelleberg S.** 2012. Should we stay or should we go: mechanisms and ecological consequences for biofilm dispersal. Nat Rev Microbiol **10:**39-50.

32. **Bean GJ, Flickinger ST, Westler WM, McCully ME, Sept D, Weibel DB, Amann KJ.** 2009. A22 disrupts the bacterial actin cytoskeleton by directly binding and inducing a low-affinity state in MreB. Biochemistry **48:**4852-4857.

33. **Iwai N, Nagai K, Wachi M.** 2002. Novel S-benzylisothiourea compound that induces spherical cells in *Escherichia coli* probably by acting on a rod-shape-determining protein(s) other than penicillin-binding protein 2. Biosci Biotechnol Biochem **66:**2658-2662.

34. **Lopez CS, Alice AF, Heras H, Rivas EA, Sanchez-Rivas C.** 2006. Role of anionic phospholipids in the adaptation of *Bacillus subtilis* to high salinity. Microbiology **152:**605-616.

35. **MacGilvray ME, Lapek JD, Jr., Friedman AE, Quivey RG, Jr.** 2012. Cardiolipin biosynthesis in *Streptococcus mutans* is regulated in response to external pH. Microbiology **158:**2133-2143.

36. **Tsai M, Ohniwa RL, Kato Y, Takeshita SL, Ohta T, Saito S, Hayashi H, Morikawa K.** 2011. *Staphylococcus aureus* requires cardiolipin for survival under conditions of high salinity. BMC Microbiol **11:**13.

37. **Romantsov T, Helbig S, Culham DE, Gill C, Stalker L, Wood JM.** 2007. Cardiolipin promotes polar localization of osmosensory transporter ProP in *Escherichia coli*. Mol Microbiol **64:**1455-1465.

38. **Hsieh CW, Lin TY, Lai HM, Lin CC, Hsieh TS, Shih YL.** 2010. Direct MinE-membrane interaction contributes to the proper localization of MinDE in *E. coli*. Mol Microbiol **75:**499-512.

39. **Haines TH, Dencher NA.** 2002. Cardiolipin: a proton trap for oxidative phosphorylation. FEBS Lett **528:**35-39.

40. **Gold VA, Robson A, Bao H, Romantsov T, Duong F, Collinson I.** 2010. The action of cardiolipin on the bacterial translocon. Proc Natl Acad Sci U S A **107:**10044-10049.

41. **Renner LD, Weibel DB.** 2011. Cardiolipin microdomains localize to negatively curved regions of *Escherichia coli* membranes. Proc Natl Acad Sci U S A **108:**6264-6269.

42. **Wakeham MC, Sessions RB, Jones MR, Fyfe PK.** 2001. Is there a conserved interaction between cardiolipin and the type II bacterial reaction center? Biophys J **80:**1395-1405.

43. **McAuley KE, Fyfe PK, Ridge JP, Isaacs NW, Cogdell RJ, Jones MR.** 1999. Structural details of an interaction between cardiolipin and an integral membrane protein. Proc Natl Acad Sci U S A **96:**14706-14711.

44. **Distler AM, Allison J, Hiser C, Qin L, Hilmi Y, Ferguson-Miller S.** 2004. Mass spectrometric detection of protein, lipid and heme components of cytochrome c oxidase from *R. sphaeroides* and the stabilization of non-covalent complexes from the enzyme. Eur J Mass Spectrom (Chichester, Eng) **10:**295-308.

45. **Svensson-Ek M, Abramson J, Larsson G, Tornroth S, Brzezinski P, Iwata S.** 2002. The X-ray crystal structures of wild-type and EQ(I-286) mutant cytochrome c oxidases from *Rhodobacter sphaeroides*. J Mol Biol **321:**329-339.

46. **Oliver PM, Crooks JA, Leidl M, Yoon EJ, Saghatelian A, Weibel DB.** 2014. Localization of anionic phospholipids in *Escherichia coli* cells. J Bacteriol **196:**3386-3398.

47. **Romantsov T, Guan Z, Wood JM.** 2009. Cardiolipin and the osmotic stress responses of bacteria. Biochim Biophys Acta **1788:**2092-2100.

48. **Shibuya I, Miyazaki C, Ohta A.** 1985. Alteration of phospholipid composition by combined defects in phosphatidylserine and cardiolipin synthases and physiological consequences in *Escherichia coli*. J Bacteriol **161:**1086-1092.

49. **Tan BK, Bogdanov M, Zhao J, Dowhan W, Raetz CR, Guan Z.** 2012. Discovery of a cardiolipin synthase utilizing phosphatidylethanolamine and phosphatidylglycerol as substrates. Proc Natl Acad Sci U S A **109:**16504-16509.

50. **Kjelleberg S, Hermansson M, Marden P, Jones GW.** 1987. The transient phase between growth and nongrowth of heterotrophic bacteria, with emphasis on the marine environment. Annu Rev Microbiol **41:**25-49.

51. **Lange R, Hengge-Aronis R.** 1991. Growth phase-regulated expression of bolA and morphology of stationary-phase *Escherichia coli* cells are controlled by the novel sigma factor sigma S. J Bacteriol **173:**4474-4481.

52. **Persat A, Stone HA, Gitai Z.** 2014. The curved shape of Caulobacter crescentus enhances surface colonization in flow. Nat Commun **5:**3824.

53. **Huber B, Riedel K, Kothe M, Givskov M, Molin S, Eberl L.** 2002. Genetic analysis of functions involved in the late stages of biofilm development in *Burkholderia cepacia* H111. Mol Microbiol **46:**411-426.

54. **Watnick PI, Kolter R.** 1999. Steps in the development of a Vibrio cholerae El Tor biofilm. Mol Microbiol **34:**586-595.

55. **Puskas A, Greenberg EP, Kaplan S, Schaefer AL.** 1997. A quorum-sensing system in the free-living photosynthetic bacterium *Rhodobacter sphaeroides*. J Bacteriol **179:**7530-7537.

56. **van den Ent F, Amos LA, Lowe J.** 2001. Prokaryotic origin of the actin cytoskeleton. Nature **413:**39-44.

57. **Dominguez-Escobar J, Chastanet A, Crevenna AH, Fromion V, Wedlich-Soldner R, Carballido-Lopez R.** 2011. Processive movement of MreB-associated cell wall biosynthetic complexes in bacteria. Science **333:**225-228.

58. **Figge RM, Divakaruni AV, Gober JW.** 2004. MreB, the cell shape-determining bacterial actin homologue, co-ordinates cell wall morphogenesis in *Caulobacter crescentus*. Mol Microbiol **51:**1321-1332.

59. **Reimold C, Defeu Soufo HJ, Dempwolff F, Graumann PL.** 2013. Motion of variable-length MreB filaments at the bacterial cell membrane influences cell morphology. Mol Biol Cell **24:**2340-2349.

60. **Sistrom WR.** 1960. A requirement for sodium in the growth of *Rhodopseudomonas spheroides*. J Gen Microbiol **22:**778-785.

61. **Ind AC, Porter SL, Brown MT, Byles ED, de Beyer JA, Godfrey SA, Armitage JP.** 2009. Inducible-expression plasmid for *Rhodobacter sphaeroides* and *Paracoccus denitrificans*. Appl Environ Microbiol **75:**6613-6615.

62. **Simon R, U. Priefer, and A. Puhler.** 1983. A broad host range mobilization system for in vitro genetic engineering: transposon mutagenesis in gram negative bacteria. Nat Biotechnol **1:**784-791.

63. **Davis J, Donohue TJ, Kaplan S.** 1988. Construction, characterization, and complementation of a Puf- mutant of *Rhodobacter sphaeroides*. J Bacteriol **170:**320-329.

64. **Bligh EG, Dyer WJ.** 1959. A rapid method of total lipid extraction and purification. Can J Biochem Physiol **37:**911-917.

65. **De Leo V, Catucci L, Ventrella A, Milano F, Agostiano A, Corcelli A.** 2009. Cardiolipin increases in chromatophores isolated from *Rhodobacter sphaeroides* after osmotic stress: structural and functional roles. J Lipid Res **50:**256-264.

66. **Suaste-Olmos F, Domenzain C, Mireles-Rodriguez JC, Poggio S, Osorio A, Dreyfus G, Camarena L.** 2010. The flagellar protein FliL is essential for swimming in *Rhodobacter sphaeroides*. J Bacteriol **192:**6230-6239.

67. **Tavano CL, Podevels AM, Donohue TJ.** 2005. Identification of genes required for recycling reducing power during photosynthetic growth. J Bacteriol **187:**5249-5258.

68. **Davis MR, Jr., Goldberg JB.** 2012. Purification and visualization of lipopolysaccharide from Gram-negative bacteria by hot aqueous-phenol extraction. J Vis Exp doi:10.3791/3916.

## SUPPORTING INFORMATION

## RESULTS

***RSP_0113* does not encode a cardiolipin synthase in *R. sphaeroides.***

To investigate the origins of the residual 10% of the cardiolipin (CL) in the CL3 mutant, we performed a BLAST search and found another candidate *CL synthase* (*cls*) gene in *R. sphaeroides*: *RSP_0113* (GenBank entry YP_353188) (1, 2). RSP_0113 is 25% identical and 41% similar to the amino acid sequence of *Escherichia coli* CL synthase, and contains a phospholipase D domain that is a characteristic motif found in CL synthases. We cloned the *RSP_0113* gene into an *E. coli* expression plasmid pTrc99A and an *R. sphaeroides* expression plasmid pIND4, and expressed it in the *E. coli* CL-deficient mutant BKT12 (3) and *R. sphaeroides* CL3, respectively. We were unable to detect CL in phospholipids extracted from BKT12 cells harboring a plasmid-encoded *RSP_0113* gene or nor were we able to detect increased CL in analogous CL3 transformants (data not shown) by thin-layer chromatogram. These results suggest that RSP_0113 is not a CL synthase in either bacterium and leave us uncertain of the origins of the residual 10% CL in *R. sphaeroides* CL3.

## EXPERIMENTAL PROCEDURES

### Confocal scanning laser microscopy of biofilms.

Stationary phase cell cultures were standardized to an absorbance of 1.0 (λ, 600 nm). The standardized cultures were inoculated 1/100 in Sistrom’s succinate medium containing 5 μg/ml Nile Red in a chamber slide with hydrophobic plastic surfaces (ibidi, Verona, WI) and incubated for 72 h at 30°C. After washed with water to remove planktonic cells, biofilms were imaged on a Nikon A1R- Si confocal microscope. Images were processed with NIS-Elements AR software.

**Figure S1. Nile Red does not change cell shape and impede cell growth of *R. sphaeroides*.** (A) Images depicting the morphology of *R. sphaeroides* wild-type (WT) and CL3 cells grown aerobically in Sistrom's succinate medium containing 5 μg/mL Nile Red at 30°C with shaking at 200 rpm. Each data point was determined by imaging 300 cells using phase contrast brightfield microscopy and using ImageJ to determine cell width and length. The values represent mean values ± standard deviations. Differences of the cell shape parameters between the two strains were analyzed by Student's *t test*. The P value for all parameters measured was $< 0.001$. Scale bar, 2 μm. (B) Growth curves of *R. sphaeroides* WT and CL3 cells grown with shaking in glass test tubes at 30°C in Sistrom's succinate medium containing 5 μg/mL Nile Red. The values represent mean values ± standard deviations obtained from three independent experiments. Although a ~0.1 difference in absorbance ($\lambda$, 600 nm) was observed at stationary phase, colony-forming units (CFUs) of the WT and CL3 strains were not significantly different (WT: $1.6 \times 10^9$ CFU/mL, CL3: $1.5 \times 10^9$ CFU/mL).

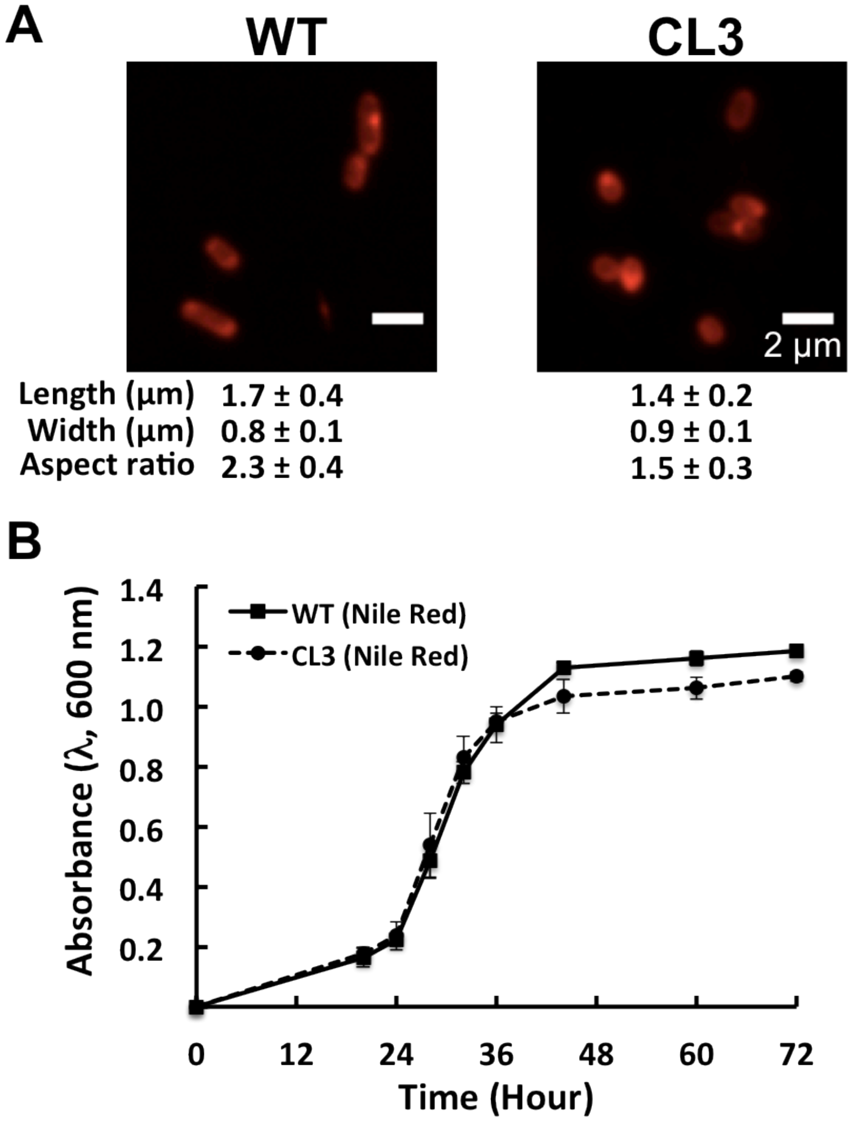

| | WT | CL3 |
|---|---|---|
| Length (µm) | 1.7 ± 0.4 | 1.4 ± 0.2 |
| Width (µm) | 0.8 ± 0.1 | 0.9 ± 0.1 |
| Aspect ratio | 2.3 ± 0.4 | 1.5 ± 0.3 |

**Figure S1**

**Figure S2. Confocal laser scanning micrographs of *R. sphaeroides* WT and CL3 biofilms.** *R. sphaeroides* WT and CL3 biofilms were grown on a chamber slide with hydrophobic plastic surfaces for 72 h at 30°C in Sistrom's succinate medium containing 5 μg/ml Nile Red and imaged using a confocal microscope. Upper panels: orthogonal views. Scale bar, 10 μm. Lower panels: 3-D reconstructions of confocal microscopy images. The thickness of *R. sphaeroides* WT biofilms was 20 μm. In contrast, the CL3 strain formed biofilms that were typically ~9-μm thick.

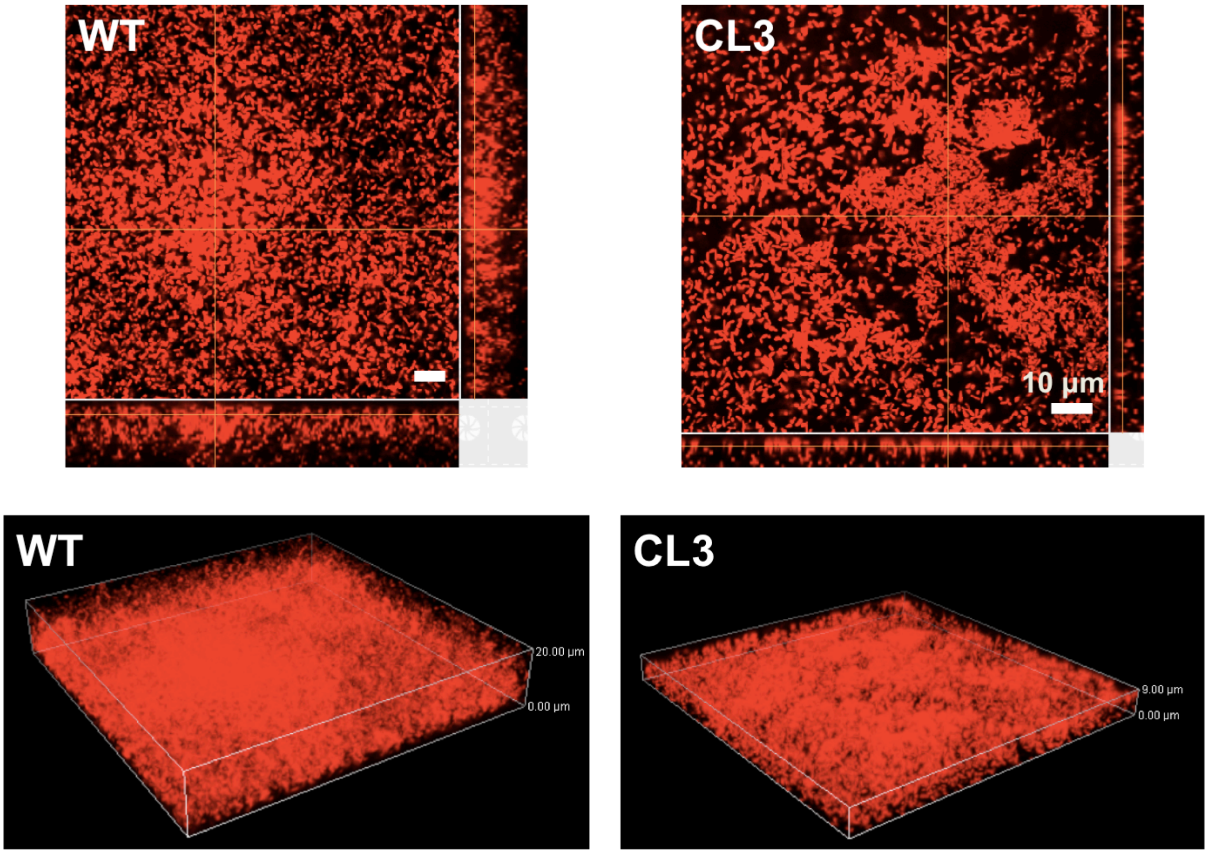

**Figure S2**

**Figure S3.** Representative micrographs of *R. sphaeroides* WT and CL3 cells attached to surfaces. *R. sphaeroides* WT and CL3 cells were grown on a chamber slide with hydrophobic plastic surfaces at 30°C in Sistrom's succinate medium. Cells attached to the surface were imaged at 1 h after inoculation. Images were acquired using phase contrast brightfield microscopy. Scale bar, 2 μm.

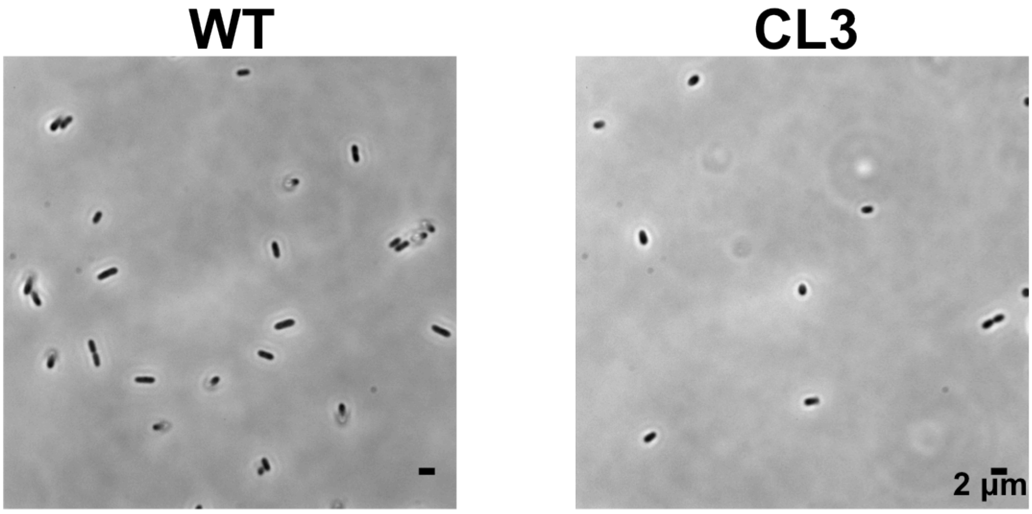

Figure S3

**Figure S4. Quantification of *R. sphaeroides* WT and CL3 biofilms grown in wells of a glass bottom microtiter plate.** Biofilms were grown on a glass bottom microtiter plate (MatTek, Ashland, MA) for 72 h at 30°C in Sistrom's succinate medium, followed by staining with crystal violet (CV). The extent of biofilm formation was determined by the absorbance of CV at $\lambda$, 550 nm. The values represent mean values ± standard deviations obtained from three independent experiments, each performed in 8 replicates. *R. sphaeroides* strain CL3 displayed a 50% reduction in biofilm formation compared with the WT strain after 72 h of incubation.

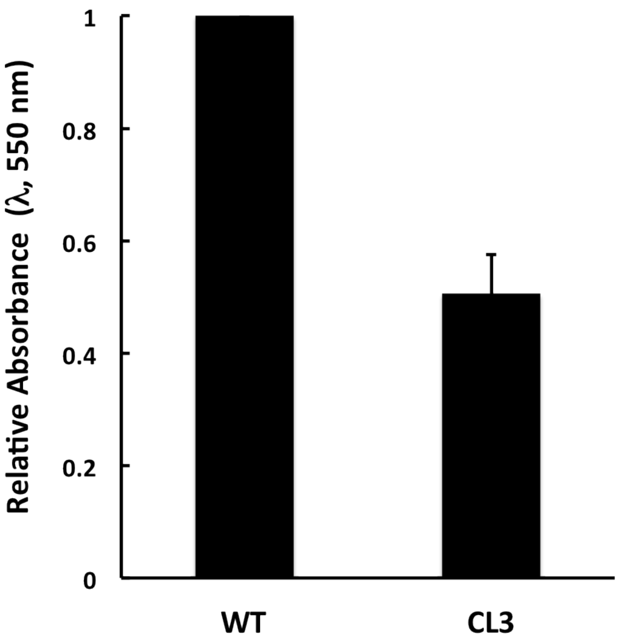

Figure S4

**Figure S5. Exopolysaccharides (EPS) extracted from planktonic cultures of *R. sphaeroides* WT and CL3 cells.** Cells were grown with shaking in glass test tubes for 72 h at 30°C in Sistrom's succinate medium. The EPS in growth media was precipitated by adding absolute ethanol to a final concentration of 75%, separated on an SDS-polyacrylamide gel using electrophoresis, and visualized by silver staining. EPS from both *R. sphaeroides* strains displayed similar banding patterns and was present in similar amounts.

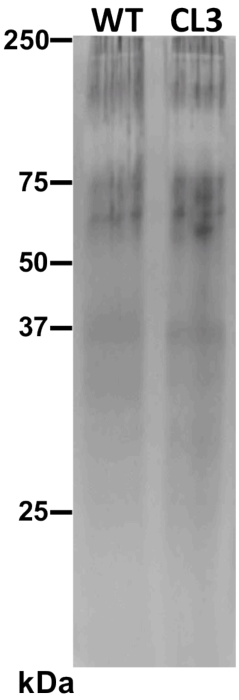

**Figure S5**

# REFERENCES

1. **Altschul SF, Madden TL, Schaffer AA, Zhang J, Zhang Z, Miller W, Lipman DJ.** 1997. Gapped BLAST and PSI-BLAST: a new generation of protein database search programs. Nucleic Acids Res **25:**3389-3402.

2. **Kontur WS, Schackwitz WS, Ivanova N, Martin J, Labutti K, Deshpande S, Tice HN, Pennacchio C, Sodergren E, Weinstock GM, Noguera DR, Donohue TJ.** 2012. Revised sequence and annotation of the *Rhodobacter sphaeroides* 2.4.1 genome. J Bacteriol **194:**7016-7017.

3. **Tan BK, Bogdanov M, Zhao J, Dowhan W, Raetz CR, Guan Z.** 2012. Discovery of a cardiolipin synthase utilizing phosphatidylethanolamine and phosphatidylglycerol as substrates. Proc Natl Acad Sci U S A **109:**16504-16509.

# CHAPTER 3

# Cardiolipin contributes to bacterial cell shape determination by regulating peptidoglycan precursor biosynthesis

This chapter was adapted from:

Ti-Yu Lin, William S. Gross, George K. Auer, Kaitlin Schaefer, Suzanne Walker,

Daniel Kahne and Douglas B. Weibel

Manuscript in Preparation

## ABSTRACT

Cardiolipin (CL) is an anionic phospholipid that plays an important role in bacterial cell biology. We previously observed that a *Rhodobacter sphaeroides* mutant (Δ*cls*) devoid of CL changes cell shape from a rod to an ellipsoid. In this study, we use chemical biology approach to investigate the molecular mechanisms by which CL regulates bacterial cell shape. Using fluorescent D-amino acids labeling and ultra performance liquid chromatography-mass spectrometry, we found that *R. sphaeroides* cells treated with antibiotics inhibiting peptidoglycan (PG) precursor biosynthesis had phenotypes similar to *R. sphaeroides* Δ*cls* cells (including: cell shape, PG growth mode, and PG composition), suggesting that a CL deficiency in *R. sphaeroides* causes a reduction in the production of PG precursors and cell elongation. MurG is a glycosyltransferase that performs the last step of PG precursor biosynthesis. We characterize the interaction of MurG with membranes in vivo and in vitro and demonstrate that MurG preferentially interacts with CL. We found that *R. sphaeroides* Δ*cls* cells synthesized a reduced amount of PG precursors compared to wild-type cells. Overexpression of MurG in *R. sphaeroides* Δ*cls* cells restored their rod shape, indicating that the shape change caused by a CL deficiency is a result of a decrease in MurG activity. We also found that the *R. sphaeroides* Δ*cls* mutant is susceptible to drugs targeting PG synthesis compared to the wild-type strain. We suggest CL biosynthesis as a potential antibiotic target.

# INTRODUCTION

Bacterial cells have a wide variety of shapes that play roles in regulating bacterial functions, including: motility, adhesion, replication, pathogenicity, and evasion of the mammalian immune system (1, 2). Bacterial cell shape arises from the morphology of the cell wall, which is composed of a layer of peptidoglycan (PG) that surrounds the cytoplasmic membrane and resists the osmotic pressure and other mechanical forces applied to cells by their environments (3, 4). Antibiotic development has paid careful attention to the underlying machinery controlling cell shape due to its connection to the PG and the catastrophic effect of inhibiting PG synthesis (5, 6). In Gram-negative bacteria, PG is synthesized in three distinct steps (Figure 1). 1) Monosaccharide-peptide precursors are synthesized in the cytoplasm through the action of seven enzymes, MurABCDEF and DdlA. 2) A lipid linker is attached to the monosaccharide-peptide precursor by MraY to tether it to the inner leaflet of the cytoplasmic membrane (referred to as lipid I), a second sugar is attached to the lipid I by MurG to create a disaccharide-peptide precursor (referred to as lipid II), and the molecule is flipped by MurJ to the outer leaflet. 3) Lipid II is polymerized by a glycosyltransferase (GTase) and the nascent glycan strands are incorporated into the existing PG in the periplasm by a transpeptidase (TPase) that crosslinks peptides. In rod-shaped bacteria, PG synthesis occurs at different sites of the cell at different stages of the cell cycle. During cell division, FtsZ initiates the organization of the divisome containing PBP1b (a bifunctional GTase and TPase) and

PBP3 (a TPase that requires FtsW for its function), which perform PG assembly at the division site. During cell elongation, MreB forms a scaffold for assembly of an elongasome containing PBP1a (a bifunctional GTase and TPase) and PBP2 (a TPase that requires RodA for its activity), which catalyze PG assembly along the sidewalls of the cell (3, 4).

The phospholipid membrane is another cellular structure that may play an important role in determining bacterial shape by regulating PG synthesis. The contribution of the cytoplasmic membrane in regulating bacterial cell morphology remains at-large. Previously, we found a mutant of the Gram-negative, rod-shaped bacterium *Rhodobacter sphaeroides* that lacks the ability to produce the intrinsically curved anionic phospholipid cardiolipin (CL) creates cells with an ellipsoidal shape (7). As this change in cell morphology was not observed in other rod-shaped bacterial strains depleted of CL, including: *Escherichia coli* and *Bacillus subtilis* (8, 9), we view *R. sphaeroides* as a potential model to explore the role of the cytoplasmic membrane in bacterial shape determination. In this study, we demonstrate that the common rod shape-determining strategy of many bacteria (i.e., MreB-directed cell elongation) is also adopted by *R. sphaeroides*. Despite a reduction in the elongation of its cylindrical cell body, the CL-deficient mutant of *R. sphaeroides* retains an elongasome with normal function. Surprisingly, we found that CL takes part in bacterial shape determination by regulating the biosynthesis of PG precursor. We describe research supporting the hypothesis that a CL deficiency in *R. sphaeroides* reduces the supply of PG precursors to the elongasome for PG assembly at the sidewalls of the cell, which results in a change of cell shape.

## RESULTS

### CL plays a role in cell shape determination.

The *R. sphaeroides* cell membrane contains four major types of phospholipids, including: phosphatidylethanolamine (PE), phosphatidylcholine (PC), phosphatidylglycerol (PGL) and CL in a ratio of approximately 5 : 2 : 2.4 : 0.6 (PE : PC : PGL : CL) by weight (10). Previously, we demonstrated that a CL-deficient mutant of *R. sphaeroides*, in which the *CL synthase* gene is deleted (Δ*cls*), produces a limited amount of CL (0.5% of total lipids) and displays an ellipsoidal cell shape phenotype with a characteristic decrease (20%) in cell length compared to the wild-type (wt) strain, in which CL accounts for 5.6% of total lipids (Figure 2A, B) (7, 10). To investigate whether the change in cell shape of the *R. sphaeroides* Δ*cls* mutant is due to an increased cell division rate (relative to cell growth), we performed single cell time-lapse imaging on both *R. sphaeroides* wt and Δ*cls* cells (Figure S1). We imaged cells, tracked their growth directly between cell division events, and found that the wt and Δ*cls* strains had a comparable doubling time of ~150 min. The Δ*cls* mutant, however, displayed a 25% decrease in the rate of cell elongation compared to the wt strain, which suggested to us that the morphological change in the *R. sphaeroides* Δ*cls* mutant is due to a defect in cell elongation. Complementation of the Δ*cls* mutant by ectopically expressing CL synthase in cells from the IPTG (isopropyl-β-D-thiogalactopyranoside)-inducible expression vector pIND (11) increased the concentration of CL to 2.3% of total lipids and restored the cell elongation rate by

13% (Figure S1), suggesting that CL is important for the establishment of the rod shape of *R. sphaeroides* cells.

### CL deficiency does not impair elongasome function.

MreB is a bacterial cytoskeletal protein that is homologous to eukaryotic actin (12). In rod-shaped bacteria, MreB polymerizes into filamentous structures on the inner leaflet of the cytoplasmic membrane and recruits elongasome components, including the cell-elongation specific TPase PBP2. MreB filaments move circumferentially around the length of the cell with a velocity that is correlated to the rate of PG assembly and in an orientation that may guide elongation of the cell (13-15). In *R. sphaeroides*, MreB, MreC, MreD, PBP2, and RodA are thought to be encoded at the same locus (Figure S2A) (16). MreB requires MreC and MreD for its cellular localization and PBP2 requires RodA for its TPase activity (3). RodA has recently been reported to also possess a GTase activity (17, 18). To investigate whether *R. sphaeroides* uses this shape-determining strategy of the elongasome summarized above, we used a chemical biology approach. We treated *R. sphaeroides* cells with the small molecule inhibitors S-(3,4-dichlorobenzyl)isothiourea (A22; binds MreB and disassembles MreB filaments) and mecillinam (MEC; binds PBP2 and inhibits its TPase activity required for cell elongation). The MIC of A22 is 60 μg/mL and the MIC of MEC is 3 μg/mL for *R. sphaeroides*. Sub-MIC concentrations of both drugs (A22: 10 μg/mL; MEC: 0.5 μg/mL) did not cause significant defects in *R. sphaeroides* cell growth and decreased cell length (A22: 40%; MEC: 30%), which matches the phenotype of other rod-shaped bacteria treated with these compounds (3) and suggests a conserved cell elongation machinery (Figure 2C, D). The similarity between the phenotype of *R. sphaeroides* Δ*cls* cells (i.e., shorter cell length) and those of *R. sphaeroides* wt cells treated with A22 and MEC led us to hypothesize that the structure and function of the elongasome may be altered in the *R. sphaeroides* Δ*cls* mutant and PG assembly is inhibited at the sidewalls of the cell. To test this hypothesis, we first compared expression levels of the genes coding for elongasome components in *R. sphaeroides* wt and Δ*cls* cells using real-time PCR (qPCR). We found no significant difference between the expression levels of elongasome genes in wt and Δ*cls* cells (Figure S2B). We also treated *R. sphaeroides* cells with the PBP1a inhibitor cefsulodin to inhibit its TPase activity, the MIC of which is 20 μg/mL. A sub-MIC concentration (5 μg/mL) of the drug caused neither significant growth defects nor a change in cell shape (Figure S3), suggesting a redundant role of PBP1a in cell elongation (18). We next investigated whether the subcellular localization of MreB is altered in the *R. sphaeroides* Δ*cls* mutant.

In *E. coli*, MreB filaments directly associate with the cytoplasmic membrane through an N-terminal amphipathic helix (19). Sequence alignment revealed that this membrane-binding feature is conserved in *R. sphaeroides* MreB (Helix 1, residues 1-9) (Figure 3A, S4). To investigate whether *R. sphaeroides* MreB interacts with the membrane, we sought to purify *R. sphaeroides* MreB and perform a liposome-pelleting assay. However, despite substantial efforts, we were unable to purify *R. sphaeroides* MreB and a mutant lacking the N-terminal helix due to the insolubility of both proteins (Figure S5). This observation raised the question of whether *R. sphaeroides* MreB has other membrane-binding motifs. We tested this using the prediction software AMPHIPASEEK and found that *R. sphaeroides* MreB may form an internal amphipathic helix (Helix 2, residues 87-97) (Figure 3A, S6). To test whether the two *R. sphaeroides* MreB helices interact with the membrane, we translationally fused either one or two helices (either two copies of the same helix, or a combination of both helices arranged in tandem) to the N-terminus of green fluorescent protein (GFP) and expressed the fusion proteins in *R. sphaeroides* cells. GFP localized to the *R. sphaeroides* cytoplasmic membrane only when it was attached to two copies of either helix or the two different helices arranged in tandem (Figure 3B). Therefore, we propose that *R. sphaeroides* MreB binds to the cytoplasmic membrane using two amphipathic helices that compensate for the weak membrane-binding energy of a single helix (Figure 3C). The weak membrane-binding property of a single helix is likely compensated by MreB polymerization to presents multiple copies of the helix at the inner leaflet of the membrane. To examine the subcellular localization of *R. sphaeroides* MreB, we separated cellular components into cytosolic and membrane fractions and quantified the level of MreB in each fraction by Western blot using a polyclonal antibody against *E. coli* MreB (Figure S7) (20). The expression level of MreB protein was unchanged in *R. sphaeroides* Δ*cls* cells (Figure S8). We found MreB present in the membrane fractions of both *R. sphaeroides* wt and Δ*cls* cells, indicating that the interaction of *R. sphaeroides* MreB with the membrane does not require CL (Figure 3D). The change in cell shape observed in the *R.*

*sphaeroides* Δ*cls* mutant is unlikely to be due to changing the affinity of MreB for the membrane.

MreB filaments direct PG assembly at the sidewalls of cells during cell elongation. We examined whether the structure of MreB is disrupted in *R. sphaeroides* Δ*cls* cells—and consequently its biochemical function—by comparing the PG growth modes of the *R. sphaeroides* wt and Δ*cls* strains. We probed PG assembly in cells at different stages of the cell cycle with HADA: an analog of D-alanine containing a covalently attached coumarin fluorophore that can be incorporated into newly synthesized PG (21). We found that PG assembly in *R. sphaeroides* wt cells occurs along the sidewalls and accompanies cell elongation (Figure 2G). At early and late stages of cell division (i.e., cell septation), PG assembly is refocused away from the sidewalls to the division plane. After the mother and daughter cells are separated, PG assembly shifts back to the sidewalls during cell elongation. This cycle of PG assembly was not observed in *R. sphaeroides* wt cells treated with A22 in which the structure of MreB was disrupted (Figure 2H). A22-treated *R. sphaeroides* cells exhibited three aberrant phenotypes: round and irregular shapes, and asymmetrical cell division. Round *R. sphaeroides* cells displayed peripheral PG assembly and divided at the mid-cell. In irregularly shaped cells, PG was assembled in apparently random loci. Lastly, asymmetrical labeling of septal PG occurred in cells undergoing asymmetrical division. *R. sphaeroides* wt cells treated with MEC had phenotypes similar to those of A22-treated cells, suggesting that inhibiting PBP2 activity would disrupt the structure of MreB (Figure 2H). Despite their round cell shape, the pattern of PG assembly displayed in *R. sphaeroides* Δ*cls* cells is the same as that in wt cells (Figure 2G), suggesting that their shape change is unlikely to be due to disrupting the MreB structure or inhibiting PBP2 activity.

### Inhibition of PG precursor biosynthesis results in a phenotype that resembles *R. sphaeroides* Δ*cls* cells.

In rod-shaped bacteria, PG precursor biosynthesis colocalizes with PG assembly at different stages of the cell cycle (22). The change in cell shape that we observed in the *R. sphaeroides* Δ*cls* mutant could be a result of a reduction in PG precursor biosynthesis that leads to a short supply of PG precursors for cell elongation but does not affect cell division. To test this hypothesis, we treated *R. sphaeroides* cells with the MurA inhibitor fosfomycin (FOS) and the DdlA inhibitor D-cycloserine (DCS) to interfere with PG precursor biosynthesis. MurA converts uridine diphosphate-N-acetylglucosamine (UDP-GlcNAc) into UDP-N-acetylmuramic acid (UDP-MurNAc). DdlA is a D-alanine (D-Ala) ligase that generates D-Ala-D-Ala (Figure 1). The MIC of FOS is 1500 μg/mL and the MIC of DCS is 1 μg/mL for *R. sphaeroides*. At sub-MIC concentrations (FOS: 250 μg/mL; DCS: 0.05 μg/mL), both drugs decreased *R. sphaeroides* cell length (FOS: 15%; DCS: 25%) and did not cause significant growth defects (Figure 2E, F). HADA labeling experiments showed that these two drugs did not affect the pattern of PG assembly in *R. sphaeroides* cells (Figure 2G). These results suggest that the change in the shape of *R. sphaeroides* Δ*cls* cells may arise due to a decrease in PG precursor biosynthesis caused by a CL deficiency.

To further test this hypothesis, we determined the PG composition of *R. sphaeroides* cells using ultra performance liquid chromatography-mass spectrometry (UPLC-MS) (Figure S9, Table S4). We treated *R. sphaeroides* wt cells with A22 and MEC and found that both compounds changed the PG composition of cells (Figure 4A). Compared to wt cells, A22 and MEC decreased the concentration of disaccharide-peptide (muropeptide) monomer by 33% and increased the concentration of crossed-linked muropeptides (dimer and trimer) by 20%, resulting in a 32% increase in the degree of cross-linking (Figure 4B). Both A22 and MEC led to a 60% increase in the concentration of anhydromuramyl muropeptides found at the terminating end of the glycan strand, reflecting a 43% decrease in the average glycan strand length (Figure 4C). A similar result was found in *E. coli* (23). Surprisingly, *R. sphaeroides* Δ*cls* cells have a PG composition that is indistinguishable from those of wt cells and wt cells treated with either FOS or DCS (Figure 4A, B, C). These results confirm that a CL deficiency does not impair the function of elongasome and that the change in cell shape of the *R. sphaeroides* Δ*cls* mutant is due to abnormalities in PG precursor biosynthesis.

### CL regulates PG precursor biosynthesis.

To investigate the role CL plays in the production of PG precursors (lipid II) in cells, we first compared expression levels of the genes coding for enzymes that relay to synthesize lipid II in *R. sphaeroides* wt and Δ*cls* cells. We found no significant difference (Figure S10). MurG is a GTase that catalyzes the rate-limiting step of lipid II formation by transferring the GlcNAc from UDP-GlcNAc to lipid I (Figure 1) (24). It has been suggested that MurG is a peripheral membrane protein (25). We fused *gfp* with *R. sphaeroides* genomic *murG* in both wt and Δ*cls* strains and imaged the cells (Figure S11). We observed that MurG localized at the membrane and concentrated at the poles of the cell (Figure 5A). At the division plane, MurG focused and colocalized with FtsZ (Figure 5A, S12). This subcellular localization pattern of MurG was not changed in *R. sphaeroides* Δ*cls* cells. We performed cell fractionation experiments and found no significant difference between the amounts of membrane-localized MurG (~75%) in *R. sphaeroides* wt and Δ*cls* cells (Figure 5B). These results suggest that the membrane localization of MurG does not require CL and the change in the shape of *R. sphaeroides* Δ*cls* cells is not due to mislocalization of MurG.

Anionic phospholipids, such as CL and PGL, have been shown to accumulate at the polar regions of rod-shaped bacterial cells (8). We stained *R. sphaeroides* membranes with the anionic phospholipids-specific fluorescent dye 10-N-nonyl acridine orange (NAO) and observed an enrichment of the dye at the polar regions of both wt and Δ*cls* cells (Figure 5C). CL synthase catalyzes the formation of CL using PGL as a precursor. Compared to *R. sphaeroides* wt cells, Δ*cls* cells contain a higher level of PGL that maintains the anionicity of the membrane (10). The polar enrichment of MurG that we observed in *R. sphaeroides* wt and Δ*cls* cells suggests a higher affinity of MurG for CL and PGL. We purified recombinant MurG and quantified the interaction between MurG and phospholipid membranes using an *in* *vitro* liposome-pelleting assay. We found that 67% of MurG interacted with liposomes containing 100 mol% PC and segregated to the pellet fraction. When 10 mol% CL or PGL was incorporated into the liposomes, the fraction of MurG interacting with membranes increased to 92% (Figure 5D). These results suggest that MurG directly interacts with membrane structure and has an equal preference for CL and PGL.

CL and PGL are both important for the function of *E. coli* MurG; however, CL is more effective in promoting its GTase activity (26). Although the MurG-membrane interaction is not affected in *R. sphaeroides* Δ*cls* cells, the depletion of CL in the cell membrane would cause a decrease in MurG activity that reduces lipid II biosynthesis for cell elongation. To test this hypothesis, we treated *R. sphaeroides* cells with the MurG inhibitor murgocil (27). However, murgocil is *Staphylococcal*-specific and did not have bioactivity against *R. sphaeroides* due to amino acid differences in the MurG-murgocil binding site between the two strains (Figure S13). Alternatively, we compared the amounts of lipid II generated in *R. sphaeroides* wt and Δ*cls* cells by quantifying the incorporation of HADA into the cell wall (Figure 5E). We found that a CL deficiency caused a 25% decrease in the production of lipid II in *R. sphaeroides*. Complementation of CL synthase in *R. sphaeroides* Δ*cls* cells restored lipid II production by 14% (Figure 5F), suggesting that CL is important for the enzymatic activity of MurG and cell elongation. As control experiments, we treated *R. sphaeroides* cells with FOS and DCS. We found that both PG precursor inhibitors reduced HADA incorporation by 21% and 24%, respectively (Figure S14A). We also treated *S. aureus* cells with murgocil and the drug decreased HADA incorporation by 81% (Figure S14B). These results demonstrate that inhibition of PG precursor biosynthesis can impair PG assembly.

### Overexpression of MurG in *R. sphaeroides* Δ*cls* cells restores the rod shape of cells.

To further confirm the correlation between MurG activity and cell length, we increased MurG activity in *R. sphaeroides* cells by overexpressing the enzyme (an N-terminal GFP fusion protein) from the pIND vector in cells. Induction of the plasmid with 100 μM IPTG caused cell filamentation and uneven cell division due to polymerization of the protein and possibly a disturbance of FtsZ function (Figure S15). However, leaky expression of the plasmid did not affect the subcellular localization of MurG and cell growth, and consequently we used leaky expression for our overexpression experiments. We found that the overexpression of MurG in *R. sphaeroides* cells caused an increase (11%) in cell length compared to cells expressing GFP (Figure 6A, B).

A hydrophobic patch of *E. coli* MurG has been proposed to be the membrane association motif (28). Sequence alignment revealed that this membrane-binding interface is conserved in *R. sphaeroides* MurG (Figure S13). We created the *R. sphaeroides* MurG mutant L76E, in which the residue L76 is corresponding to the residue L78 in the hydrophobic patch of *E. coli* MurG, and expressed it in *R. sphaeroides* cells. We found that this MurG mutant was able to localize at the division plane and did not affect the cell growth. However, it failed to reach the *R. sphaeroides* cytoplasmic membrane and only caused a minor increase (5%) in cell length compared to cells expressing GFP (Figure 6C). These results correlate MurG activity to the length of *R. sphaeroides* cells. To compensate for the decreased MurG activity in cells due to a CL deficiency, we overexpressed MurG in *R. sphaeroides* Δ*cls* cells. We found that the overexpression of MurG increased the length of *R. sphaeroides* Δ*cls* cells by 13% compared to Δ*cls* cells expressing GFP (Figure 6D, E), suggesting that the morphological abnormality of the *R. sphaeroides* Δ*cls* mutant is a result of a decrease in MurG activity that reduces the supply of lipid II for cell elongation.

### CL deficiency increases the sensitivity of *R. sphaeroides* to antibiotics targeting PG synthesis.

Given that CL plays an important role in MurG function, the *R. sphaeroides* Δ*cls* mutant should be susceptible to antibiotics that inhibit PG precursor biosynthesis and its downstream PG assembly. To test this hypothesis, we performed spot-titre assays and found that compared to *R. sphaeroides* wt cells, Δ*cls* cells were more sensitive to drugs interfering with PG precursor biosynthesis, including: FOS and DCS, and drugs interrupting PG assembly, including: A22, MEC, and ampicillin (AMP; binds PBPs and inhibits their TPase activities) (Figure 7). These results confirm that CL deficiency impedes the production of PG precursors in *R. sphaeroides*.

# DISCUSSION

In this study, we used a chemical biology approach and provided evidence that CL can be a bacterial cell shape determinant. We treated *R. sphaeroides* wt cells with different antibiotics targeting PG synthesis and compared the resulting phenotypes with the shape of *R. sphaeroides* Δ*cls* cells. We found that inhibition of the elongasome changed the shape, PG growth mode, and PG composition of *R. sphaeroides* cells. Although the depletion of CL in *R. sphaeroides* alters its cell shape, the PG growth mode and PG composition of *R. sphaeroides* Δ*cls* cells remain unchanged. Surprisingly, inhibitors of PG precursor synthases caused phenotypes of *R. sphaeroides* cells similar to Δ*cls* cells, which was not observed in other model bacteria, such as *E. coli* and *Caulobacter crescentus* (29). These results led us to hypothesize that CL would regulate the activities of enzymes synthesizing PG precursor for cell elongation in *R. sphaeroides*. Of the ten PG precursor synthases shown in Figure 1, MurG catalyzes the rate-limiting step of PG precursor biosynthesis and is reported to preferentially interact with CL in *E. coli* (26, 30). We demonstrate that the change in the shape of *R. sphaeroides* Δ*cls* cells is a result of a decrease in MurG activity. However, we do not rule out the possibility that a CL deficiency can also decrease the activities of other PG precursor synthases in *R. sphaeroides*, especially the two integral membrane proteins MraY and MurJ.

CL has four acyl tails and a relatively small head group, creating an intrinsic molecular shape with a large curvature of ~1.3 $nm^{-1}$ (31). In rod-shaped bacteria, CL tends to localize in the inner leaflet of the cell membrane and clusters into membrane microdomains that concentrate at the cell poles to reduce the elastic stress arising from the enhanced curvature of the membrane at these cellular regions relative to the cylindrical body (32, 33). In contrast, PGL has a significantly smaller curvature (~0.11 $nm^{-1}$) than CL but still concentrates at the polar membranes through unknown mechanisms (8). The heterogeneous distribution of anionic phospholipids in membranes has been hypothesized to sort proteins into different regions in bacterial cells (34). We found that MurG interacts with anionic phospholipids and is enriched at the poles of *R. sphaeroides* cells where PG synthesis does not occur. We suggest that the polar localization of MurG provides a mechanism for the storage of excess protein (35).

It has been shown that in energy-transducing membranes, CL interacts tightly with respiratory complexes in the electron transport chain and regulates ATP synthesis. CL also binds tightly to the SecYEG protein complex and regulates protein translocation (36-39). CL domains can be induced by the preferential interaction of CL with specific proteins and localized throughout the cell body (40). We hypothesize that the interaction of MurG with CL induces the formation of CL membrane microdomains that provide favored environments for MurG and stimulates its GTase activity (Figure 5E). Although MurG also binds PGL and its subcellular localization in *R. sphaeroides* Δ*cls* cells is unchanged, PGL is unable to form domains and restore MurG activity. In support of this hypothesis, *R. sphaeroides* Δ*cls* cells have a decreased lipid II production compared to *R. sphaeroides* wt cells.

The structural mechanisms differentiating the effects of the two anionic phospholipids on MurG activity require further research. *E. coli* mutants devoid of CL do not have an altered morphology because the MurG activity is restored in cells due to an upregulation of MurG expression (26). However, the level of MurG protein in *R. sphaeroides* Δ*cls* cells remains unchanged (Figure S16). We overexpressed MurG in *R. sphaeroides* Δ*cls* cells to restore its activity in cells and found a recovery of rod-shaped morphology.

The hydrophobic patch of *E. coli* MurG is surrounded by several basic residues that might contribute to its preferential interaction with CL (28). These residues are not conserved in *R. sphaeroides* MurG, except for R77, which is corresponding to R79 in *E. coli* MurG (Figure S13). We created the *R. sphaeroides* MurG mutant R77E and expressed it in *R. sphaeroides* cells. We did not observe a difference in subcellular localization between this mutant and the wild-type MurG (data not shown). The molecular mechanisms underlying the preferential interaction between MurG and anionic phospholipids remain to be determined. Interestingly, the MurG membrane-binding mutant L76E is still able to localize at the division plane, suggesting that MurG interacts with the divisome using a different motif. This would explain why a CL deficiency does not cause a defect in cell division in *R. sphaeroides.*

A growing body of evidence indicates that CL plays a fundamental role in bacterial adaptation to environmental stress, including osmoadaptation, biofilm formation, DNA repair, and survival in host tissues (7, 41-46). Our research provides the first example of how membrane composition plays a role in determining bacterial cell shape. The PG cell wall is the canonical target for antibiotics that are bacterial chemotherapeutics; however, the emergence of antibiotic resistance has dampened the utility of this class of antibiotics. Although the *R. sphaeroides* Δ*cls* mutant has no significant defect in growth, it is susceptible to antibiotics that target PG compared to the *R. sphaeroides* wt strain. It has been shown that a *Pseudomonas putida* Δ*cls* mutant is susceptible to several antibiotics as its drug efflux system is impaired (47). These data suggest CL biosynthesis as a potential antibiotic target.

# EXPERIMENTAL PROCEDURES

## Bacterial strains and growth conditions

*R. sphaeroides* strains were grown aerobically in Sistrom's succinate medium at 30°C with shaking at 200 rpm. When required, kanamycin (25 μg/ml), spectinomycin (5 μg/ml), or tetracycline (0.025 μg/ml) was added to the medium. *E. coli* strains were grown in LB broth at 37°C with shaking at 200 rpm. When required, kanamycin (25 μg/ml), or tetracycline (10 μg/ml) was added to the medium. The bacterial strains and plasmids used in this study are described in Table S1.

## Analysis of cell morphology

An aliquot of cell cultures in log phase (absorbance of 0.6, $\lambda$ = 600 nm) was dropped onto a 2% (w/v) agarose pad prepared in phosphate-buffered saline (PBS) buffer (137 mM NaCl, 2.7 mM KCl, 10 mM $Na_2HPO_4$, 1.76 mM$KH_2PO_4$, pH 7.4), covered with a glass coverslip, and imaged with an inverted Nikon Eclipse Ti microscope equipped with a Photometrics CoolSNAP HQ2 charge-coupled-device (CCD) camera and a 120 W mercury arc lamp (X-cite Series 120, EXFO). Images were acquired with a 100× objective (Nikon Plan Apo 100×/1.40 oil Ph3 DM) and the Nikon Instruments Software (NIS)-Elements Advanced Research (AR) microscope imaging software program (Version 4.000.07). Cell width and length were determined with ImageJ. To track the cell growth at single-cell level, cells were dropped onto a 2% (w/v) agarose pad prepared in Sistrom's succinate medium and imaged every 5 min for 6 h at 30°C.

### Plasmid constructions

The primers used in this study are listed in Table S2. Cloning of PCR fragments into vectors were performed by In-Fusion Cloning (Clontech) in accordance with the user manual unless otherwise noted. The pIND5 and pK18*mobsac*B constructs were transformed into *E. coli* S17-1 and subsequently mobilized via conjugation into the recipient *R. sphaeroides* wt or Δ*cls* strain as described previously (48).

### HADA labeling and quantification

Cells were grown to early log phase (absorbance of 0.3, $\lambda = 600$ nm) and labeled with 0.5 mM HADA for ~1/8 of the doubling time (20 min) at room temperature, followed by washing three times with PBS to remove excess dye. The labeled cells were imaged using a DAPI filter. The fluorescence of HADA incorporated into PG was measured with an excitation wavelength of 405 nm and an emission wavelength of 450 nm using a Tecan infinite M1000 microplate reader (Tecan, San Jose, CA). Additional and more detailed methods are provided in Supporting Information.

## ACKNOWLEDGEMENTS

We thank the Ferguson-Miller laboratory (Michigan State University) for the strain *R. sphaeroides* Δ*cls*, the Donohue laboratory (University of Wisconsin-Madison) for the plasmid pIND, and NBRP (NIG, Japan) : *E.coli* for the MreB antibody. We thank Cameron Scarlett for UPLC-MS support. The research was supported by a William R. & Dorothy E. Sullivan Wisconsin Distinguished Graduate Fellowship and a Dr. James Chieh-Hsia Mao Wisconsin Distinguished Graduate Fellowship.

**Figure 1. PG synthesis in gram-negative bacteria.** PG synthesis in Gram-negative bacteria is conserved and proceeds in three distinct steps. The process starts with the biosynthesis of PG precursor (i.e., lipid II) in the cytoplasm, followed by its translocation from the cytoplasm to the periplasm where PG assembly occurs. In rod-shaped bacteria, cytoskeletal proteins guide the location of PG synthesis at different stages of the cell cycle. During cell division, FtsZ organizes the divisome, which synthesizes PG at the division site. For clarity, a sub-set of cell-division proteins is illustrated in the diagram. During cell elongation, the elongasome is associated with MreB, which directs PG synthesis at the sidewalls. See text for details. GlcNAc, N-acetylglucosamine; MurNAc, N-acetylmuramic acid; meso-Dap, meso-diaminopimelic acid.

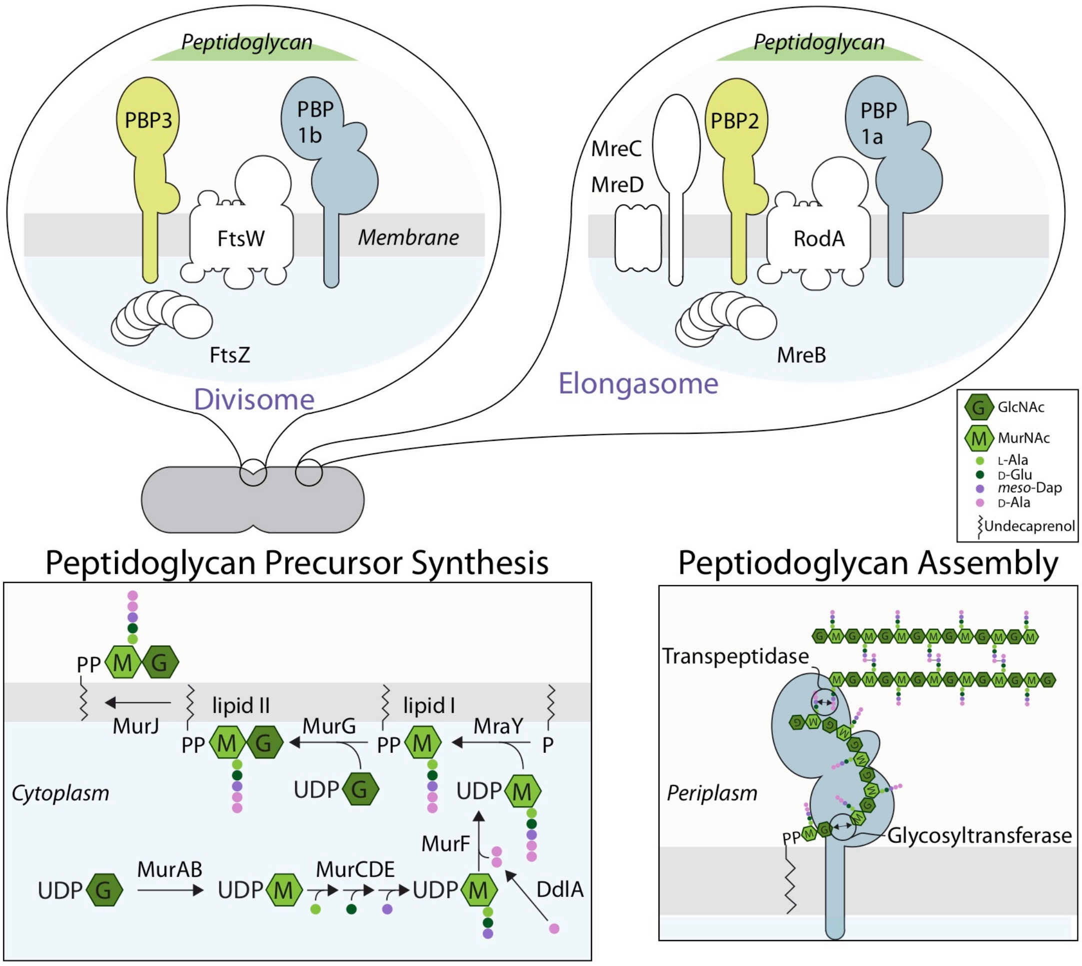
Peptidoglycan
PBP3
PBP 1b
FtsW
Membrane
FtsZ
Divisome
Peptidoglycan
MreC
MreD
PBP2
PBP 1a
RodA
MreB
Elongasome
G GlcNAc
M MurNAc
L-Ala
D-Glu
meso-Dap
D-Ala
Undecaprenol
Peptidoglycan Precursor Synthesis
PP M G
MurJ
lipid II
PP M G
MurG
UDP G
lipid I
PP M
MraY
P
UDP M
Cytoplasm
MurF
UDP G
MurAB
UDP M
MurCDE
UDP M
DdlA
Peptiodoglycan Assembly
Transpeptidase
Periplasm
PP
Glycosyltransferase

Figure 1

**Figure 2. CL participates in cell shape determination through regulating PG precursor biosynthesis.** Probability density histogram of the cell length distribution of *R. sphaeroides* wt cells (A), Δ*cls* cells (B), wt cells treated with A22 (C), wt cells treated with MEC (D), wt cells treated with FOS (E), and wt cells treated with DCS (F). Cells were grown in plain medium or medium containing the indicated small molecule inhibitors until they reached log phase (absorbance of 0.6, λ = 600 nm) and imaged by phase-contrast bright-field microscopy. Scale bar, 2 μm. Each data point represents a mean value ± standard deviation of the cell length (L), width (W), and aspect ratio (AR) for 300 cells determined by ImageJ. The shaded blue area overlaying the histogram represents the Kernel density estimation (KDE) of the cell length distribution. We overlaid a grey dashed line outlining the KDE of the cell length distribution of *R. sphaeroides* wt cells with the other five histograms for comparison. (G) Representative micrographs of HADA-labeled *R. sphaeroides* wt cells, Δ*cls* cells, wt cells treated with FOS, and wt cells treated with DCS. (H) Representative micrographs of HADA-labeled *R. sphaeroides* wt cells treated with A22, and wt cells treated with MEC. Cells were grown in plain medium or medium containing the indicated small molecule inhibitors to early log phase (absorbance of 0.3, λ = 600 nm), labeled with HADA, and imaged using phase and fluorescence microscopy. The concentrations of inhibitors used were A22: 10 μg/ml; MEC: 0.5 μg/ml; FOS: 250 μg/ml; DCS: 0.05 μg/ml.

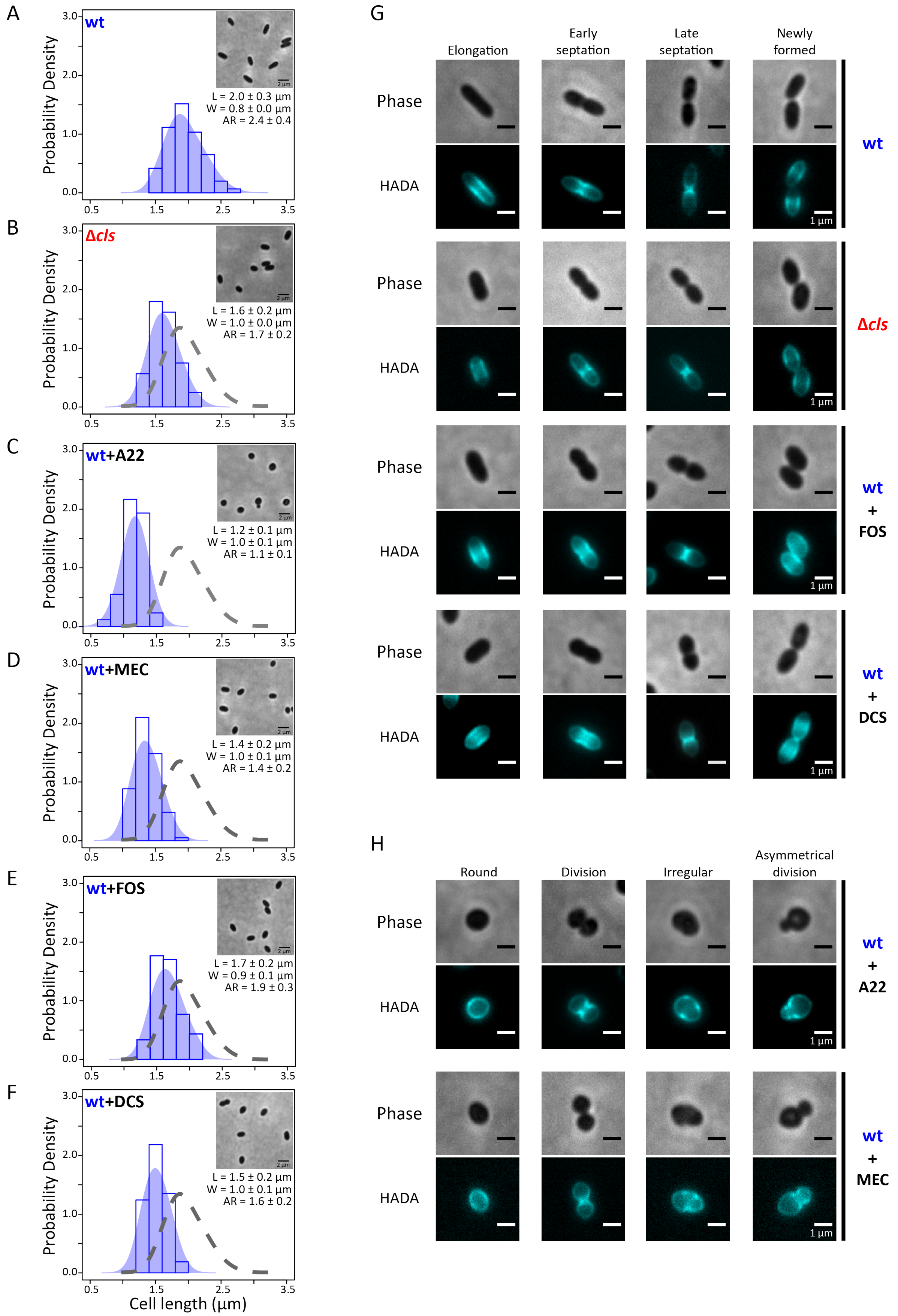
A
wt
L = 2.0 ± 0.3 µm
W = 0.8 ± 0.0 µm
AR = 2.4 ± 0.4
B
Δcls
L = 1.6 ± 0.2 µm
W = 1.0 ± 0.0 µm
AR = 1.7 ± 0.2
C
wt+A22
L = 1.2 ± 0.1 µm
W = 1.0 ± 0.1 µm
AR = 1.1 ± 0.1
D
wt+MEC
L = 1.4 ± 0.2 µm
W = 1.0 ± 0.1 µm
AR = 1.4 ± 0.2
E
wt+FOS
L = 1.7 ± 0.2 µm
W = 0.9 ± 0.1 µm
AR = 1.9 ± 0.3
F
wt+DCS
L = 1.5 ± 0.2 µm
W = 1.0 ± 0.1 µm
AR = 1.6 ± 0.2
Probability Density
0.0
1.0
2.0
3.0
0.5
1.5
2.5
3.5
Cell length (µm)
2 µm
G
Elongation
Early septation
Late septation
Newly formed
Phase
HADA
1 µm
wt
Δcls
wt + FOS
wt + DCS
H
Round
Division
Irregular
Asymmetrical division
wt + A22
wt + MEC

Figure 2

**Figure 3.** ***R. sphaeroides*** **MreB is a membrane protein and has no preference for CL in binding to the cytoplasmic membrane.** (A) Helical wheel projections of the two predicted amphipathic helices in *R. sphaeroides* MreB. In both helices, hydrophobic residues cluster on one side, forming a predicted membrane-binding surface. Basic residues cluster on the other side of helix 2. Green diamonds denote hydrophobic residues. The amount of green is in proportion to the hydrophobicity. Light blue pentagons represent basic residues. The circles indicate polar and neutral amino acids. (B) Representative micrographs of *R. sphaeroides* cells expressing cytoplasmic GFP, GFP translationally fused to the C-terminus of either MreB helix 1 (H1-GFP) or MreB helix 2 (H2-GFP), the C-terminal end of a construct containing both H1 and H2 (H1-H2-GFP), the C-terminus of a tandem repeat of H1 (H1-H1-GFP), or the C-terminus of a tandem repeat of H2 (H2-H2-GFP) from the pIND vector with 1 mM IPTG induction. Cells were grown to log phase (absorbance of 0.6, λ = 600 nm) and imaged using fluorescence microscopy. (C) A diagram depicting that *R. sphaeroides* MreB binds to the membrane using two amphipathic helices. (D) Biochemical fractionation of *R. sphaeroides* wt and Δ*cls* cells. We fractionated wt and Δ*cls* cell lysates that had the same amounts of proteins into cytosolic and membrane fractions, and performed Western blot analysis using a polyclonal antibody against *E. coli* MreB.

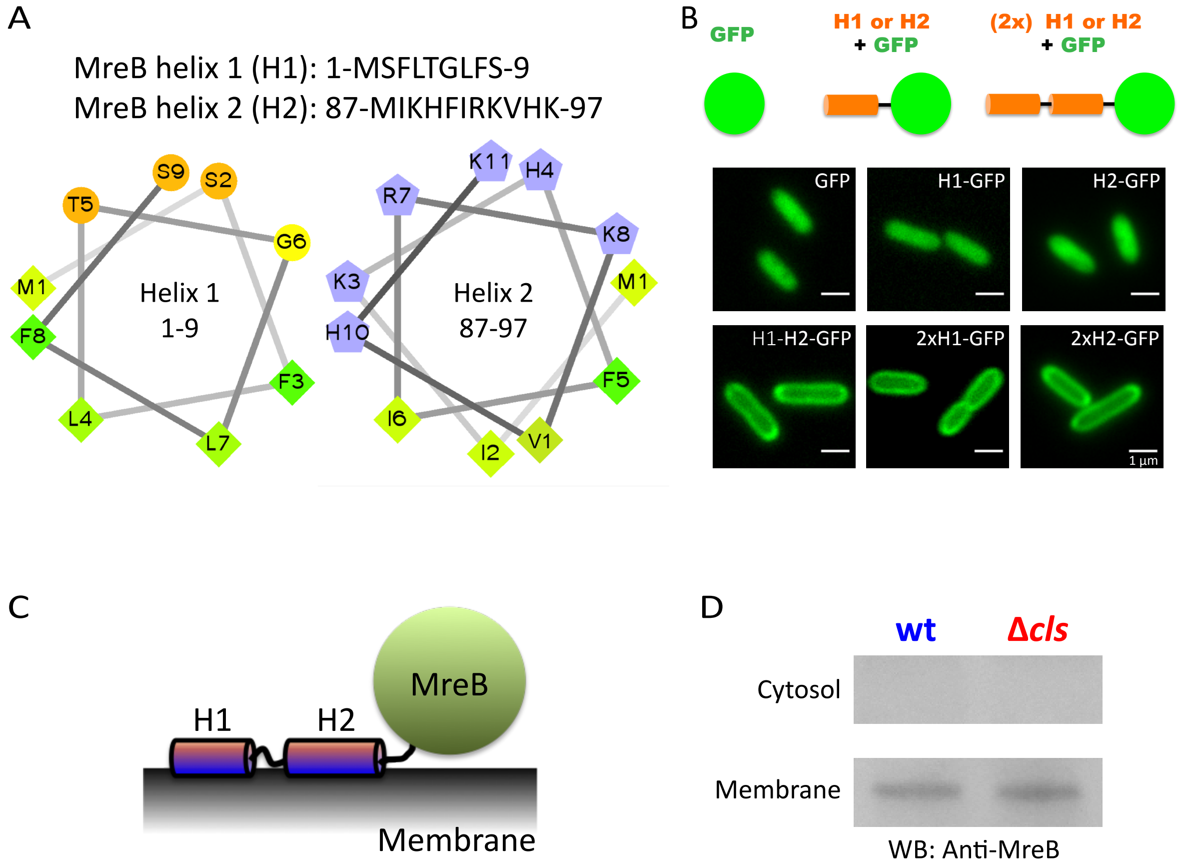
A
MreB helix 1 (H1): 1-MSFLTGLFS-9
MreB helix 2 (H2): 87-MIKHFIRKVHK-97
S9
S2
T5
G6
M1
F8
F3
L4
L7
Helix 1
1-9
K11
H4
R7
K8
K3
M1
H10
F5
I6
I2
V1
Helix 2
87-97
B
GFP
H1 or H2
+ GFP
(2x) H1 or H2
+ GFP
GFP
H1-GFP
H2-GFP
H1-H2-GFP
2xH1-GFP
2xH2-GFP
1 μm
C
H1
H2
MreB
Membrane
D
wt
Δcls
Cytosol
Membrane
WB: Anti-MreB

Figure 3

**Figure 4. CL deficiency does not affect the PG composition of cells.** (A) Quantification of muropeptides purified from *R. sphaeroides* wt cells, Δ*cls* cells, wt cells treated with A22, wt cells treated with MEC, wt cells treated with FOS, and wt cells treated with DCS. A22 and MEC treatment decreased the relative abundance of muropeptide monomer by 33%, increased the relative abundance of crossed-linked muropeptides (dimer and trimer) by 20%, and increased the relative abundance of anhydrous muropeptides by 60%; all compared to wt cells. These alterations in muropeptide composition yield a PG with a higher level of cross-linking (B) and a shorter average strand length (C) compared to wt cells. A CL deficiency does not change the PG composition of *R. sphaeroides* Δ*cls* cells that resembles those of wt cells and wt cells treated with either FOS or DCS. Data represent mean values ± standard deviations obtained from three independent experiments. The concentrations of inhibitors used were: A22: 10 μg/ml; MEC: 0.5 μg/ml; FOS: 250 μg/ml; DCS: 0.05 μg/ml.

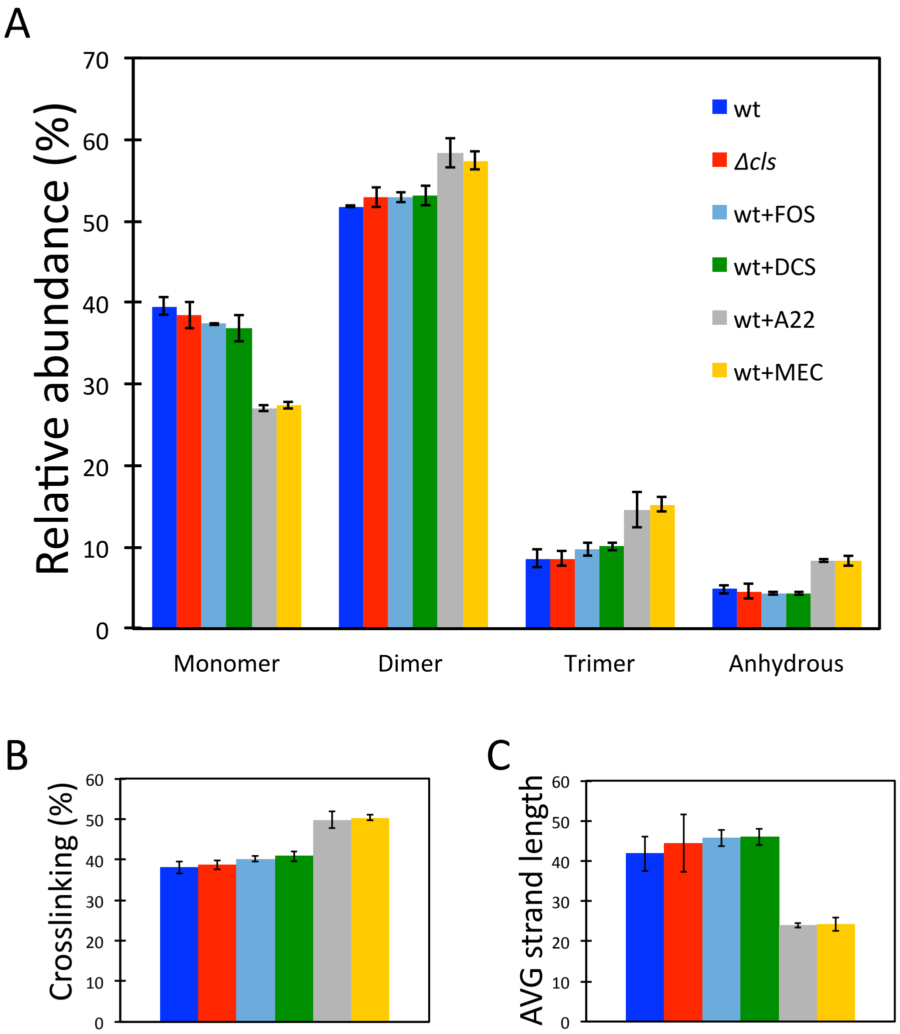
A
70
60
50
40
30
20
10
0
Relative abundance (%)
wt
*Δcls*
wt+FOS
wt+DCS
wt+A22
wt+MEC
Monomer
Dimer
Trimer
Anhydrous
B
Crosslinking (%)
60
50
40
30
20
10
0
C
AVG strand length
60
50
40
30
20
10
0

**Figure 4**

**Figure 5.** ***R. sphaeroides*** **MurG interacts with CL, and this interaction is important for its enzymatic activity and cell elongation.** (A) Representative micrographs of TyL1 and TyL2 cells, which are *R. sphaeroides* wt and Δ*cls* cells in which the genomic *murG* is replaced with *gfp-murG*, respectively. Cells were grown to log phase (absorbance of 0.6, $\lambda$ = 600 nm) and imaged using phase and fluorescence microscopy. (B) Biochemical fractionation of TyL1 and TyL2 cells. We fractionated TyL1 and TyL2 cell lysates that had the same amounts of proteins into cytosolic and membrane fractions, and performed Western blot analysis using a monoclonal antibody against GFP. The percentage of membrane-localized MurG was determined by quantifying the optical densitometry signal with ImageJ. Data represent mean values ± standard deviations obtained from three independent experiments. (C) Representative micrographs of *R. sphaeroides* wt and Δ*cls* cells stained with NAO. Cells were grown to early log phase (absorbance of 0.3, $\lambda$ = 600 nm), stained with NAO, and imaged using fluorescence microscopy. (D) Liposome-pelleting assays of MurG with liposomes containing the indicated phospholipids. The percentage of pelleted MurG was determined by quantifying the optical densitometry signal with ImageJ. Data represent mean values ± standard deviations obtained from three independent experiments. S, supernatant; P, pellet. (E) A diagram depicting the incorporation of HADA into the lipid II molecule by MurG and its assembly into the existing PG by PBP proteins. We hypothesize that CL interacts with MurG and is important for its activity. As CL does not affect PG assembly, we assess the effect of CL on lipid II production by quantifying the incorporation of HADA into the

existing PG. (F) Quantification of HADA incorporation in *R. sphaeroides* wt, Δ*cls* cells, and Δ*cls* cells expressing Cls. Cells were grown until early log phase (absorbance of 0.3, $\lambda$ = 600 nm) and labeled with HADA. We measured the fluorescence emission of HADA and normalized the fluorescent signals by CFU. Each data point (mean value ± standard deviation) was obtained from three independent experiments.

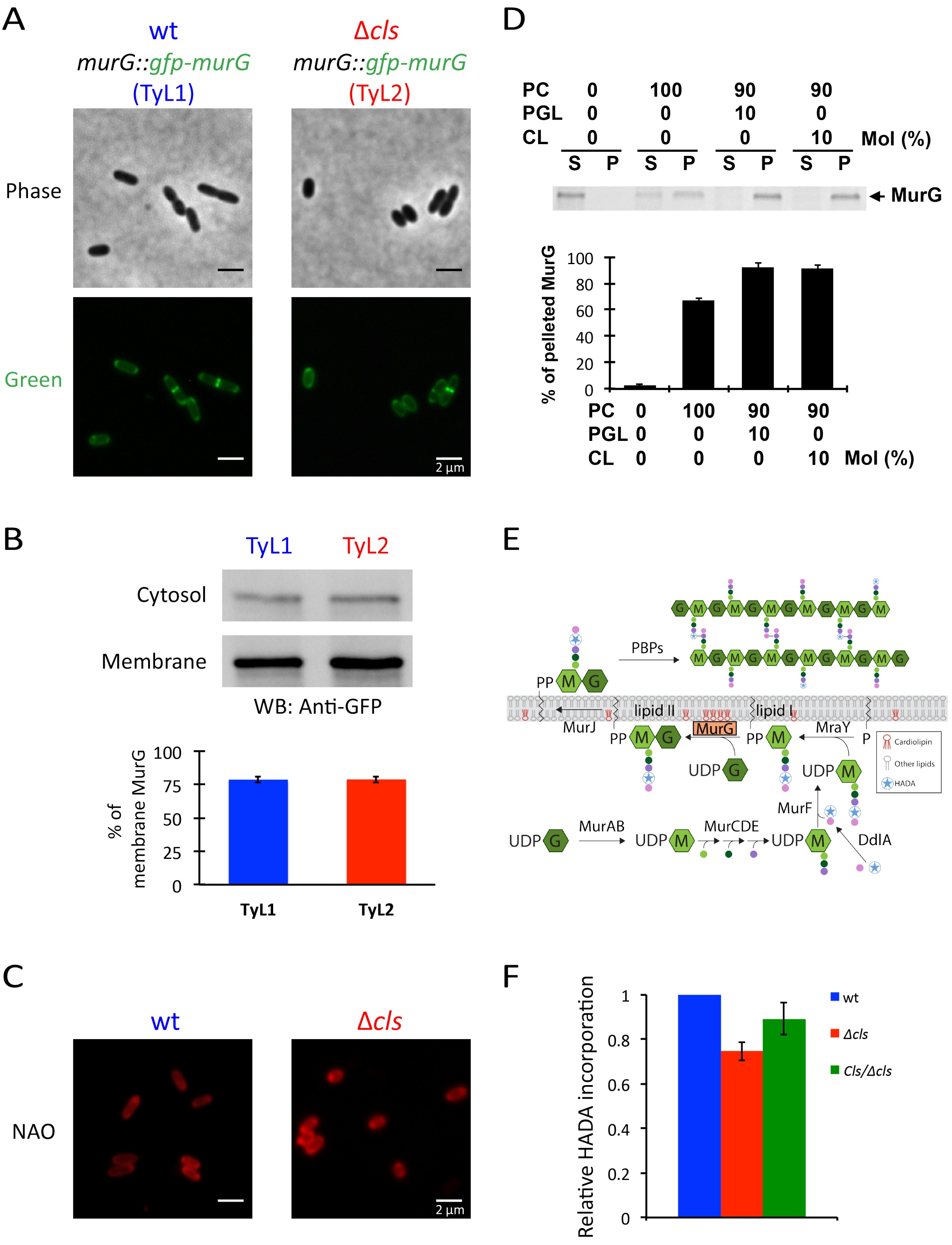
A
wt
murG::gfp-murG
(TyL1)
Δcls
murG::gfp-murG
(TyL2)
Phase
Green
2 µm
D
PC 0 100 90 90
PGL 0 0 10 0
CL 0 0 0 10 Mol (%)
S P S P S P S P
MurG
% of pelleted MurG
100
80
60
40
20
0
PC 0 100 90 90
PGL 0 0 10 0
CL 0 0 0 10 Mol (%)
B
TyL1
TyL2
Cytosol
Membrane
WB: Anti-GFP
% of membrane MurG
100
75
50
25
0
TyL1
TyL2
E
PBPs
PP M G
lipid II
lipid I
MurJ
MurG
MraY
P
PP M G
PP M
UDP G
UDP M
Cardiolipin
Other lipids
HADA
MurF
UDP G
MurAB
UDP M
MurCDE
UDP M
DdlA
C
wt
Δcls
NAO
2 µm
F
Relative HADA incorporation
1
0.8
0.6
0.4
0.2
0
wt
Δcls
Cls/Δcls

**Figure 5**

**Figure 6. MurG activity correlates with the length of *R. sphaeroides* cells.** Representative micrographs of *R. sphaeroides* wt cells expressing GFP (A), wt cells expressing GFP-MurG (B), wt cells expressing GFP-MurG$^{L76E}$ (C), Δ*cls* cells expressing GFP (D), and Δ*cls* cells expressing GFP-MurG (E) from the pIND vector without IPTG induction. Cells were grown to log phase (absorbance of 0.6, $\lambda = 600$ nm) and imaged using phase and fluorescence microscopy. Probability density histogram of the cell length distribution of each strain is shown on the right panel. Each data point represents a mean value ± standard deviation of the cell length (L), width (W), and aspect ratio (AR) for 300 cells determined by ImageJ. The shaded blue area overlaying the histogram represents the Kernel density estimation (KDE) of the cell length distribution. We overlaid a grey dashed line outlining the KDE of the cell length distribution of *R. sphaeroides* wt cells expressing GFP with the histograms of wt cells expressing GFP-MurG and wt cells expressing GFP-MurG$^{L76E}$ for comparison. We also overlaid a grey dashed line outlining the KDE of the cell length distribution of *R. sphaeroides* Δ*cls* cells expressing GFP with the histogram of Δ*cls* cells expressing GFP-MurG for comparison.

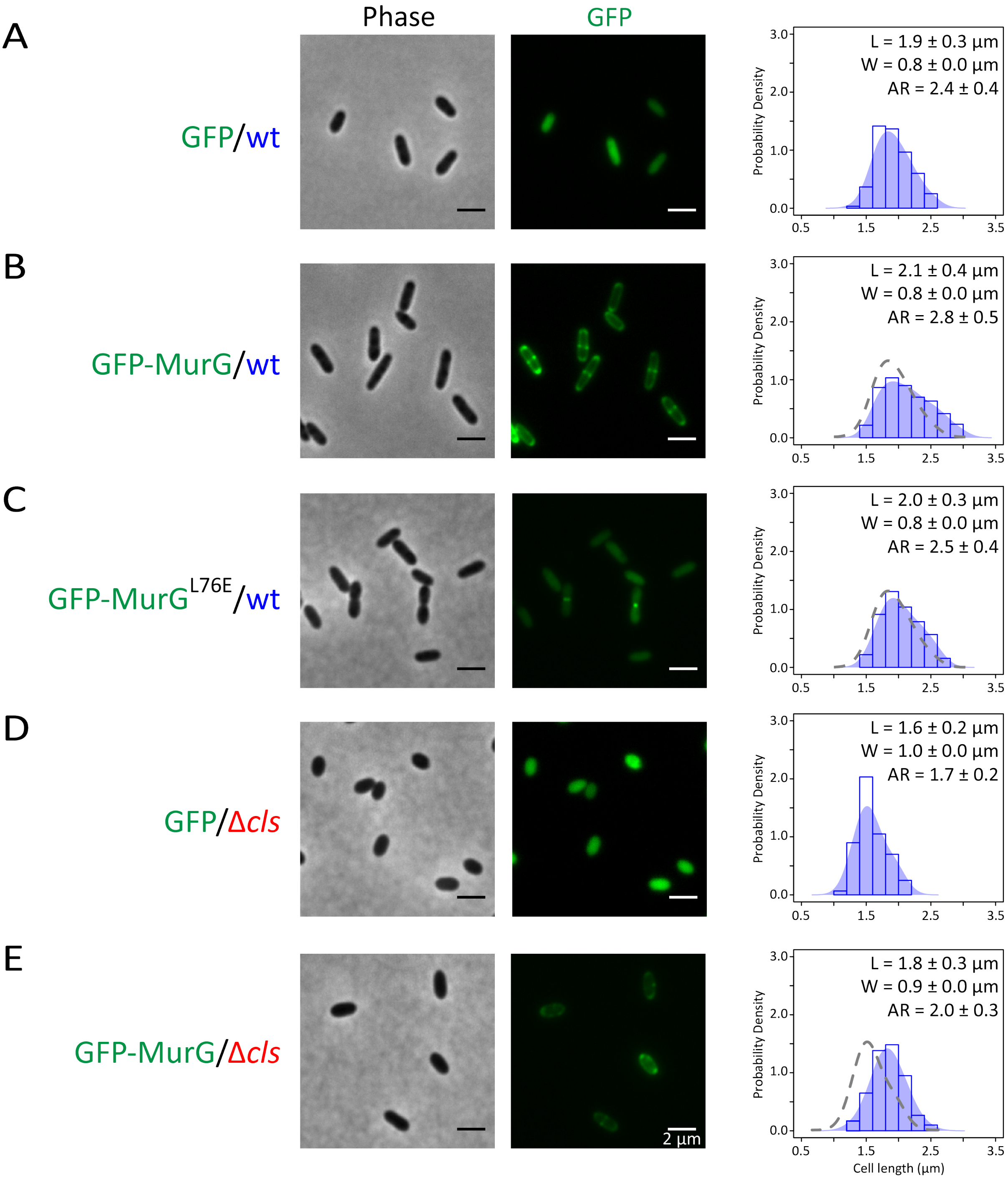
Phase
GFP
A
GFP/wt
L = 1.9 ± 0.3 µm
W = 0.8 ± 0.0 µm
AR = 2.4 ± 0.4
B
GFP-MurG/wt
L = 2.1 ± 0.4 µm
W = 0.8 ± 0.0 µm
AR = 2.8 ± 0.5
C
GFP-MurG$^{L76E}$/wt
L = 2.0 ± 0.3 µm
W = 0.8 ± 0.0 µm
AR = 2.5 ± 0.4
D
GFP/Δcls
L = 1.6 ± 0.2 µm
W = 1.0 ± 0.0 µm
AR = 1.7 ± 0.2
E
GFP-MurG/Δcls
L = 1.8 ± 0.3 µm
W = 0.9 ± 0.0 µm
AR = 2.0 ± 0.3
2 µm
Probability Density
0.0
1.0
2.0
3.0
0.5
1.5
2.5
3.5
Cell length (µm)

**Figure 6**

**Figure 7.** ***R. sphaeroides* Δ*cls* mutant is susceptible to antibiotics targeting PG synthesis.** Spot-titre assays of *R. sphaeroides* wt and Δ*cls* cells. Cell cultures in stationary phase were standardized to an absorbance of 1.0 ($\lambda$ = 600 nm). The standardized cultures were serially diluted and 5 μl aliquots were spotted on the surfaces of plates containing Sistrom's minimal medium with 1.5% agar and the indicated antibiotics (FOS: 125 μg/ml; DCS: 0.05 μg/ml; A22: 5 μg/ml; MEC: 0.1 μg/ml; AMP: 5 μg/ml). The plates were incubated for 72 h at 30°C.

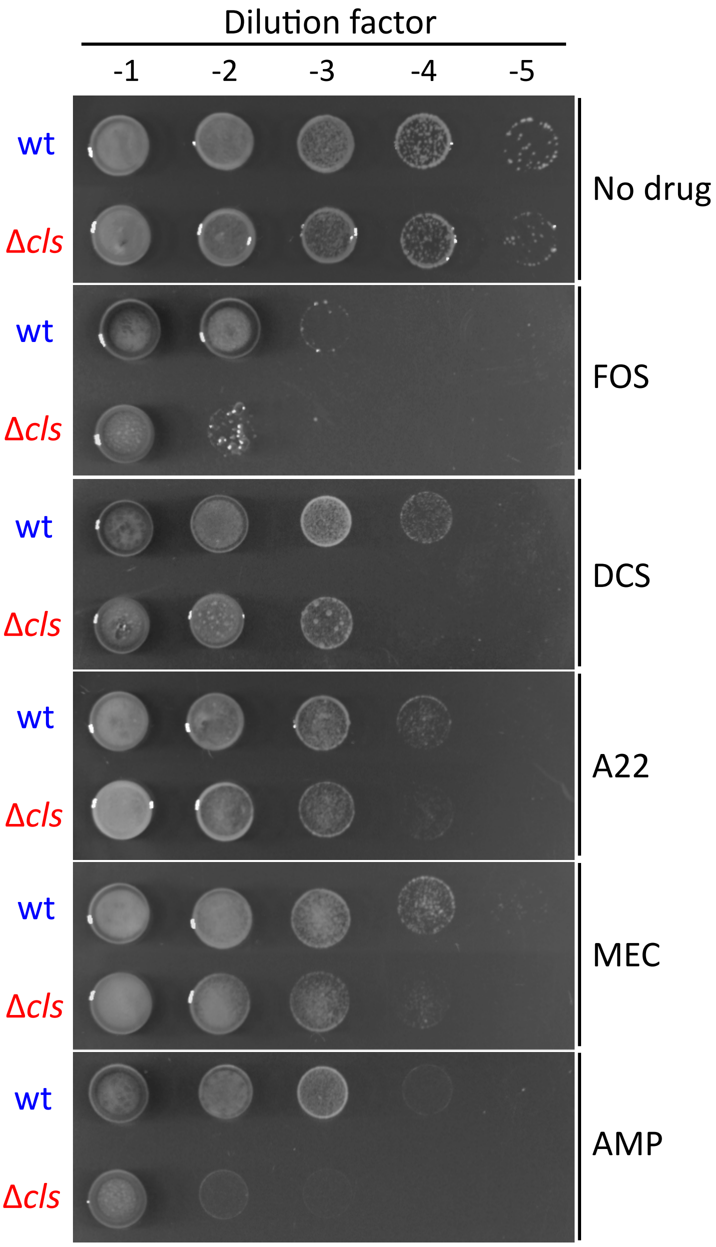
Dilution factor
-1
-2
-3
-4
-5
wt
Δcls
No drug
wt
Δcls
FOS
wt
Δcls
DCS
wt
Δcls
A22
wt
Δcls
MEC
wt
Δcls
AMP

**Figure 7**

# REFERENCES

1. **Yang DC, Blair KM, Salama NR.** 2016. Staying in Shape: the Impact of Cell Shape on Bacterial Survival in Diverse Environments. Microbiol Mol Biol Rev **80:**187-203.

2. **Young KD.** 2006. The selective value of bacterial shape. Microbiol Mol Biol Rev **70:**660-703.

3. **Cabeen MT, Jacobs-Wagner C.** 2005. Bacterial cell shape. Nat Rev Microbiol **3:**601-610.

4. **Typas A, Banzhaf M, Gross CA, Vollmer W.** 2011. From the regulation of peptidoglycan synthesis to bacterial growth and morphology. Nat Rev Microbiol **10:**123-136.

5. **van Teeseling MCF, de Pedro MA, Cava F.** 2017. Determinants of Bacterial Morphology: From Fundamentals to Possibilities for Antimicrobial Targeting. Front Microbiol **8:**1264.

6. **Teo AC, Roper DI.** 2015. Core Steps of Membrane-Bound Peptidoglycan Biosynthesis: Recent Advances, Insight and Opportunities. Antibiotics (Basel) **4:**495-520.

7. **Lin TY, Santos TM, Kontur WS, Donohue TJ, Weibel DB.** 2015. A Cardiolipin-Deficient Mutant of *Rhodobacter sphaeroides* Has an Altered Cell Shape and Is Impaired in Biofilm Formation. J Bacteriol **197:**3446-3455.

8. **Oliver PM, Crooks JA, Leidl M, Yoon EJ, Saghatelian A, Weibel DB.** 2014. Localization of anionic phospholipids in *Escherichia coli* cells. J Bacteriol **196:**3386-3398.

9. **Kawai F, Shoda M, Harashima R, Sadaie Y, Hara H, Matsumoto K.** 2004. Cardiolipin domains in *Bacillus subtilis* marburg membranes. J Bacteriol **186:**1475-1483.

10. **Zhang X, Tamot B, Hiser C, Reid GE, Benning C, Ferguson-Miller S.** 2011. Cardiolipin deficiency in *Rhodobacter sphaeroides* alters the lipid profile of membranes and of crystallized cytochrome oxidase, but structure and function are maintained. Biochemistry **50:**3879-3890.

11. **Ind AC, Porter SL, Brown MT, Byles ED, de Beyer JA, Godfrey SA, Armitage JP.** 2009. Inducible-expression plasmid for *Rhodobacter sphaeroides* and *Paracoccus denitrificans*. Appl Environ Microbiol **75:**6613-6615.

12. **van den Ent F, Amos LA, Lowe J.** 2001. Prokaryotic origin of the actin cytoskeleton. Nature **413:**39-44.

13. **Garner EC, Bernard R, Wang W, Zhuang X, Rudner DZ, Mitchison T.** 2011. Coupled, circumferential motions of the cell wall synthesis machinery and MreB filaments in *B. subtilis*. Science **333:**222-225.

14. **Dominguez-Escobar J, Chastanet A, Crevenna AH, Fromion V, Wedlich-Soldner R, Carballido-Lopez R.** 2011. Processive movement of MreB-associated cell wall biosynthetic complexes in bacteria. Science **333:**225-228.

15. **Errington J.** 2015. Bacterial morphogenesis and the enigmatic MreB helix. Nat Rev Microbiol **13:**241-248.

16. **Slovak PM, Wadhams GH, Armitage JP.** 2005. Localization of MreB in *Rhodobacter sphaeroides* under conditions causing changes in cell shape and membrane structure. J Bacteriol **187:**54-64.

17. **Meeske AJ, Riley EP, Robins WP, Uehara T, Mekalanos JJ, Kahne D, Walker S, Kruse AC, Bernhardt TG, Rudner DZ.** 2016. SEDS proteins are a widespread family of bacterial cell wall polymerases. Nature **537:**634-638.

18. **Cho H, Wivagg CN, Kapoor M, Barry Z, Rohs PD, Suh H, Marto JA, Garner EC, Bernhardt TG.** 2016. Bacterial cell wall biogenesis is mediated by SEDS and PBP polymerase families functioning semi-autonomously. Nat Microbiol doi:10.1038/nmicrobiol.2016.172**:**16172.

19. **Salje J, van den Ent F, de Boer P, Lowe J.** 2011. Direct membrane binding by bacterial actin MreB. Mol Cell **43:**478-487.

20. **Shiomi D, Toyoda A, Aizu T, Ejima F, Fujiyama A, Shini T, Kohara Y, Niki H.** 2013. Mutations in cell elongation genes mreB, mrdA and mrdB suppress the shape defect of RodZ-deficient cells. Mol Microbiol **87:**1029-1044.

21. **Kuru E, Hughes HV, Brown PJ, Hall E, Tekkam S, Cava F, de Pedro MA, Brun YV, VanNieuwenhze MS.** 2012. In Situ probing of newly synthesized peptidoglycan in live bacteria with fluorescent D-amino acids. Angew Chem Int Ed Engl **51:**12519-12523.

22. **den Blaauwen T, de Pedro MA, Nguyen-Disteche M, Ayala JA.** 2008. Morphogenesis of rod-shaped sacculi. FEMS Microbiol Rev **32:**321-344.

23. **Varma A, de Pedro MA, Young KD.** 2007. FtsZ directs a second mode of peptidoglycan synthesis in *Escherichia coli*. J Bacteriol **189:**5692-5704.

24. **Mengin-Lecreulx D, Texier L, Rousseau M, van Heijenoort J.** 1991. The murG gene of *Escherichia coli* codes for the UDP-N-acetylglucosamine: N-acetylmuramyl-(pentapeptide) pyrophosphoryl-undecaprenol N-acetylglucosamine transferase involved in the membrane steps of peptidoglycan synthesis. J Bacteriol **173:**4625-4636.

25. **Bupp K, van Heijenoort J.** 1993. The final step of peptidoglycan subunit assembly in *Escherichia coli* occurs in the cytoplasm. J Bacteriol **175:**1841-1843.

26. **van den Brink-van der Laan E, Boots JW, Spelbrink RE, Kool GM, Breukink E, Killian JA, de Kruijff B.** 2003. Membrane interaction of the glycosyltransferase MurG: a special role for cardiolipin. J Bacteriol **185:**3773-3779.

27. **Mann PA, Muller A, Xiao L, Pereira PM, Yang C, Ho Lee S, Wang H, Trzeciak J, Schneeweis J, Dos Santos MM, Murgolo N, She X, Gill C, Balibar CJ, Labroli M, Su J, Flattery A, Sherborne B, Maier R, Tan CM, Black T, Onder K, Kargman S, Monsma FJ, Jr., Pinho MG, Schneider T, Roemer T.** 2013. Murgocil is a highly bioactive staphylococcal-specific inhibitor of the peptidoglycan glycosyltransferase enzyme MurG. ACS Chem Biol **8:**2442-2451.

28. **Ha S, Walker D, Shi Y, Walker S.** 2000. The 1.9 A crystal structure of *Escherichia coli* MurG, a membrane-associated glycosyltransferase involved in peptidoglycan biosynthesis. Protein Sci **9:**1045-1052.

29. **Harris LK, Theriot JA.** 2016. Relative Rates of Surface and Volume Synthesis Set Bacterial Cell Size. Cell **165:**1479-1492.

30. **Barbosa MD, Ross HO, Hillman MC, Meade RP, Kurilla MG, Pompliano DL.** 2002. A multitarget assay for inhibitors of membrane-associated steps of peptidoglycan biosynthesis. Anal Biochem **306:**17-22.

31. **Powell GL, Hui SW.** 1996. Tetraoleoylpyrophosphatidic acid: a four acyl-chain lipid which forms a hexagonal II phase with high curvature. Biophys J **70:**1402-1406.

32. **Huang KC, Mukhopadhyay R, Wingreen NS.** 2006. A curvature-mediated mechanism for localization of lipids to bacterial poles. PLoS Comput Biol **2:**e151.

33. **Mukhopadhyay R, Huang KC, Wingreen NS.** 2008. Lipid localization in bacterial cells through curvature-mediated microphase separation. Biophys J **95:**1034-1049.

34. **Lin TY, Weibel DB.** 2016. Organization and function of anionic phospholipids in bacteria. Appl Microbiol Biotechnol **100:**4255-4267.

35. **Michaelis AM, Gitai Z.** 2010. Dynamic polar sequestration of excess MurG may regulate enzymatic function. J Bacteriol **192:**4597-4605.

36. **Gold VA, Robson A, Bao H, Romantsov T, Duong F, Collinson I.** 2010. The action of cardiolipin on the bacterial translocon. Proc Natl Acad Sci U S A **107:**10044-10049.

37. **Haines TH, Dencher NA.** 2002. Cardiolipin: a proton trap for oxidative phosphorylation. FEBS Lett **528:**35-39.

38. **Musatov A, Sedlak E.** 2017. Role of cardiolipin in stability of integral membrane proteins. Biochimie **142:**102-111.

39. **Tsirigotaki A, De Geyter J, Sostaric N, Economou A, Karamanou S.** 2017. Protein export through the bacterial Sec pathway. Nat Rev Microbiol **15:**21-36.

40. **Epand RM, Epand RF.** 2009. Domains in bacterial membranes and the action of antimicrobial agents. Mol Biosyst **5:**580-587.

41. **Wood JM.** 2018. Perspective: challenges and opportunities for the study of cardiolipin, a key player in bacterial cell structure and function. Curr Genet doi:10.1007/s00294-018-0811-2.

42. **Romantsov T, Gonzalez K, Sahtout N, Culham DE, Coumoundouros C, Garner J, Kerr CH, Chang L, Turner RJ, Wood JM.** 2018. Cardiolipin synthase A colocalizes with cardiolipin and osmosensing transporter ProP at the poles of *Escherichia coli* cells. Mol Microbiol **107:**623-638.

43. **Rowlett VW, Mallampalli V, Karlstaedt A, Dowhan W, Taegtmeyer H, Margolin W, Vitrac H.** 2017. Impact of Membrane Phospholipid Alterations in *Escherichia coli* on Cellular Function and Bacterial Stress Adaptation. J Bacteriol **199**.

44. **Rajendram M, Zhang L, Reynolds BJ, Auer GK, Tuson HH, Ngo KV, Cox MM, Yethiraj A, Cui Q, Weibel DB.** 2015. Anionic Phospholipids Stabilize RecA Filament Bundles in *Escherichia coli*. Mol Cell **60:**374-384.

45. **Rossi RM, Yum L, Agaisse H, Payne SM.** 2017. Cardiolipin Synthesis and Outer Membrane Localization Are Required for Shigella flexneri Virulence. MBio **8**.

46. **Dalebroux ZD, Edrozo MB, Pfuetzner RA, Ressl S, Kulasekara BR, Blanc MP, Miller SI.** 2015. Delivery of cardiolipins to the *Salmonella* outer membrane is necessary for survival within host tissues and virulence. Cell Host Microbe **17:**441-451.

47. **Bernal P, Munoz-Rojas J, Hurtado A, Ramos JL, Segura A.** 2007. A *Pseudomonas putida* cardiolipin synthesis mutant exhibits increased sensitivity to drugs related to transport functionality. Environ Microbiol **9:**1135-1145.

48. **Davis J, Donohue TJ, Kaplan S.** 1988. Construction, characterization, and complementation of a Puf- mutant of *Rhodobacter sphaeroides*. J Bacteriol **170:**320-329.

# SUPPORTING INFORMATION

## EXPERIMENTAL PROCEDURES

### Plasmid constructions

The primers used in this study are listed in Table S2. Cloning of PCR fragments into vectors were performed by In-Fusion Cloning (Clontech) in accordance with the user manual unless otherwise noted. The pIND5 and pK18*mobsac*B constructs were transformed into *E. coli* S17-1 and subsequently mobilized via conjugation into the recipient *R. sphaeroides* wt or Δ*cls* strain.

**pIND5TetR:** The tetracycline resistance gene was amplified by PCR using the primers RF-TetR-F and RF-TetR-R. The PCR product was used as megaprimers to replace the kanamycin resistance gene in pIND5 using the restriction-free method.

***gfp*-pIND5TetR:** *gfp* was amplified by PCR using the primers NdeI-*gfp*_p5 and BglII-*gfp*_p5 and cloned into pIND5TetR at the NdeI and BglII sites.

***gfp*-*murG*-pIND5TetR:** *murG* was amplified by PCR using the primers NdeI-*murG*_p5 and BglII-*murG*_p5 from *R. sphaeroides* 2.4.1 genomic DNA and cloned into pIND5TetR at the NdeI and BglII sites to generate *murG*-pIND5TetR. *gfp* was then amplified by PCR using the primers NdeI-*gfp*_p5 and *murG*-NdeI-*gfp* and cloned into *murG*-pIND5TetR at the NdeI site.

***gfp-murG*$^{L76E}$-pIND5TetR:** murG$^{L76E}$ was created by using the Stratagene QuikChange XL site-directed mutagenesis kit in accordance with the manufacturer's protocol. The primers used were *murG*_L76E_S and *murG*_L76E_AS.

**1k-*gfp-murG*-pK18*mobsacB*TetR:** *murG* and its 5′ upstream DNA sequence (~1 kb) was amplified by PCR using the primers BamHI-*murG1k* and HindIII-*murG1k* from *R. sphaeroides* 2.4.1 genomic DNA and cloned into pK18*mobsacB*TetR at the BamHI and HindIII sites to generate *1k*-*murG*-pK18*mobsacB*TetR. An NdeI site was inserted into *1k*-*murG*-pK18*mobsacB*TetR between *murG* and its 5′ upstream DNA sequence by the Stratagene QuikChange XL site-directed mutagenesis kit using the primers *murG1k*+NdeI_S and *murG1k*+NdeI_AS to create *1k*-NdeI-*murG*-pK18*mobsacB*TetR. *gfp* was then amplified by PCR using the primers *murG1k*-NdeI-*gfp* and *murG*-NdeI-*gfp* and cloned into *1k*-NdeI-*murG*-pK18*mobsacB*TetR at the NdeI site.

***murG*-pET28b(+):** *murG* was amplified by PCR using the primers NdeI-*murG*_p28 and XhoI-*murG*_p28 and cloned into pET28b(+) at the NdeI and XhoI sites. The MurG expressed from the pET28b(+) vector contained an N-terminal His•Tag followed by a thrombin cleavage sequence.

***mreB*-pET20b(+):** *mreB* was amplified by PCR using the primers NdeI-*mreB*_p20 and XhoI-*mreB*_p20 from *R. sphaeroides* 2.4.1 genomic DNA and cloned into pET20b(+) at the NdeI and XhoI sites. The MreB expressed from the pET20b(+) vector contained a C-terminal His•Tag.

***mreB*$^{\Delta N}$-pET20b(+):** *mreB*$^{\Delta N}$ (a mutant lacking the N-terminal helix) was amplified by PCR using the primers NdeI-*mreB*$^{\Delta N}$ _p20 and XhoI-*mreB*_p20 and cloned into pET20b(+) at the NdeI and XhoI sites. The MreB expressed from the plasmid lost its first 9 amino acids and contained a C-terminal His•Tag.

***mreBH1-gfp*-pIND5:** The primers NdeI-*mreBH1* and BglII-*mreBH1* were annealed and ligated into pIND5 at the NdeI and BglII sites to create *mreBH1*-pIND5. *gfp* was then amplified by PCR using the primers *mrebBH1*-BglII-*gfp* and BglII-*gfp*_p5 and cloned into *mreBH1*-pIND5 at the BglII site.

**2X*mreBH1-gfp*-pIND5:** The primers NdeI-2X*mreBH1* and BglII-2X*mreBH1* were annealed and ligated into pIND5 at the NdeI and BglII sites to create 2X*mreBH1*-pIND5. *gfp* was then amplified by PCR using the primers *mrebBH1*-BglII-*gfp* and BglII-*gfp*_p5 and cloned into *mreBH1*-pIND5 at the BglII site.

***mreBH2-gfp*-pIND5:** *gfp* amplified by PCR using the primers NdeI-*mrebBH2*-*gfp*_p5 and BglII-*gfp*_p5 and cloned into pIND5 at the NdeI and BglII sites.

**2X*mreBH2-gfp*-pIND5:** The primers NdeI-*mreB*H2-F and NdeI-*mreB*H2-R were annealed and cloned into *mreBH2-gfp*-pIND5 at the NdeI site.

***mreBH1-H2-gfp*-pIND5:** The primers NdeI-*mreBH1*-F and NdeI-*mreBH1*-R were annealed and cloned into *mreBH2-gfp*-pIND5 at the NdeI site.

***ftsZ-mCherry*-pIND5:** *ftsZ* was amplified by PCR using the primers NdeI-*ftsZ*_p5 and BglII-*ftsZ*_p5 from *R. sphaeroides* 2.4.1 genomic DNA and cloned into pIND5 at the NdeI and BglII sites to generate *ftsZ*-pIND5. *mCherry* was then amplified by PCR using the primers BglII-*mCherry*_p5 and *ftsZ*-BglII-*mCherry* and cloned into *ftsZ*-pIND5 at the BglII site.

### Creation of TyL1 and TyL2

1k-*gfp-murG*-pK18*mobsacB*TetR was introduced into *R. sphaeroides* wt or Δ*cls* cells by conjugation. The integration of plasmid into *R. sphaeroides* genome through homologous recombination was selected by plating cells on plates containing Sistrom's minimal medium with 1.5% agar and tetracycline. Single colony was picked into plain Sistrom's minimal medium and grown for two days. The excision of the plasmid from the genome through a second homologous recombination was selected by plating cells on plates containing Sistrom's minimal medium with 1.5% agar and 10% sucrose. The insertion of *gfp* between *murG* and its upstream sequences was confirmed by PCR using the primes WSG and HindIII-*murG1k*.

## qPCR

Cells were grown to log phase (absorbance of 0.6, $\lambda = 600$ nm), and RNA was isolated as previously described. The RNA samples were then treated with RNase-free DNase (Qiagen, Valencia, CA) and further purified with an RNeasy CleanUp kit (Qiagen, Valencia, CA). cDNA synthesis was performed with a High Capacity RNA-to-cDNA kit (Applied Biosystems, Foster City, CA). Five nanograms of cDNA was used for each qPCR reaction. The Applied Biosystems 7500 real-time PCR system (Applied Biosystems, Foster City, CA) with SYBR green chemistry was used to monitor amplification and to quantify the amounts of PCR products. Relative quantitation of gene expression was calculated by the $\Delta\Delta C_T$ method, in which the level of *rpoZ* gene (encodes the Ω subunit of RNA polymerase) expression was used as an internal control. The qPCR primers used in this study are listed in Table S3.

## PG isolation and UPLC/MS analysis

Cells were grown in plain medium or medium containing the indicated small molecule inhibitors (A22: 10 μg/ml; MEC: 0.5 μg/ml; FOS: 250 μg/ml; DCS: 0.05 μg/ml) to early log phase (absorbance of 0.3, $\lambda = 600$ nm) and pelleted by centrifugation at 4,000 × *g* for 10 min at room temperature. Cells were then resuspended in 1 ml 0.25% SDS (in 0.1 M Tris/HCl, pH 6.8) and boiled for 40 min. The cell suspension was centrifuged at 10,000 × *g* for 5 min at room temperature and the pellet was washed with $ddH_2O$ to remove SDS. The pellet was then resuspended in 1 ml $ddH_2O$ and put in a waterbath sonicator for 30 min at room temperature. 500

μl of nuclease solution (15 μg/ml DNase and 60 μg/ml RNase in 0.1 M Tris/HCl, pH 6.8) was added into the sample that was then incubated for 60 min at 37°C in a shaker. The sample was added 500 μl trypsin solution (50 μg/ml trypsin in $ddH_2O$), incubated for another 60 min at 37°C in a shaker and then boiled for 15 min to inactivate the enzymes. The suspension was centrifuged at 10,000 × *g* for 5 min at room temperature and the pellet was washed with $ddH_2O$. The pellet was resuspended in digestion buffer (12.5 mM sodium dihydrogen-phosphate, pH 5.5) to an absorbance of 3.0 ($\lambda$ = 600 nm) and added 1/10 volume of mutanolysin solution (5.000 U/ml of mutanolysin in $ddH_2O$). The sample (~175 μl) was incubated for 16 h at 37°C in a shaker and then boiled for 15 min to inactivate the enzyme. The suspension was centrifuged at 10,000 × *g* for 5 min at room temperature and PG was in the supernatant. 50 μl of reduction solution (20 mg/ml sodium borohydrate in 0.5 M borax in $ddH_2O$ at pH 9.0) was added into the PG solution that was then incubated for 30 min at room temperature. The sample was adjusted to pH 2.0-3.0 with phosphoric acid solution (50%) and analyzed by UPLC/MS.

For UPLC/MS, we injected 7.5 μL of purified muropeptides on a Cortecs 2.1 x 100 mm C18 column (Waters) packed with 1.6 μm-diameter particles and equipped with a Cortecs C18 guard column (Waters). The column temperature maintained at 52°C using an Acquity standard flow UPLC system equipped with an inline photodiode array (Waters). For muropeptide separation by UPLC, we used solvent A (Optima LCMS-grade water with 0.05% trifluoroacetic acid) and solvent B (30% (v/v) Optima LCMS-grade methanol in Optima LCMS-grade water with 0.05%

trifluoroacetic acid) (Fisher Scientific). Muropeptides were eluted from the column with a gradient of increasing solvent B (1 min hold at 1% B, to 99% B at 60 min, hold 99% B 5 min, to 1% B at 65.5 min, 4.5 min hold at 1% B) at a flow rate of 0.2 ml/min. We analyzed the eluent from the column using a Bruker MaXis Ultra-High Resolution time-of-flight 4G mass spectrometer (Bruker Daltonic) with an MS method. The capillary voltage was set to 4100 V, the nebulizer pressure was 2.0 bar, and the drying gas was set to 6.0 L/m at 220°C. Muropeptides were detected at $\lambda$=205 nm and via MS.

### Cell fractionation

Cells were grown to early log phase (absorbance of 0.3, $\lambda$ = 600 nm), pelleted by centrifugation at 5,000 × *g* for 10 min at 4°C and then resuspended in Buffer T (20 mM Tris-Cl, pH 8.0). Cells were passed through a Constant Systems Cell Disruptor (Constant Systems Ltd.) at 10,000 psi and the resulting cell lysate was clarified by centrifugation at 5,000 × *g* for 10 min at 4°C. The clear lysate was quantified and equal amounts of wt and Δ*cls* lysates were brought to the same volume using Buffer T, followed by centrifugation at 45,000 × *g* for 30 min at 4°C and divided into supernatant and pellet (dissolved in Buffer T) fractions. The same amounts of proteins in the supernatant (enriched in cytosolic proteins) and pellet (enriched in membrane proteins) fractions were subjected to Western blot analysis using anti-MreB or anti-GFP antibodies.

### NAO staining

Cells were grown to early log phase (absorbance of 0.3, $\lambda$ = 600 nm), and NAO at a final concentration of 10 μM was added into the cultures that were grown for another 4 h. Cells were then imaged under a fluorescence microscope using 480 nm excitation and 685 nm emission filters.

### MurG purification

*E. coli* BL21(DE3) cells transformed with pET28b containing *R. sphaeroides murG* were grown to an absorbance of 0.6 ($\lambda$ = 600 nm) and induced with 1 mM IPTG for 3 h at 37°C. Cells were pelleted by centrifugation at 4,000 × *g* for 10 min at 4°C and then resuspended in Buffer T containing 5 mM imidazole and 0.1 mM PMSF. Cells were passed through a Constant Systems Cell Disruptor (Constant Systems Ltd.) at 20,000 psi and the resulting cell lysate was mixed with Triton X-100 at a final concentration of 3% for 1 h at 4°C with rotation. The supernatant and insoluble fractions were separated by centrifugation at 25,000 × *g* for 40 min at 4°C. The supernatant was subjected to a Ni-NTA agarose (Qiagen) column equilibrated with Buffer T. The column was washed stepwise with Buffer T, 25 imidazole in Buffer T and then 50 mM imidazole in Buffer T, and the MurG protein was eluted with 100 mM imidazole in Buffer T. The protein was concentrated into Buffer T (without imidazole) using a 10 kDa cutoff spin column (Millipore). To remove the His•Tag from the recombinant protein, the protein concentrate was subjected to thrombin (Millipore) cleavage with a dilution factor for thrombin of 1:200 for 16 h at 22°C. The reaction mixture was mixed with 25 μL of streptavidin agarose beads at 22°C for 30 min with rotation followed by centrifugation in a spin filter (Millipore). The filtrate, free of biotinylated thrombin, was concentrated into Buffer T using a 10 kDa cutoff spin column. To remove undigested protein, 25 μL of Ni-NTA agarose was added to the resulting protein concentrate and the sample was incubated at 22°C for 30 min with rotation. The Ni-NTA agarose was removed using a spin filter. The concentration of MurG with a molar extinction coefficient of 21,430 $cm^{-1}M^{-1}$ was determined by measuring the absorbance at $\lambda$=280 nm.

### Liposome preparation

Phospholipids used in this study were purchased from Avanti Polar Lipids: 1,2-di-(9Z-octadecenoyl)-*sn*-glycero-d-phosphocoline (PC), 1,2-di-(9Z-octadecenoyl)-*sn*-glycero-d-phospho-(1′-rac-glycerol) (PG) and 1,1′,2,2′-tetra-(9Z-octadecenoyl) cardiolipin (CL). To prepare liposomes of uniform size, lipid mixtures were dissolved in chloroform, dried in a glass vial and rehydrated in Buffer T. The resulting liposome solutions were then frozen in liquid nitrogen and thawed in 37°C water bath 5 times, followed by extrusion (Avanti Polar Lipid Mini Extruder) 15 times through a membrane filter (Whatman) with a pore size of 1 μm.

### Liposome-pelleting Assay

To block nonspecific binding, phospholipids at 21 mM were pre-incubated with 2.5 μM of bovine serum albumin (BSA) in Buffer T for 10 min. MurG in Buffer T was then added into the solution, resulting in a final MurG concentration of 1.7 μM, phospholipid concentration of 12.5 mM, and BSA concentration of 1.5 μM. The reaction was incubated for 30 min, centrifuged at 16300 × *g* for 30 min, and then divided into supernatant and pellet (dissolved in Buffer T) fractions. All the procedures were performed at room temperature. Proteins in the supernatant and pellet fractions were subjected to SDS-PAGE and visualized by coomassie blue staining.

**Figure S1.** ***R. sphaeroide* Δ*cls* cells have a lower cell elongation rate (compared to wt cells) and an ellipsoidal cell shape.** Probability density histogram of the cell length distribution of *R. sphaeroides* wt cells (A), Δ*cls* cells (B), and Δ*cls* cells expressing Cls (C). Cells in log phase (absorbance of 0.6, $\lambda = 600$ nm) were imaged by phase-contrast bright-field microscopy. Scale bar, 2 µm. Each data point represents a mean value ± standard deviation of the cell length (L), width (W), and aspect ratio (AR) for 300 cells determined by ImageJ. The shaded blue area overlaying the histogram represents the Kernel density estimation (KDE) of the cell length distribution. We overlaid a grey dashed line outlining the KDE of the cell length distribution of *R. sphaeroides* wt cells with the three histograms for comparison. Levels of CL in cells were determined from a TLC plate. Each data point (mean value ± standard deviation) was obtained from three independent experiments. For details, see ref. #7 and #10. (D) Representative time-lapse micrographs of *R. sphaeroides* wt, Δ*cls* cells, and Δ*cls* cells expressing Cls. Cells in early log phase (absorbance of 0.3, $\lambda = 600$ nm) were imaged using phase-contrast bright-field microscopy. We determined the cell elongation rate ($\Delta L/\Delta t$) by $(L_{90} - L_0)/90$ (nm/min); $L_{90}$ is the cell length at 90 min; $L_0$ is the cell length at 0 min. Each data point (mean value ± standard deviation) was determined by imaging ≥23 cells and using ImageJ to determine cell length.

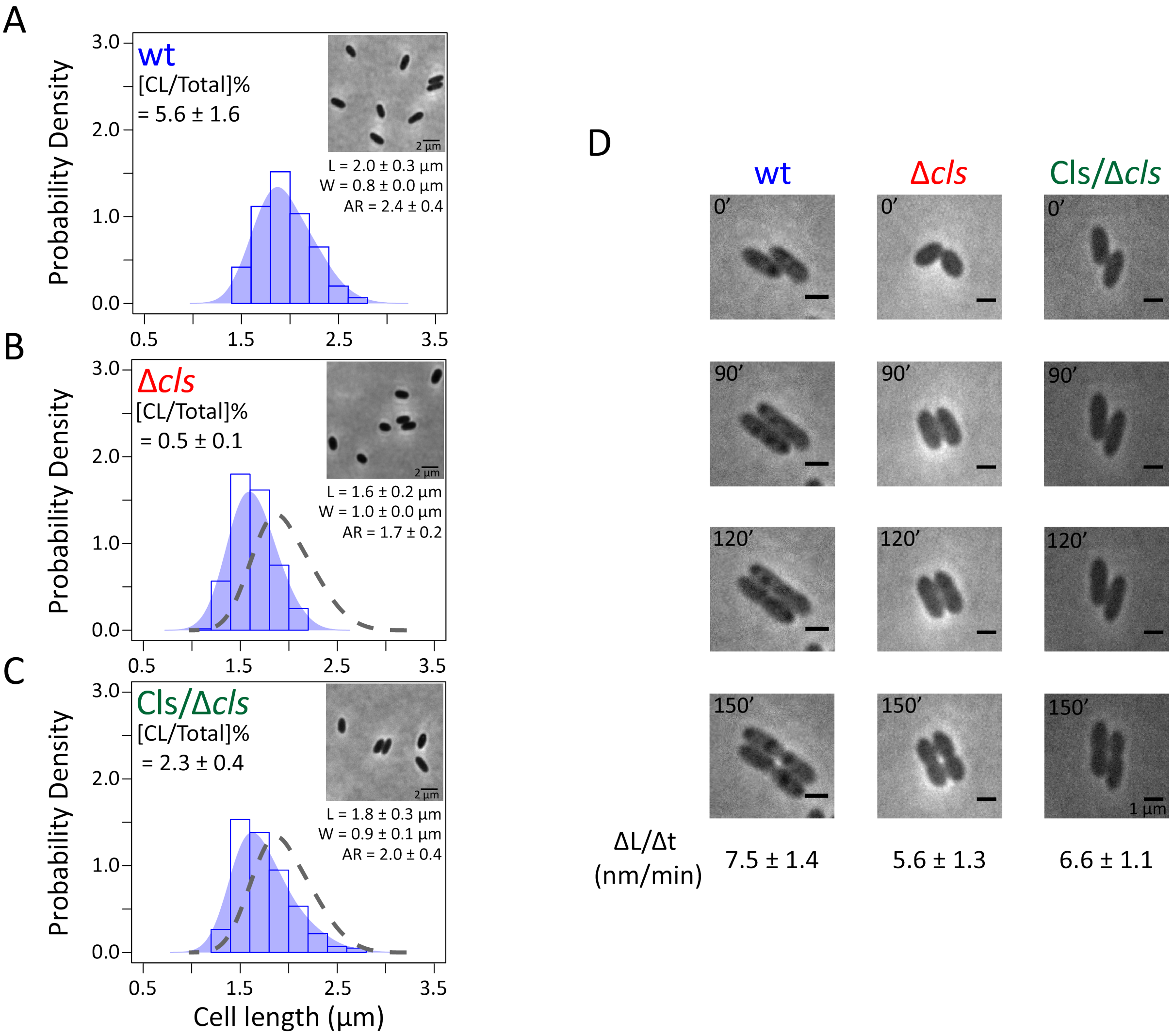
A
wt
[CL/Total]%
= 5.6 ± 1.6
2 µm
L = 2.0 ± 0.3 µm
W = 0.8 ± 0.0 µm
AR = 2.4 ± 0.4
B
Δcls
[CL/Total]%
= 0.5 ± 0.1
2 µm
L = 1.6 ± 0.2 µm
W = 1.0 ± 0.0 µm
AR = 1.7 ± 0.2
C
Cls/Δcls
[CL/Total]%
= 2.3 ± 0.4
2 µm
L = 1.8 ± 0.3 µm
W = 0.9 ± 0.1 µm
AR = 2.0 ± 0.4
Probability Density
3.0
2.0
1.0
0.0
0.5
1.5
2.5
3.5
Cell length (µm)
D
wt
Δcls
Cls/Δcls
0′
90′
120′
150′
1 µm
ΔL/Δt (nm/min)
7.5 ± 1.4
5.6 ± 1.3
6.6 ± 1.1

**Figure S1**

**Figure S2. CL deficiency does not affect the expression level of the elongasome in *R. sphaeroides*.** (A) Schematic diagram showing *mre* and *mrd* loci in *R. sphaeroides* genome. The *mre* locus is composed of *mreB*, *mreC,* and *mreD*; the *mrd* locus contains *pbp2* and *rodA*. These two loci cluster together and are suggested to be organized as a single operon in *R. sphaeroides* genome. (B) The expression levels of elongasome genes in *R. sphaeroides* wt and Δ*cls* cells were assayed by qPCR. Shown are mean values ± standard deviations obtained from three independent experiments, each performed in triplicate. All the differences (< 50%) are considered to be insignificant.

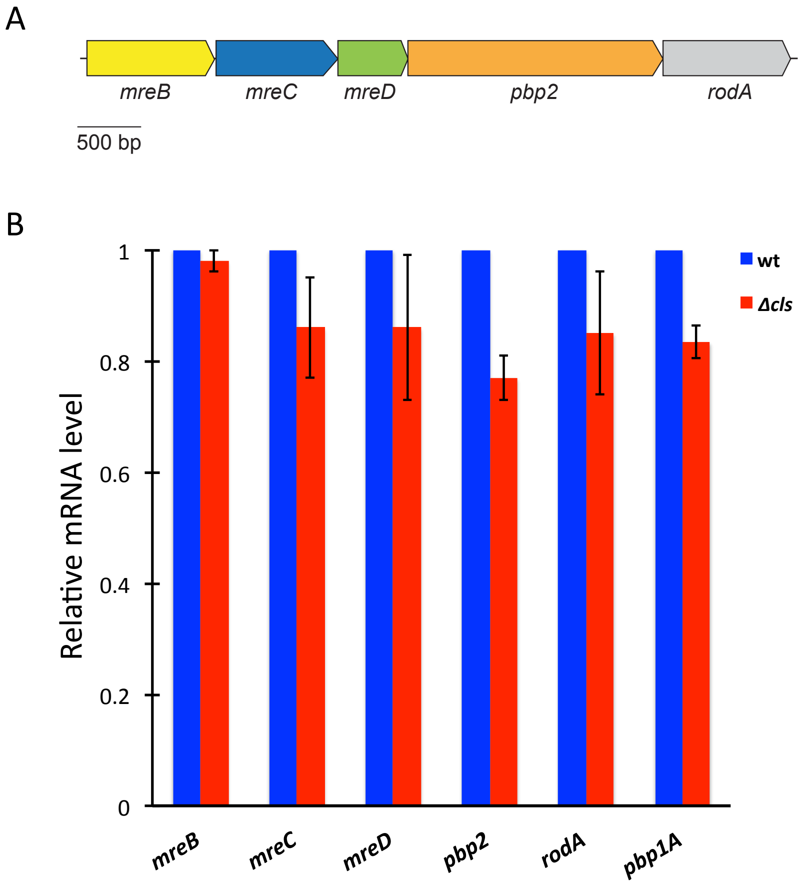
A
mreB
mreC
mreD
pbp2
rodA
500 bp
B
Relative mRNA level
0
0.2
0.4
0.6
0.8
1
wt
Δcls
mreB
mreC
mreD
pbp2
rodA
pbp1A

**Figure S2**

**Figure S3. Inhibition of PBP1a does not cause a change in *R. sphaeroides* cell shape.** Probability density histogram of the cell length distribution of *R. sphaeroides* wt cells treated with CEF. Cells were grown in medium containing 5 μg/ml CEF until they reached log phase (absorbance of 0.6, $\lambda$ = 600 nm) and imaged by phase-contrast bright-field microscopy. Scale bar, 2 μm. Each data point represents a mean value ± standard deviation of the cell length (L), width (W), and aspect ratio (AR) for 300 cells determined by ImageJ. The shaded blue area overlaying the histogram represents the Kernel density estimation (KDE) of the cell length distribution. We overlaid a grey dashed line outlining the KDE of the cell length distribution of *R. sphaeroides* wt cells with the histogram for comparison.

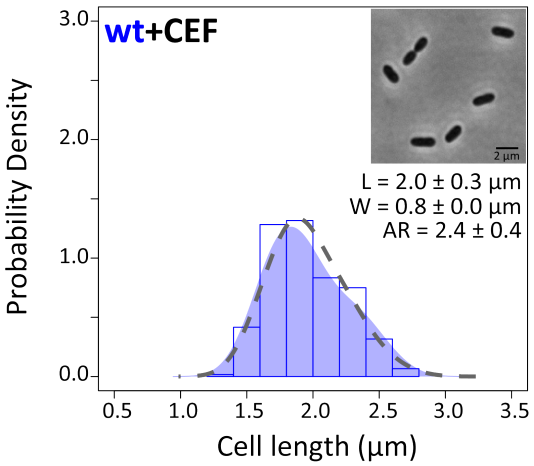
wt+CEF
Probability Density
3.0
2.0
1.0
0.0
0.5
1.0
1.5
2.0
2.5
3.0
3.5
Cell length (μm)
2 μm
L = 2.0 ± 0.3 μm
W = 0.8 ± 0.0 μm
AR = 2.4 ± 0.4

**Figure S3**

**Figure S4. Multiple sequence alignment of MreBs.** Amino acid sequences of MreB from *Thermotoga maritima, E. coli* and *R. sphaeroides* are aligned using CLUSTAL O. Stars indicate conserved residues; colons indicate residues with similar size and hydropathy; periods indicate residues with similar size or hydropathy. Amino acids are highlighted: in red for residues involved in membrane binding, in yellow for residues involved in ATPase activity, and in blue for residues involved in A22 sensitivity. *T. maritima* MreB interacts with the membrane via a membrane insertion loop containing two hydrophobic residues, leucine and phenylalanine (L93, F94); *E. coli* MreB binds membranes by an N-terminal amphipathic helix (residues 1-9); In addition to the N-terminal amphipathic helix (residues 1-9), *R. sphaeroides* MreB may contain an internal amphipathic helix (residues 87-97) that is also involved in membrane binding.

```
T. maritima MreB     -------MLRKDIGIDLGTANTLVFLRGKGIVVNEPSVIAIDST----TGEILKVGLEAK   49
E. coli MreB         MLKKFRGMFSNDLSIDLGTANTLIYVKGQGIVLNEPSVVAIRQDRAGSPKSVAAVGHDAK   60
R. sphaeroides MreB  -MSFLTGLFSSDMAIDLGTANTLIYVRGKGIVLSEPSVVAYHVK--DGKKQVLAVGEDAK   57
                            :: .*:.*********::::*:***:.****:*          .:  ** :**

T. maritima MreB     NMIGKTPATIKAIRPMRDGVIADYTVALVMLRYFINKAKGGMNL-FKPRVVIGVPIGITD   108
E. coli MreB         QMLGRTPGNIAAIRPMKDGVIADFFVTEKMLQHFIKQVHSNSFMRPSPRVLVCVPVGATQ   120
R. sphaeroides MreB  LMLGRTPGSIEAIRPMREGVIADFDTAEEMIKHFIRKVHKRTTF-SKPKIIVCVPHGATP   116
                      *:*:**..* *****::*****: .:  *:::**.:.:    :  .*:::: ** * *

T. maritima MreB     VERRAILDAGLEAGASKVFLIEEPMAAAIGSNLNVEEPSGNMVVDIGGGTTEVAVISLGS   168
E. coli MreB         VERRAIRESAQGAGAREVFLIEEPMAAAIGAGLPVSEATGSMVVDIGGGTTEVAVISLNG   180
R. sphaeroides MreB  VEKRAIRQSVLSAGARRAGLIAEPIAAAIGAGMPITDPTGNMVVDVGGGTTEVAVLSLGD   176
                     **:*** ::   ***  .. ** **:*****: : : :*.****:*********:**

T. maritima MreB     IVTWESIRIAGDEMDEAIVQYVRETYRVAIGERTAERVKIEIGNVFPSKENDELETTVSG   228
E. coli MreB         VVYSSSVRIGGDRFDEAIINYVRRNYGSLIGEATAERIKHEIGSAYPGDEV--REIEVRG   238
R. sphaeroides MreB  IVYARSVRVGGDRMDEAIVAYLRRHQNLLIGDSTAERIKTSIGTARMPDDGRGQSMTIRG   236
                     :*   *:*:.**.:****: *:*.     **: ****:* .**..   .:    .  : *

T. maritima MreB     IDLSTGLPRKLTLKGGEVREALRSVVVAIVESVRTTLEKTPPELVSDIIERGIFLTGGGS   288
E. coli MreB         RNLAEGVPRGFTLNSNEILEALQEPLTGIVSAVMVALEQCPPELASDISERGMVLTGGGA   298
R. sphaeroides MreB  RDLLNGVPKETEINQAQVAEALAEPVQQICDAVMQALEATPPDLAADIVDRGVMLTGGGA   296
                      :*  *:*:   ::  :: *** . :  * .:*  :**  **:*.:** :**:.*****:

T. maritima MreB     LLRGLDTLLQKETGISVIRSEEPLTAVAKGAGMVLDKVNILKKLQGAG-         336
E. coli MreB         LLRNLDRLLMEETGIPVVVAEDPLTCVARGGGKALEMIDMHGGDLFSEE         347
R. sphaeroides MreB  LLGDLDLALREQTGLSISVANESLNCVALGTGKALEYEKQLRHVIDYES         345
                     **  **  * ::**: :  ::: *..** * * .*:  .
```

# Figure S4

**Figure S5. *R. sphaeroides* MreB is highly insoluble and difficult to purify.** *E. coli* BL21(DE3)pLysS cells transformed with pET20b containing *R. sphaeroides mreB* or a mutant lacking the N-terminal helix were grown to an absorbance of 0.6 ($\lambda = 600$ nm) and induced with 1 mM IPTG for 3 h at 37°C. Cells were pelleted by centrifugation at 4,000 × *g* for 10 min at 4°C and then resuspended in Buffer T. Cells were passed through a Constant Systems Cell Disruptor (Constant Systems Ltd.) at 20,000 psi and the resulting cell lysate was mixed with Triton X-100 at a final concentration of 3% for 1 h at 4°C with rotation. The supernatant and pellet fractions were separated by centrifugation at 25,000 × *g* for 40 min at 4°C. Samples were subjected to SDS-PAGE and stained with coomassie blue. Lane 1: Molecular weight marker. Lane 2: Uninduced cell lyate. Lane 3: Cell lysate after IPTG induction of full-length MreB (FL). Lane 4: Supernatant (S). Lane 5: Pellet (P). Lane 6: Molecular weight marker. Lane 7: Uninduced cell lyate. Lane 8: Cell lysate after IPTG induction of an MreB mutant lacking the N-terminal helix (ΔN). Lane 9: Supernatant (S). Lane 10: Pellet (P). Overproduced MreB proteins appeared as a thick band of approximately 37 kDa after IPTG induction.

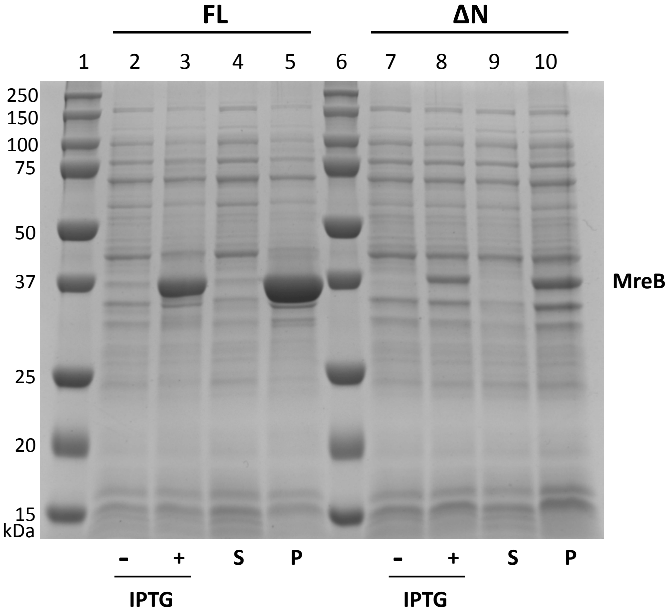
FL
ΔN
1
2
3
4
5
6
7
8
9
10
250
150
100
75
50
37
25
20
15
kDa
MreB
-
+
S
P
-
+
S
P
IPTG
IPTG

Figure S5

**Figure S6. Amphipathic helix prediction on *R. sphaeroides* MreB.** Results of amphipathic helix prediction on *R. sphaeroides* MreB from AMPHIPASEEK software. Predicted in-plane membrane anchors are indicated by red 'A's.

# *R. sphaeroides* MreB

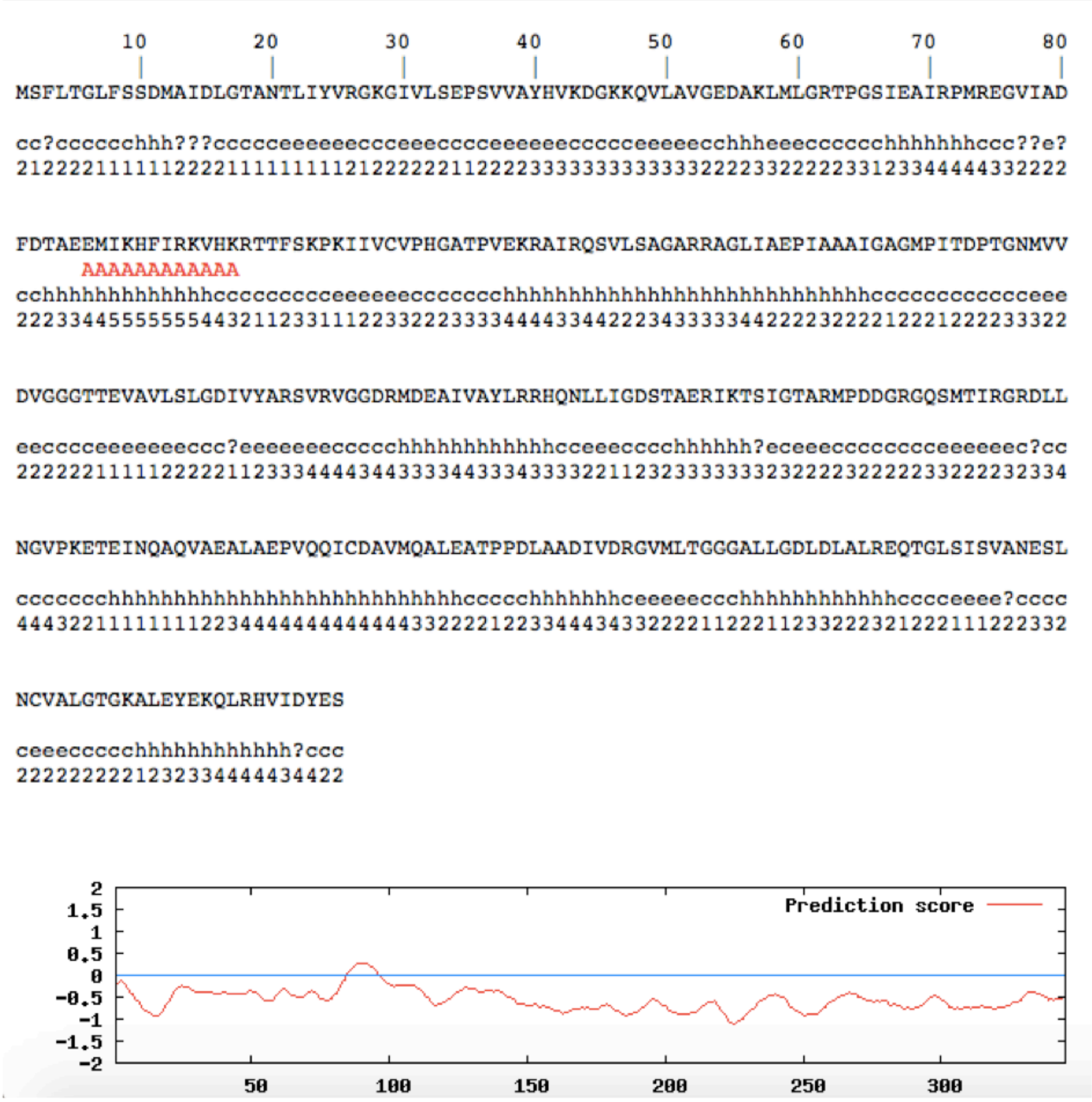

```
           10        20        30        40        50        60        70        80
            |         |         |         |         |         |         |         |
MSFLTGLFSSDMAIDLGTANTLIYVRGKGIVLSEPSVVAYHVKDGKKQVLAVGEDAKLMLGRTPGSIEAIRPMREGVIAD

cc?cccccchhh???ccccceeeeeeccceeecccceeeeeeecccceeeeeecchhheeecccccchhhhhhhhccc??e?
21222211111222211111111121222222112222333333333333322223322222331233444444332222


FDTAEEMIKHFIRKVHKRTTFSKPKIIVCVPHGATPVEKRAIRQSVLSAGARRAGLIAEPIAAAIGAGMPITDPTGNMVV
     AAAAAAAAAAAA
cchhhhhhhhhhhhhcccccccccceeeeeeccccchhhhhhhhhhhhhhhhhhhhhhhhhhhhcccccccccccceee
22233445555555443211233111223322233334444334422234333334422223222212221222233322


DVGGGTTEVAVLSLGDIVYARSVRVGGDRMDEAIVAYLRRHQNLLIGDSTAERIKTSIGTARMPDDGRGQSMTIRGRDLL

eeccccceeeeeeeccc?eeeeeeeecccchhhhhhhhhhhhcceeeeccchhhhhh?eceeeecccccccceeeeec?cc
22222211111222221123334444344333344333433332211232333333323222232222233222232334


NGVPKETEINQAQVAEALAEPVQQICDAVMQALEATPPDLAADIVDRGVMLTGGGALLGDLDLALREQTGLSISVANESL

ccccccchhhhhhhhhhhhhhhhhhhhhhhhhhhhcccccchhhhhhhceeeeeccchhhhhhhhhhhhcccceeee?cccc
44432211111111223444444444444444433222212233444343322221122211233222321222111222332


NCVALGTGKALEYEKQLRHVIDYES

ceeeccccchhhhhhhhhhhhh?ccc
2222222221232334444434422
```

**Figure S6**

**Figure S7. Antibody against *E. coli* MreB (EcMreB) recognizes *R. sphaeroides* MreB (RsMreB).** To examine whether the polyclonal anti-EcMreB antibody can recognize RsMreB, we overproduced RsMreB using the pET *E. coli* expression system and verified the protein expression by SDS-PAGE and Western blot. (A) SDS-PAGE of RsMreB stained with coomassie blue. Lane 1: Molecular weight marker. Lane 2: Uninduced cell lyate. Lane 3: Cell lysate after 3 h induction of RsMreB by IPTG. Overproduced RsMreB appeared as a thick band of approximately 37 kDa after IPTG induction. (B) The same uninduced and induced cell lysates were also verified by Western blot using the polyclonal antibody against EcMreB. Not only did the antibody detect the endogenous EcMreB in the uninduced cell lysate (Lane 1), it also recognized the overproduced RsMreB in the cell lysate after 3 h induction by IPTG (Lane 2). Both MreBs had a molecular weight of ~37 kDa and were indistinguishable from each other in Lane 2.

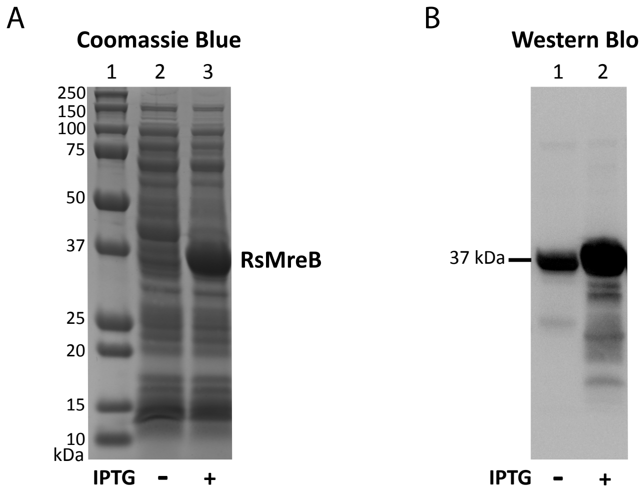
A
Coomassie Blue
1 2 3
250
150
100
75
50
37
25
20
15
10
kDa
RsMreB
IPTG - +
B
Western Blot
1 2
37 kDa
IPTG - +

**Figure S7**

**Figure S8. CL deficiency does not affect MreB protein expression in *R. sphaeroides*.** *R. sphaeroides* wt and Δ*cls* cell lysates that had the same amounts of proteins were subjected to Western blot analysis using a polyclonal antibody against MreB. The amount of MreB in cells was determined by quantifying the optical densitometry signal with ImageJ. Data represent mean values ± standard deviations obtained from three independent experiments.

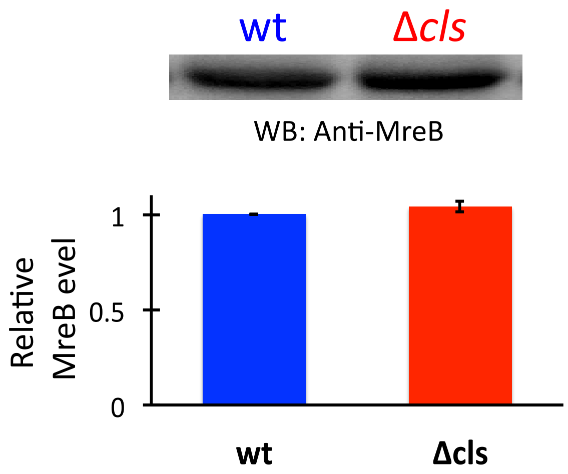

**Figure S8**

**Figure S9. Chromatograms of purified muropeptides from *R. sphaeroides* wt cells, Δ*cls* cells, wt cells treated with FOS, wt cells treated with DCS, wt cells treated with A22, and wt cells treated with MEC.** Cell walls were digested, purified and analyzed by UPLC-MS. Identified peaks are provided in Table S4. Quantification of peaks is shown in Fig. 4. * denotes a peak of undesirable contaminants in the column.

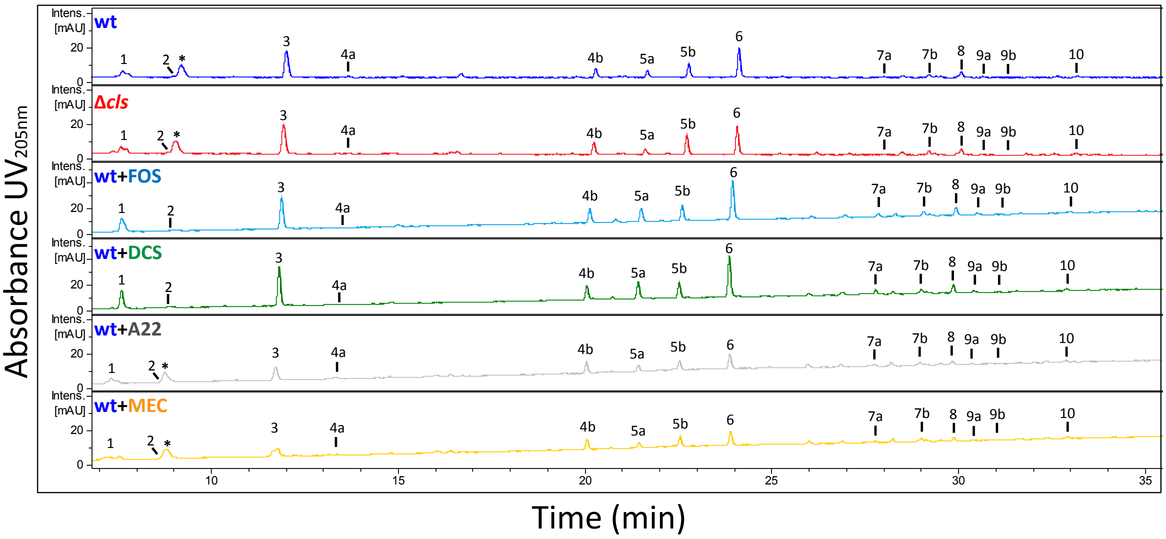
Absorbance UV$_{205nm}$
Intens. [mAU]
wt
Δcls
wt+FOS
wt+DCS
wt+A22
wt+MEC
20
0
1
2
*
3
4a
4b
5a
5b
6
7a
7b
8
9a
9b
10
15
20
25
30
35
Time (min)

**Figure S9**

**Figure S10. CL deficiency does not affect expression levels of the genes coding for enzymes responsible for PG precursor biosynthesis in *R. sphaeroides.*** The expression levels of genes synthesizing lipid II in *R. sphaeroides* wt and Δ*cls* cells were assayed by qPCR. Shown are mean values ± standard deviations obtained from three independent experiments, each performed in triplicate. All the differences (< 50%) are considered to be insignificant.

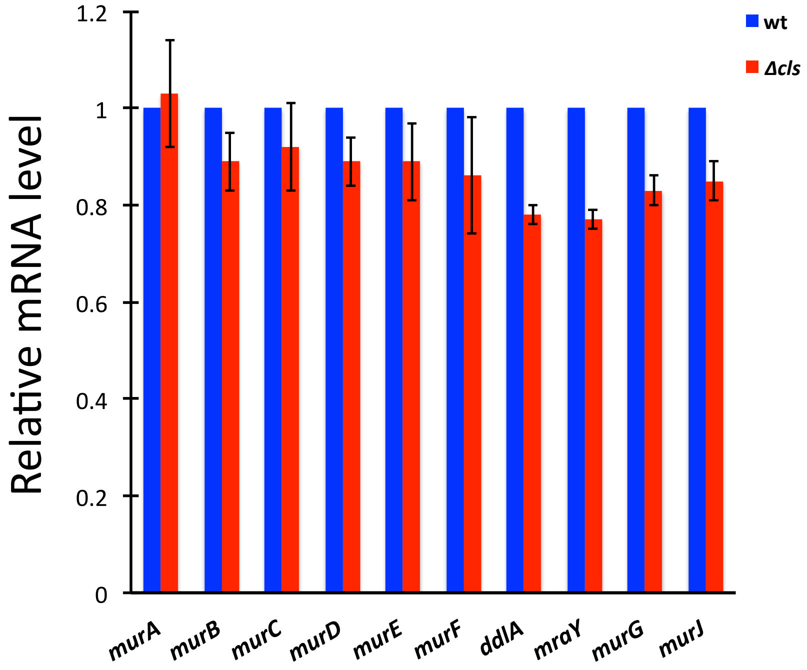
Relative mRNA level
1.2
1
0.8
0.6
0.4
0.2
0
wt
Δcls
murA
murB
murC
murD
murE
murF
ddlA
mraY
murG
murJ

**Figure S10**

**Figure S11. Construction of TyL1 and TyL2 strains.** The *murG* and its 5′ upstream DNA sequence (~1 kb) in *R. sphaeroides* wt or Δ*cls* genome are shown. In TyL1 or TyL2 genomes, a *gfp* gene is inserted between *murG* and its upstream sequence. The annealing sites and orientations of primers F1, R1, and R2 are indicated. These primers were used to amplify chromosomal DNA of *R. sphaeroides* wt (lane 2), TyL1 (lane 3), *R. sphaeroides* Δ*cls* (lane 4), or TyL2 (lane 5) by PCR. The PCR products were analyzed by agarose gel electrophoresis. DNA standards (in kb) are shown in lane 1.

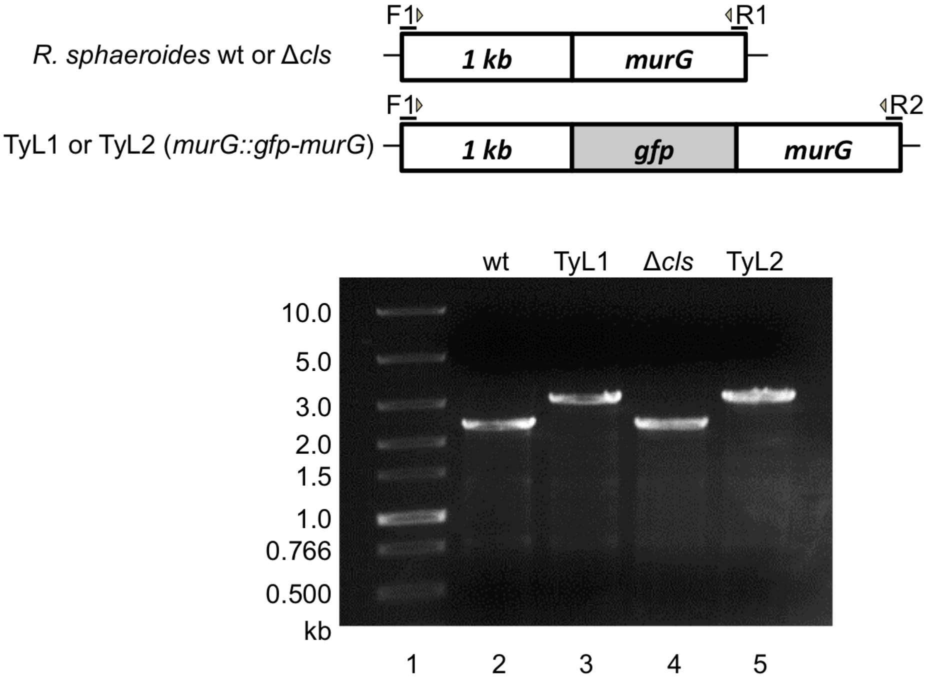
F1
R1
R. sphaeroides wt or Δcls
1 kb
murG
F1
R2
TyL1 or TyL2 (murG::gfp-murG)
1 kb
gfp
murG
wt
TyL1
Δcls
TyL2
10.0
5.0
3.0
2.0
1.5
1.0
0.766
0.500
kb
1
2
3
4
5

**Figure S11**

**Figure S12. MurG colocalizes with FtsZ in *R. sphaeroides*.** Representative micrographs of TyL1 cells expressing FtsZ-mCherry from the pIND plasmid without IPTG induction. Cells were grown to log phase (absorbance of 0.6, $\lambda$ = 600 nm) and imaged using phase and fluorescence microscopy.

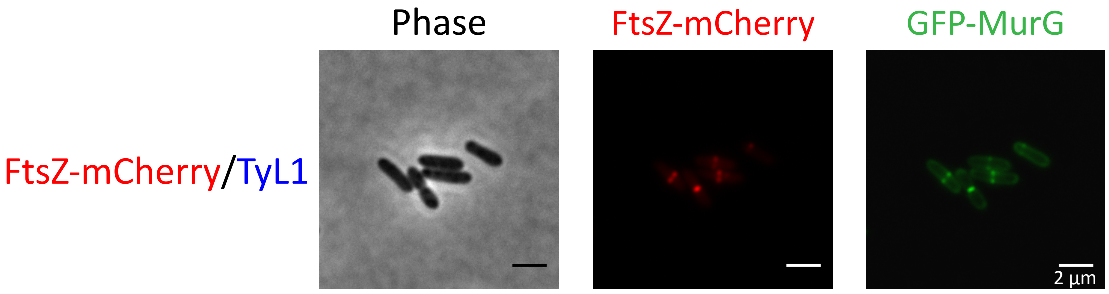

**Figure S12**

**Figure S13. Multiple sequence alignment of MurGs.** Amino acid sequences of MurG from *Staphylococcus aureus*, *E. coli* and *R. sphaeroides* are aligned using CLUSTAL O. Stars indicate conserved residues; colons indicate residues with similar size and hydropathy; periods indicate residues with similar size or hydropathy. Amino acids are highlighted: in red for residues involved in membrane binding, in magenta for residues involved in interaction with anionic phospholipids, and in yellow for residues involved in substrate binding. *E. coli* MurG contains a hydrophobic patch consisting of residues I74, L78, F81, W84, and W115, which is proposed to be the membrane association site. This membrane-binding patch is surrounded by several basic residues (K68, K71, R79, R85, R88, K139). Based on the alignment, we propose that *R. sphaeroides* MurG also contains a hydrophobic patch (A72, L76, A79, V82). Residues involved in murgocil binding are labeled with @ in blue above the sequences.

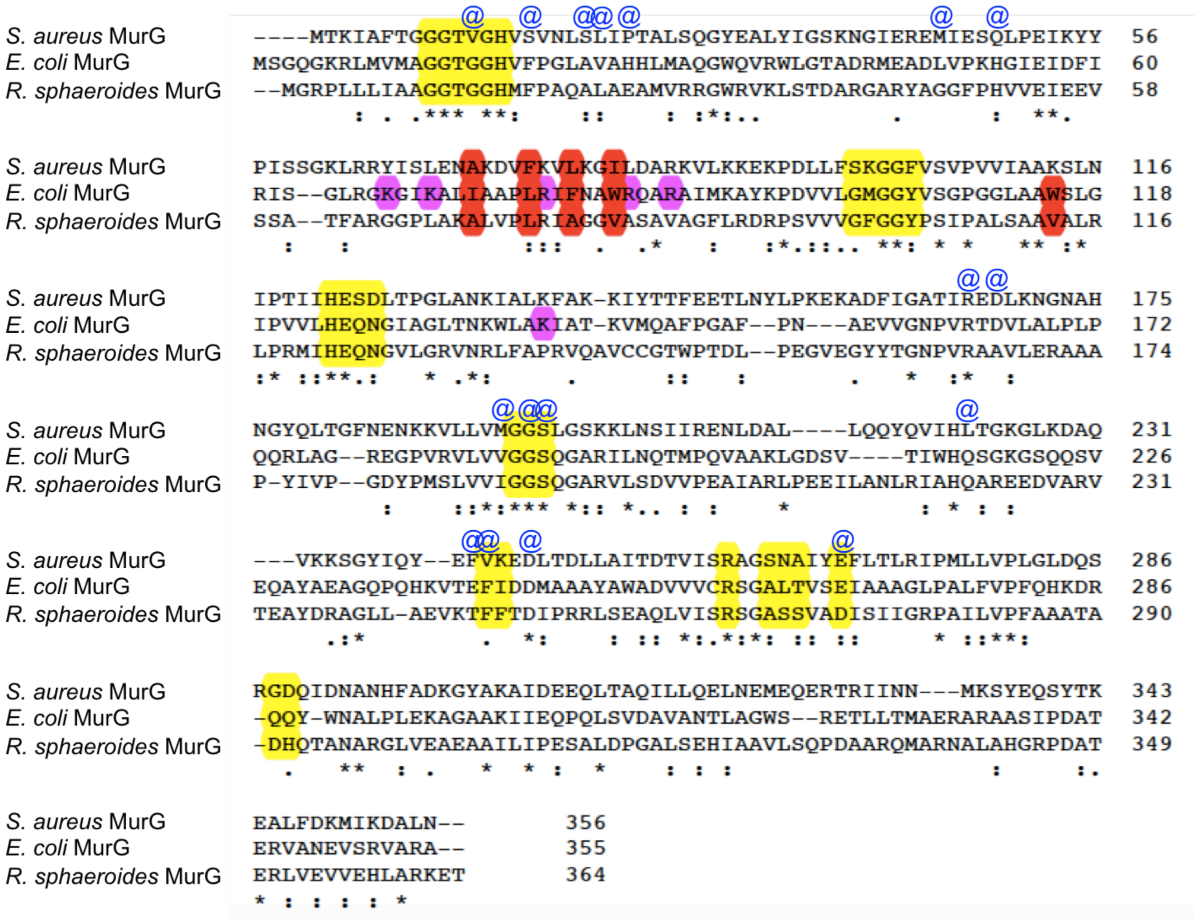

```
                                    @   @   @@ @                     @   @
S. aureus MurG       ----MTKIAFTGGGTVGHVSVNLSLIPTALSQGYEALYIGSKNGIEREMIESQLPEIKYY   56
E. coli MurG         MSGQGKRLMVMAGGTGGHVFPGLAVAHHLMAQGWQVRWLGTADRMEADLVPKHGIEIDFI   60
R. sphaeroides MurG  --MGRPLLLIAAGGTGGHMFPAQALAEAMVRRGWRVKLSTDARGARYAGGFPHVVEIEEV   58
                            : . .*** **:    ::    : :*:..         .      :  **.

S. aureus MurG       PISSGKLRRYISLENAKDVFKVLKGILDARKVLKKEKPDLLFSKGGFVSVPVVIAAKSLN   116
E. coli MurG         RIS--GLRGKGIKALIAAPLRIFNAWRQARAIMKAYKPDVVLGMGGYVSGPGGLAAWSLG   118
R. sphaeroides MurG  SSA--TFARGGPLAKALVPLRIAGGVASAVAGFLRDRPSVVVGFGGYPSIPALSAAVALR   116
                       :   :            :::  .  .*   :   :*.::.. **: * *   ** :*

                                                                       @ @
S. aureus MurG       IPTIIHESDLTPGLANKIALKFAK-KIYTTFEETLNYLPKEKADFIGATIREDLKNGNAH   175
E. coli MurG         IPVVLHEQNGIAGLTNKWLAKIAT-KVMQAFPGAF--PN---AEVVGNPVRTDVLALPLP   172
R. sphaeroides MurG  LPRMIHEQNGVLGRVNRLFAPRVQAVCCGTWPTDL--PEGVEGYYTGNPVRAAVLERAAA   174
                     :* ::**.:   * .*:     .      ::   :       .   *  :*  :

                                      @ @@                             @
S. aureus MurG       NGYQLTGFNENKKVLLVMGGSLGSKKLNSIIRENLDAL----LQQYQVIHLTGKGLKDAQ   231
E. coli MurG         QQRLAG--REGPVRVLVVGGSQGARILNQTMPQVAAKLGDSV----TIWHQSGKGSQQSV   226
R. sphaeroides MurG  P-YIVP--GDYPMSLVVIGGSQGARVLSDVVPEAIARLPEEILANLRIAHQAREEDVARV   231
                              :    ::*:*** *:: *.. : :    *         : * : :

                                    @@  @                     @
S. aureus MurG       ---VKKSGYIQY--EFVKEDLTDLLAITDTVISRAGSNAIYEFLTLRIPMLLVPLGLDQS   286
E. coli MurG         EQAYAEAGQPQHKVTEFIDDMAAAYAWADVVVCRSGALTVSEIAAAGLPALFVPFQHKDR   286
R. sphaeroides MurG  TEAYDRAGLL-AEVKTFFTDIPRRLSEAQLVISRSGASSVADISIIGRPAILVPFAAATA   290
                          .:*        .  *:    : :: *:.*:*: :: ::     * ::**:

S. aureus MurG       RGDQIDNANHFADKGYAKAIDEEQLTAQILLQELNEMEQERTRIINN---MKSYEQSYTK   343
E. coli MurG         -QQY-WNALPLEKAGAAKIIEQPQLSVDAVANTLAGWS--RETLLTMAERARAASIPDAT   342
R. sphaeroides MurG  -DHQTANARGLVEAEAAILIPESALDPGALSEHIAAVLSQPDAARQMARNALAHGRPDAT   349
                       .   **  : .   *  * :  *    : : :                  :     :.

S. aureus MurG       EALFDKMIKDALN--         356
E. coli MurG         ERVANEVSRVARA--         355
R. sphaeroides MurG  ERLVEVVEHLARKET         364
                     * : : : : *
```

**Figure S13**

**Figure S14. Inhibition of MurG decreases HADA incorporation into the existing PG of *S. aureus*.** (A) Quantification of HADA incorporation in *R. sphaeroides* wt, wt cells treated with FOS, and wt cells treated with DCS. Cells were grown in plain medium or medium containing the indicated small molecule inhibitors until early log phase (absorbance of 0.3, $\lambda = 600$ nm) and labeled with HADA. We measured the fluorescence emission of HADA and normalized the fluorescent signals by CFU. Each data point (mean value ± standard deviation) was obtained from three independent experiments. The concentrations of inhibitors used were FOS: 250 μg/ml; DCS: 0.05 μg/ml. (B) Quantification of HADA incorporation in *S. aureus* cells treated with murgocil or the solvent control DMSO. Cells were grown until log phase (absorbance of 0.6, $\lambda = 600$ nm) and treated with DMSO or murgocil at a final concentration of 20 μg/ml (10× MIC) for 20 min. Cells were then labeled with 0.24 mM HADA for another 20 min. We washed the cells with PBS to remove excess dye and measured the fluorescence emission of HADA at 405/450 nm. Each data point (mean value ± standard deviation) was obtained from three independent experiments.

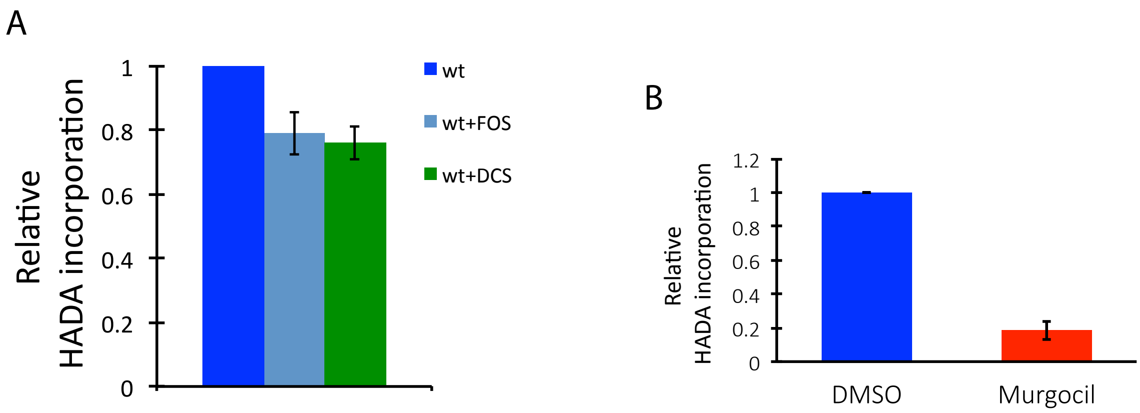
A
Relative
HADA incorporation
1
0.8
0.6
0.4
0.2
0
wt
wt+FOS
wt+DCS
B
Relative
HADA incorporation
1.2
1
0.8
0.6
0.4
0.2
0
DMSO
Murgocil

**Figure S14**

**Figure S15. Overexpression of MurG in *R. sphaeroides* cells at a high concentration causes cell filamentation and uneven cell division.** (A) Representative micrographs of *R. sphaeroides* wt cells expressing GFP-MurG from the pIND vector with the induction of 100 μM IPTG. *R. sphaeroides* wt cells expressing GFP and GFP-MurG from the pIND vector without IPTG induction are shown for comparison. (B) Representative micrographs of *R. sphaeroides* Δ*cls* cells expressing GFP-MurG from the pIND vector with the induction of 100 μM IPTG. *R. sphaeroides* Δ*cls* cells expressing GFP and GFP-MurG from the pIND vector without IPTG induction are shown for comparison.

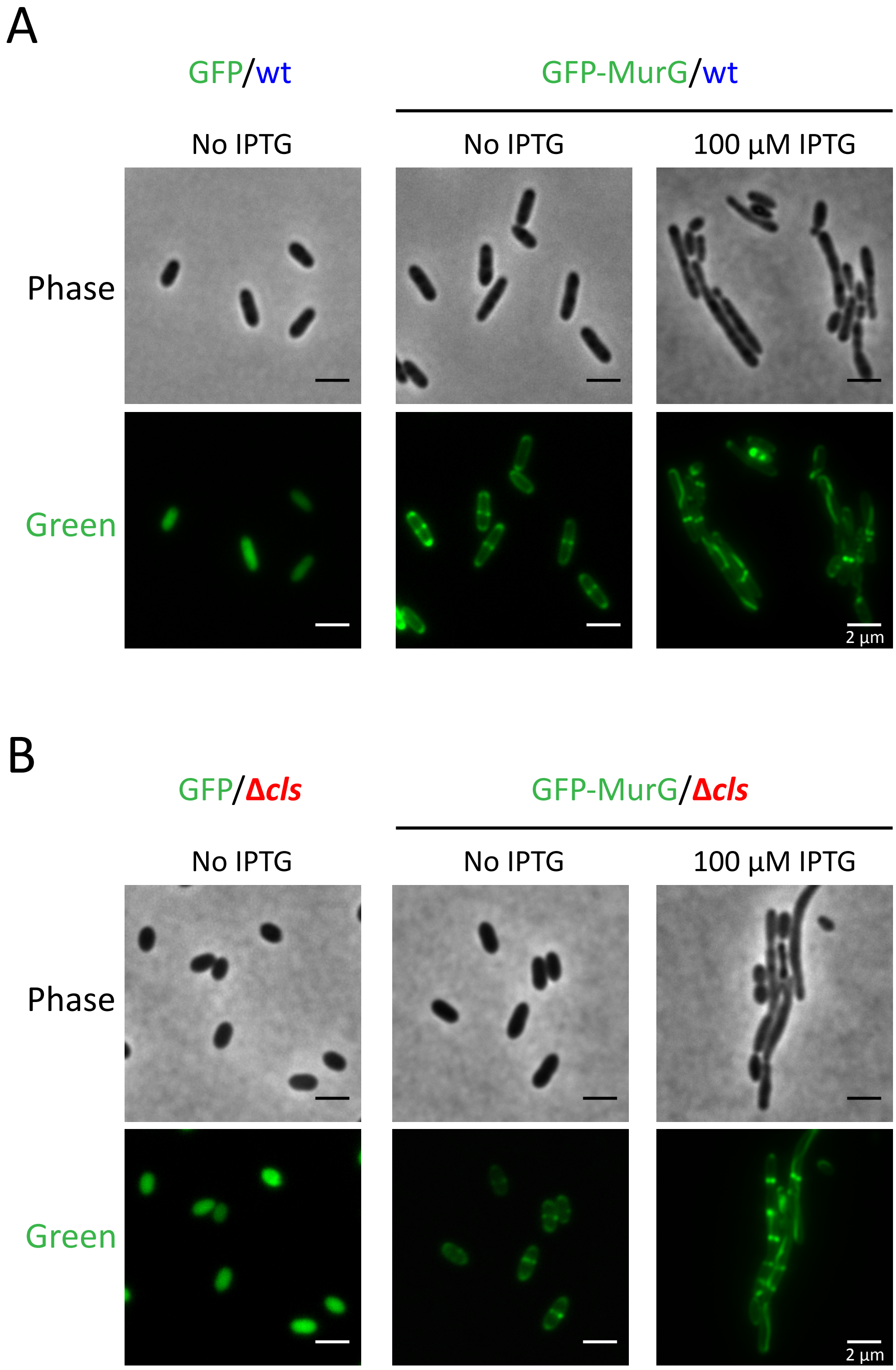
A
GFP/wt
GFP-MurG/wt
No IPTG
No IPTG
100 µM IPTG
Phase
Green
2 µm
B
GFP/Δcls
GFP-MurG/Δcls
No IPTG
No IPTG
100 µM IPTG
Phase
Green
2 µm

**Figure S15**

**Figure S16. CL deficiency does not affect MurG protein expression in *R. sphaeroides.*** TyL1 and TyL2 cell lysates that had the same amounts of proteins were subjected to Western blot analysis using a monoclonal antibody against GFP. The amount of MurG in cells was determined by quantifying the optical densitometry signal with ImageJ. Data represent mean values ± standard deviations obtained from three independent experiments.

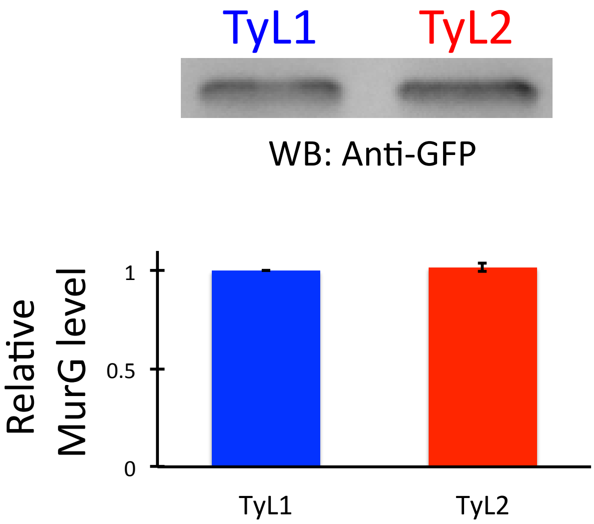

**Figure S16**

## Table S1. Bacterial strains and plasmids used in this study

| Strain or plasmid | Genotype or Description | Source or reference |
|---|---|---|
| ***E. coli* strains** | | |
| DH5α | *recA1 endA1 gyrA96 thi-1 hsdR17 supE44 relA1 deoR Δ(lacZYA-argF)U169 λ (ϕ80d lacZΔM15)* | Laboratory collection, CGSC#12384 |
| S17-1 | *recA pro hsdR* RP4-2-Tc::Mu-Km::Tn7 | |
| BL21(DE3) | Host strain for recombinant protein expression. | Laboratory collection |
| ***R. sphaeroides* strains** | | |
| 2.4.1 | Wild-type. | ATCC 17023 |
| *Δcls* | 2.4.1 containing a kanamycin resistance cassette in place of the genomic *cls.* | |
| TyL1 | 2.4.1 *murG::gfp-murG* | This study |
| TyL2 | *Δcls murG::gfp-murG* | This study |
| **Plasmids** | | |
| pIND5 | A derivative of pIND4 in which the NcoI site is replaced with an NdeI site. pIND4 is an IPTG-inducible expression vector for *R. sphaeroides*, kanamycin resistance. | |
| pIND5TetR | A variant of pIND5 with a tetracycline resistance cassette in place of the kanamycin resistance cassette. | This study |
| *gfp*-pIND5TetR | pIND5TetR containing *gfp.* | This study |
| *gfp-murG*-pIND5TetR | pIND5TetR containing *gfp-murG.* | This study |
| *gfp-murG*$^{L76E}$-pIND5TetR | pIND5TetR containing *gfp-murG*$^{L76E}$. | This study |
| pK18*mobsacB* | Suicide plasmid for allele exchange, kanamycin resistance. | |
| pK18*mobsacB*TetR | A variant of pK*18mobsacB* with a tetracycline resistance cassette in place of the kanamycin resistance cassette. | |
| 1k-*gfp-murG*-pK18*mobsacB*TetR | pK18*mobsacB*TetR containing *murG* and its 5′ upstream DNA sequence, with a *gfp* inserted in between. | This study |
| pET28b(+) | A vector for expression of proteins with an N-terminal His•Tag/thrombin/T7•Tag in the *E. coli* pET system. | Novagen |
| *murG*-pET28b(+) | pET28b(+) containing *murG.* | This study |
| *cls*-pIND5sp | pIND5sp containing *cls.* pIND5sp is a variant of pIND5 with a spectinomycin resistance cassette in place of the kanamycin resistance cassette. | |
| pET20b(+) | A vector for expression of proteins with a C-terminal His•Tag in the *E. coli* pET system. | Novagen |
| *mreB*-pET20b(+) | pET20b(+) containing *mreB.* | This study |
| *mreB*$^{\Delta N}$-pET20b(+) | pET20b(+) containing *mreB*$^{\Delta N}$. | This study |
| *mreBH1-gfp*-pIND5 | pIND5 containing *mreBH1-gfp. mreBH1* encodes the 1st to 9th amino acids of MreB (MreB helix 1). | This study |
| 2X*mreBH1-gfp*-pIND5 | pIND5 containing 2X*mreBH1-gfp.* 2X*mreBH1* denotes two copies of *mreBH1* arranged in tandem. | This study |
| *mreBH2-gfp*-pIND5 | pIND5 containing *mreBH2-gfp. mreBH2* encodes the 87th to 97th amino acids of MreB (MreB helix 2). | This study |
| 2X*mreBH2-gfp*-pIND5 | pIND5 containing 2X*mreBH2-gfp.* 2X*mreBH2* denotes two copies of *mreBH2* arranged in tandem. | This study |
| *mreBH1-H2-gfp*-pIND5 | pIND5 containing *mreBH1-H2-gfp. mreBH1-H2* denotes *mreBH1* and *mreBH2* arranged in tandem. | This study |
| *ftsZ-mCherry*-pIND5 | pIND5 containing *ftsZ-mCherry.* | This study |

## Table S2. Primers used in this study

| | |
|---|---|
| RF-TetR-F | TGCTTACATAAACAGTAATACAAGGGGTGTTATGAAACCCAACATACCCCTG |
| RF-TetR-R | GCCAGTGTTACAACCAATTAACCAATTCTGATCAGCGATCGGCTCGTTG |
| NdeI-*gfp*_p5 | GGAGAAATTAACATATGGTGAGCAAGGGCGAGGAG |
| BglII-*gfp*_p5 | GATGGTGATGAGATCTCTTGTACAGCTCGTCCAT |
| NdeI-*murG*_p5 | GGAGAAATTAACATATGGGCCGGCCGCTCCTCCTG |
| BglII-*murG*_p5 | GATGGTGATGAGATCTTGTCTCTTTCCTTGCCAG |
| *murG*-NdeI-*gfp* | AGCGGCCGGCCCATATGCTTGTACAGCTCGTCCAT |
| *murG*_L76E_S | GCCCGCGATGCGCTCGGGGACCAGCGC |
| *murG*_L76E_NS | GCGCTGGTCCCCGAGCGCATCGCGGGC |
| BamHI-*murG1k* | CGGTACCCGGGGATCCTCGACAAATGGTCGCTGA |
| HindIII-*murG1k* | GGCCAGTGCCAAGCTTTCATGTCTCTTTCCTTGC |
| *murG1k*+NdeI_S | GGGGCGGTGACCATATGGGCCGGCC |
| *murG1k*+NdeI_AS | GGCCGGCCCATATGGTCACCGCCCC |
| *murG1k*-NdeI-*gfp* | GGGGCGGTGACCATATGGTGAGCAAGGGCGAGGAG |
| NdeI-*murG*_p28 | CGCGCGGCAGCCATATGGGCCGGCCGCTCCTCCTG |
| XhoI-*murG*_p28 | GGTGGTGGTGCTCGAGTCATGTCTCTTTCCTTGC |
| NdeI-*mreB*_p20 | AAGGAGATATACATATGTCGTTTCTCACCGGCCTC |
| XhoI-*mreB*_p20 | GGTGGTGGTGCTCGAGGCTTTCGTAGTCGATCAC |
| NdeI-*mreB*$^{\Delta N}$_p20 | AAGGAGATATACATATGTCGGACATGGCCATCGAC |
| NdeI-*mreBH1* | TATGTCGTTTCTCACCGGCCTCTTCTCGA |
| BglII-*mreBH1* | GATCTCGAGAAGAGGCCGGTGAGAAACGACA |
| *mrebBH1*-BglII-*gfp* | CCTCTTCTCGAGATCTATGGTGAGCAAGGGCGAG |
| NdeI-2X*mreBH1* | TATGTCGTTTCTCACCGGCCTCTTCTCGATGTCGTTTCTCACCGGCCTCTTCTCGA |
| BglII-2X*mreBH1* | GATCTCGAGAAGAGGCCGGTGAGAAACGACATCGAGAAGAGGCCGGTGAGAAACGACA |
| NdeI-*mreBH2*-*gfp*_p5 | GGAGAAATTAACATATGATCAAGCACTTCATCCGCAAGGTGCACAAGATGGTGAGCAAGG |
| NdeI-*mreBH2*-F | AAGTGCTTGATCATATGCTTGTGCACCTTGCGGATGAAGTGCTTGATCATATGTTAATTT |
| NdeI-*mreBH2*-R | AAATTAACATATGATCAAGCACTTCATCCGCAAGGTGCACAAGCATATGATCAAGCACTT |
| NdeI-*mreBH1*-F | AAATTAACATATGTCGTTTCTCACCGGCCTCTTCTCGCATATGATCAAGCACTT |
| NdeI-*mreBH1*-R | AAGTGCTTGATCATATGCGAGAAGAGGCCGGTGAGAAACGACATATGTTAATTT |
| NdeI-*ftsZ*_p5 | GGAGAAATTAACATATG GCACTCAACCTCATGATG |
| BglII-*ftsZ*_p5 | GATGGTGATGAGATCT GTTTGCCTGACGCCGCAG |
| BglII-*mCherry*_p5 | GATGGTGATGAGATCTCTTGTACAGCTCGTCCAT |
| *ftsZ*-BglII-*mCherry* | TCAGGCAAACAGATCTATGGTGAGCAAGGGCGAG |
| WSG | AGATGGTCTATGGCTCCA |

## Table S3. qPCR primers used in this study

| Gene | Primer type | Sequence |
|---|---|---|
| *rpoZ* | Forward | TGACAAGAACCCTGTCGTG |
| | Reverse | GCAGCTTCTCTTCGGACAT |
| *mreB* | Forward | CTTCTTGCCGTCCTTCACA |
| | Reverse | CGCGAACACGCTGATCTA |
| *mreC* | Forward | CTTCCTTCCAGGCCTTCATC |
| | Reverse | TCGAGAACTTCCAGTCCTACA |
| *mreD* | Forward | CACATGCGTCTCCCGAAG |
| | Reverse | CCATCCTCTGCTATCCTCTGAT |
| *pbp2* | Forward | GATGACGACGCGGTAATTCT |
| | Reverse | ATCAACATCCGGCTGATCC |
| *rodA* | Forward | GTTCACCGCGAGATAGAAGAAG |
| | Reverse | CTCGCTTCTGGTGCTCTATG |
| *pbp1A* | Forward | CGTCATGAAGCTCTGGAACA |
| | Reverse | CGTCTGGTTCATCGGCTATAC |
| *murA* | Forward | CTTCCGCACGATGTCGTAAT |
| | Reverse | CACGATGACGCAGCTTCT |
| *murB* | Forward | GCATTCCAACTTCCTCATCAAC |
| | Reverse | CCGCATGATTTCCCACTCTA |
| *murC* | Forward | GCAAGACCACGACCACTAC |
| | Reverse | GAGCCATAGGCATGGATCAC |
| *murD* | Forward | CAATGACATCGGCCTCTTCT |
| | Reverse | CGACAGGATGTGATGGATGAG |
| *murE* | Forward | CGCATCGTCGTCGTCTTC |
| | Reverse | GATTGTCGTCGGTGACATAGAG |
| *murF* | Forward | AAGACCTCGACCAAGGAGA |
| | Reverse | CCCAGTGGTTGTTGTAGGAG |
| *ddlA* | Forward | CTCTTCGGTAGGCGTCTATATC |
| | Reverse | GACATAGGTCTCGACCATCAG |
| *mraY* | Forward | GCTCGACAATCCTTACGTCTG |
| | Reverse | CCCTTGGTGTTCTGCTTCTT |
| *murG* | Forward | ACCTTCTTCACCGACATTCC |
| | Reverse | CGGCCGATGATCGAGATG |
| *murJ* | Forward | CTCATGACCTTCCAGCTTCTT |
| | Reverse | ATGTTCCGCCGCTTCTT |

**Table S4. Muropeptides analyzed by UPLC-MS in positive ion mode.**

| Peak | Retention time (min) | Calculated mass | Observed m/z | Length of the stem peptides |
|---|---|---|---|---|
| 1 | 7.6 | 870.37 | 871.37 (+1) | Tri |
| 2 | 9 | 698.29 | 699.29 (+1) | Di |
| 3 | 12 | 941.41 | 942.41 (+1) | Tetra |
| 4a | 13.7 | 1722.71 | 575.23 (+3) | Tri-Tri |
| 4b | 20.3 | 1722.71 | 862.35 (+2) | Tri-Tri |
| 5a | 21.7 | 1793.77 | 897.88 (+2) | Tri-Tetra |
| 5b | 22.8 | 1793.77 | 897.88 (+2) | Tri-Tetra |
| 6 | 24.1 | 1864.81 | 933.40 (+2) | Tetra-Tetra |
| 7a | 28 | 2717.15 | 906.71 (+3) | Tri-Tetra-Tetra |
| 7b | 29.2 | 2717.15 | 906.71 (+3) | Tri-Tetra-Tetra |
| 8 | 30.1 | 2788.21 | 930.40 (+3) | Tetra-Tetra-Tetra |
| 9a | 30.7 | 1773.74 | 887.87 (+2) | anhydro Tri-Tetra |
| 9b | 31.9 | 1773.74 | 887.87 (+2) | anhydro Tri-Tetra |
| 10 | 33.2 | 1844.77 | 923.38 (+2) | anhydro Tetra-Tetra |

# CHAPTER 4

## MreB mutations enhance recombinant protein production in *Escherichia coli* cells

This chapter was adapted from:

Ti-Yu Lin, William S. Gross, Landen A. Nickel, Kerwyn Casey Huang,
Douglas B. Weibel

Manuscript in Preparation

## ABSTRACT

*Escherichia coli* has been a mainstay for engineering and producing recombinant proteins for applications in research and the biotech industry. Here, we describe a method for increasing recombinant protein production by leveraging mutations in the bacterial MreB that increase *E. coli* cell size without affecting growth rates. The A53T mutant in *E. coli* MreB (MreB$^{A53T}$) has a cell volume 50% larger than cells of the wild-type strain that we hypothesized would provide additional space to accommodate recombinant proteins. We overexpressed soluble (GFP and human carbonic anhydrase II) or insoluble proteins (human IGF-1) in *E. coli* MreB$^{A53T}$ cells using a common expression protocol incorporating a high-copy number plasmid containing the target gene controlled by the *lac* promoter, and observed mutants producing 30-40% more protein per unit time than the wild-type strain. This approach for increasing protein production can be extended to a range of bacterial strains used for recombinant protein production.

# INTRODUCTION

Recombinant protein production has revolutionized biochemical research and the biotech industry. Insulin was the first recombinant protein to enter the market in the early 1980s, and by 2016 more than 90 recombinant biologics were FDA-approved and commercially available (1). Recombinant expression has been widely used to engineer and produce proteins for applications that extend beyond research and the pharmaceutical industry, and include proteins in health care products, enzymes for consumer products, and antibodies and antibody fragments incorporated into diagnostic tests and devices. Driven by the exponential increase in the number of protein structures entered into the Protein Data Bank (PDB) since the early 1970s, by 2017 there were >112,000 proteins that had been produced recombinantly and purified for crystallization.

Recombinant protein expression entails cloning gene(s) encoding a protein, inserting the genes into a host cell line (either incorporated into the chromosome or plasmid DNA), inducing protein production (typically using a small molecule to activate transcription), lysing host cells to release proteins, and isolating and purifying the target protein. A variety of different cell lines are used for protein expression (e.g., bacterial, fungal, insect, and algal), however bacteria have been the most widely used host and are generally used for making proteins that do not require post-translational modifications. Several factors influence recombinant protein yields, including: 1) the capacity of cells to produce proteins (which we refer to as the ‘carrying capacity’); 2) cell growth rates; 3) the concentration of cells achieved in culture before growth is inhibited by nutrient limitations, accumulation of metabolic waste, or the presence of high concentrations of intracellular protein; and 4) the process of recovering and purifying protein from cell cultures. Recombinant protein expression can induce a cellular stress response, reduce bacterial cell growth, and result in low protein yields (2). Switching hosts provides a viable mechanism to transcend this barrier and *Escherichia coli* and other fast-growing bacteria are often used to produce proteins as they are among the fastest growing bacteria (doubling time as fast as 20 min) and can reach a high cell density in liquid cultures (titers as high as $1 \times 10^{10}$ cells/mL) (3, 4).

In addition to switching to different hosts, several other approaches are commonly used to optimize protein production, including screening nutrient and growth conditions to enhance growth rates and cell densities. A key advance in this area has been the wealth of physiological and genetic information available for *E. coli*, which has stimulated the development of molecular tools (e.g., plasmids) and engineered strains (e.g., containing chaperones or viral promoters) for improving yields of proteins. An interesting, yet largely untested approach to increasing protein production is to engineer the shape and volume of bacterial cells to tap into a larger volume to produce and store increased amounts or concentrations of recombinant proteins or other molecules. One example of this approach has entailed inhibiting *E. coli* cell division to produce filamentous cells that increase the intracellular volume for the storage of polyhydroxyalkanoates (5, 6). However, filamentous cells grow more slowly than vegetative cells, do not produce higher concentrations of recombinant proteins, and are prone to lysis, which limits their applications (7).

The spatial assembly of the peptidoglycan layer of the cell wall controls cell shape in many bacteria; recent evidence highlights the role of the bacterial homolog of eukaryotic actin, MreB in this process. MreB binds the cell membrane and short filaments of polymerized MreB that are oriented approximately parallel to the short axis of the cell move around the circumference of rod-shaped cells; the paths of these protein filaments are hypothesized to correlate to the synthesis of newly synthesized peptidoglycan. Current evidence suggests that these filaments may recruit the cell wall synthesis complex and direct the assembly of the rigid peptidoglycan layer of the cell wall, thereby assembling the material that defines cell shape (8, 9).

Several point mutations in MreB increase the width of rod-shaped *E. coli* cells through unknown mechanisms,(10) including the *E. coli* $\mathrm{MreB}^{\mathrm{A53T}}$ point mutant, which has a decrease in cell length ($x_{\mathrm{length}}$ = 3.1 μm) and an increase in cell width ($x_{\mathrm{width}}$ = 1.3 μm) compared to the wild-type ($\mathrm{MreB}^{\mathrm{WT}}$) strain ($x_{\mathrm{length}}$ = 3.5 μm, $x_{\mathrm{width}}$ = 1.0 μm) when grown in lysogeny broth (LB); cells of *E. coli* $\mathrm{MreB}^{\mathrm{A53T}}$ are 50% larger in volume than the *E. coli* $\mathrm{MreB}^{\mathrm{WT}}$ strain. We also found that compared to $\mathrm{MreB}^{\mathrm{WT}}$ cells, $\mathrm{MreB}^{\mathrm{A53T}}$ cells produced 70% more ATP that can be used for protein production (Figure 1A). As the amount of DNA in $\mathrm{MreB}^{\mathrm{A53T}}$ is unchanged,(10) we hypothesized that cells of the point mutant may have an increased carrying capacity for biomolecules. We anticipated that the increase in production would arise from an increase in cell volume, and that an increase in intracellular space devoid of the chromosome (e.g., at the cell poles) may enable MreB$^{A53T}$ cells to tolerate higher concentrations of recombinant proteins (Figure 1B).

We were particularly interested in exploiting the increase in cell width to expand the volume of the polar region of rod-shaped bacteria, as cells often use this space to store large amounts of expressed proteins packaged into insoluble aggregates referred to as inclusion bodies. Inclusion bodies are a convenient format for producing expressed proteins at scale, as protein packaged into inclusion bodies can be easily separated from other cellular materials and refolded into active protein.

In this study, we tested our hypothesis using *E. coli* MreB$^{A53T}$ and three target proteins: 1) green fluorescent protein (GFP, a soluble protein that is highly tolerated by *E. coli* during overexpression); 2) human carbonic anhydrase II (HCAII, a protein that is well tolerated by *E. coli* during overexpression); and 3) human insulin-like growth factor (IGF-1; an important therapeutic human protein that is packaged into inclusion bodies in *E. coli* cells during overexpression). Using a commonly used recombinant expression system based on a high-copy number plasmid containing either the genes coding for GFP, HCAII, or IGF-1 under control of the *lac* promoter, we demonstrate that altering bacterial cell shape and volume improves yields of recombinant proteins.

# RESULTS AND DISCUSSION

## MreB$^{A53T}$ does not affect cell growth in nutrient-rich liquid media.

The *E. coli* MreB$^{A53T}$ mutant has a lag-phase growth advantage (a 0.8 h reduction in lag time compared with the MreB$^{WT}$ strain) when growing in Davis minimal (DM) medium supplemented with glucose (10). To investigate if the *E. coli* MreB$^{A53T}$ mutant maintains this growth advantage when growing in nutrient-rich liquid media in which recombinant protein production is generally performed, we grew the cells in LB nutrient media and measured their growth curves. Figure 1C demonstrates no significant difference in growth between *E. coli* MreB$^{WT}$ and MreB$^{A53T}$ strains, suggesting that the lag-phase growth advantage conferred by the MreB A53T mutation in minimal media is highly dependent on growth conditions such as nutrient composition and concentration.

## *E. coli* MreB$^{A53T}$ enhances the yield of GFP produced in *E. coli* cells.

We used GFP (26.9 kDa; containing 238 amino acids) for initial experiments, in which we expressed it from a high-copy number plasmid (*gfp*-pIND5) under control of the *lac* promoter in both MreB$^{WT}$ and MreB$^{A53T}$ cells. The pIND vector has been used to achieve a high expression level of recombinant proteins in *E. coli* (11, 12). We grew cells in LB nutrient media and tracked cell growth by measuring the absorbance of cell cultures at a wavelength of 600 nm ($OD_{600}$) at 1 h intervals. *E. coli* MreB$^{A53T}$ entered log phase ~0.5 h earlier than the MreB$^{WT}$ strain (Figure 2A). 3 h after starting cultures, both strains were in log phase ($OD_{600}$ of ~0.5 for $MreB^{WT}$; $OD_{600}$ of ~0.7 for $MreB^{A53T}$), and we induced protein expression by adding isopropyl-β-D-thiogalactopyranoside (IPTG; to a concentration of 1 mM) and continued growing cells until they reached early stationary phase ($OD_{600}$ of ~1.8 for both strains).

We found that the expression of GFP reduced cell size of both *E. coli* strains [between induction and 3 h of incubation, the volume of $MreB^{WT}$ and $MreB^{A53T}$ decreased from 2.3 to 1 $\mu m^3$ and 3.5 to 2 $\mu m^3$, respectively] and produced diffuse fluorescence ($\lambda_{em}$=512 nm) throughout the cytoplasm (Figure 2B, S2). Occasionally, GFP misfolded, aggregated, and formed inclusion bodies in a small number of cells that was visible by phase contrast microscopy. To compare GFP expression levels in cells of the two *E. coli* strains, we performed Western blot analyses on cell lysates prepared from the same volume of cell cultures. We found that the $MreB^{A53T}$ mutant produced more GFP than the $MreB^{WT}$ strain at each time point after IPTG induction: 35% more at 1 h, 28% more at 2 h, and 43% more at 3 h (Figure 2C, D).

### $MreB^{A53T}$ enhances the yield of HCAII produced in *E. coli* cells.

HCAII is a 29.2 kDa metalloenzyme containing 260 amino acids that catalyzes the interconversion of carbon dioxide and water to bicarbonate and a proton, and an important drug target and model system for drug development (13). We expressed HCAII from *hcaii*-pIND5 in both *E. coli* $MreB^{WT}$ and $MreB^{A53T}$ cells, grew cells in LB media, and tracked their growth. *E. coli* $MreB^{A53T}$ entered log phase earlier (~0.25 h) than the $MreB^{WT}$ strain (Figure 3A). 3 h after starting cultures, both strains were in log phase ($OD_{600}$ ~0.4 for $MreB^{WT}$; $OD_{600}$ ~0.5 for $MreB^{A53T}$); we induced expression of HCAII using IPTG (1 mM) and grew cells until they reached early stationary phase ($OD_{600}$ ~1.5 for $MreB^{WT}$; $OD_{600}$ ~1.7 for $MreB^{A53T}$). Expression of HCAII reduced the cell size of both *E. coli* strains and did not induce inclusion body formation, which confirmed cytoplasmic HCAII was soluble (Figure 3B, S3). We performed Western blot analyses on cell lysates prepared from the same volume of cell cultures and found that *E. coli* $MreB^{A53T}$ produced more HCAII than $MreB^{WT}$ at each time point after IPTG induction: 69% more at 1 h, 39% more at 2 h, and 30% more at 3 h (Figure 3C, D). We found no significant difference between the enzyme activities of the HCAII purified from *E. coli* $MreB^{WT}$ and $MreB^{A53T}$ cells (Figure S4).

### ***E. coli*** $MreB^{A53T}$ **enhances the yield of human insulin-like growth factor, IGF-1.**

IGF-1 is a 7.7 kDa protein containing 70 amino acids produced by the liver that is structurally similar to insulin, yet plays a very different role in the human body. IGF-1 is secreted throughout life, plays a key role in childhood growth, and continues to have anabolic effects in adults. A recombinant version of IGF-1 is approved for the treatment of growth failure in humans and is commercially manufactured in *E. coli* and yeast cells (14). *E. coli* cells expressing recombinant IGF-1 package the protein into inclusion bodies (7). To examine if our approach to enhancing protein expression in bacteria is applicable to proteins that are insoluble after production in cells, we performed the same protein expression protocol on IGF-1 that we used for GFP and HCAII. *E. coli* $MreB^{A53T}$ entered log phase earlier (~1 h) than MreB$^{WT}$ cells (Figure 4A) and displayed a growth profile similar to the *E. coli* strains expressing GFP (Figure 2A). After 4 h of growth (OD$_{600}$ ~0.4 for MreB$^{WT}$; OD$_{600}$ ~0.7 for MreB$^{A53T}$), we induced protein expression using IPTG and continued growing the cells until they reached early stationary phase (OD$_{600}$ ~1.7 for MreB$^{WT}$; OD$_{600}$ ~1.8 for MreB$^{A53T}$). Expression of IGF-1 induced inclusion body formation and reduced the cell size of both *E. coli* strains (Figure 4B, S5). We noticed that the inclusion bodies at the poles of MreB$^{A53T}$ cells were noticeably larger than those in MreB$^{WT}$ cells. Using Western blot analyses, we found that MreB$^{A53T}$ cells produced more IGF-1 than the MreB$^{WT}$ strain at each time point after IPTG induction: 137% more at 1 h, 89% more at 2 h, 41% more at 3 h, and 41% more at 4 h (Figure 4C, D).

In conclusion, we tested whether *E. coli* cells engineered with an increased cell volume (yet no reduction in cell growth) could increase yields of expressed soluble (e.g., GFP and HCAII) or insoluble (e.g., IGF-1) recombinant proteins. We found an enhancement of all the three proteins of 30-40% per unit time in *E. coli* strain REL606 incorporating MreB$^{A53T}$ compared to the MreB$^{WT}$ strain. REL606 is a derivative of *E. coil* B strain, which was a predecessor of the commonly used expression strain BL21 (15). We anticipate that this approach will work with other proteins and *E. coli* strains.

MreB$^{A53T}$ has a short lag time—compared to MreB$^{WT}$—when grown in minimal nutrient media supplemented with glucose (10). We did not observe a significant difference in growth between the two strains in LB media; however, MreB$^{A53T}$ cells entered log phase earlier than MreB$^{WT}$ cells when containing recombinant plasmids, suggesting that protein expression can be induced earlier when using the $\mathrm{MreB}^{\mathrm{A53T}}$ mutant. We determined a colony-forming unit (CFU) count for each strain at 1 h and 3 h (or 4 h for IGF-1) after IPTG induction (Table S1, S2, S3) and used these values to determine the relative amount of protein produced per cell and per unit volume for both $\mathrm{MreB}^{\mathrm{A53T}}$ and $\mathrm{MreB}^{\mathrm{WT}}$ cells. For each of the three proteins studied, we found that 1 h after IPTG induction, the $\mathrm{MreB}^{\mathrm{A53T}}$ mutant produced ~86% more protein per cell and ~7% more protein per unit volume than the $\mathrm{MreB}^{\mathrm{WT}}$ strain. 3 h (or 4 h for IGF-1) after IPTG induction, the $\mathrm{MreB}^{\mathrm{A53T}}$ mutant produced ~137% more protein per cell and ~16% more protein per unit volume than the $\mathrm{MreB}^{\mathrm{WT}}$ strain (Figure 5). These results suggest that the $\mathrm{MreB}^{\mathrm{A53T}}$ mutant has a higher protein carrying capacity compared to the wild-type strain. The molecular mechanisms by which a point mutation in MreB increases cell size and protein production require further research.

A variety of other materials have also been expressed in bacterial hosts, including: biopolymers, nucleic acids, and small molecules (16, 17). In principle, our approach can be applied to a range of different overexpression strains of bacteria that are used for the production of proteins, enzymes, biomaterials, and small molecules that are all derived from genetically encoded pathways. A collection of MreB point mutations in *E. coli* that produce cells with large volumes (10) enables different mutations to be screened and tested to determine which are best tolerated by host strains of bacteria and which produce the highest yields of protein.

## EXPERIMENTAL PROCEDURES

### Bacterial strains and growth conditions.

*E. coli* strains were grown in LB nutrient broth at 37°C with shaking at 200 rpm. When required, kanamycin (25 μg/mL) was added to nutrient media. For growth curves, cell cultures in stationary phase (overnight cultures) were diluted 100x into LB media. The absorbance ($\lambda = 600$ nm) of cell cultures was measured at the time points indicated. To measure ATP production, cells were grown to log phase (absorbance of 0.4-0.7; $\lambda = 600$ nm) and subjected to BacTiter-Glo™ Microbial Cell Viability Assay (Promega) in accordance with the user manual. To induce protein expression, IPTG was added into cultures (to a final concentration of 1 mM) when cultures reached log phase (absorbance of 0.4-0.7; $\lambda = 600$ nm). Bacterial strains and plasmids used in this study are summarized in Table 1.

### Plasmid construction.

*gfp*, *hcaii*, and *igf-1* were amplified by PCR and cloned into pIND5 at the NdeI and BglII sites by In-Fusion Cloning (Clontech) in accordance with the user manual. The primers used for amplifying the three genes are listed in Table S4. The three target proteins contained a C-terminal RSHHHHHH sequence translationally fused from the pIND5 vector.

### Imaging.

A droplet containing a suspension of cells was dropped onto a 2% agarose (w/v) pad prepared in phosphate-buffered saline (PBS) buffer (137 mM NaCl, 2.7 mM KCl, 10 mM $Na_2HPO_4$, and 1.76 mM$KH_2PO_4$, pH 7.4), covered with a glass coverslip, and imaged with an inverted Nikon Eclipse Ti microscope equipped with a Photometrics CoolSNAP HQ2 charge-coupled-device (CCD) camera and a 120 W mercury arc lamp (X-cite Series 120, EXFO). We acquired phase contrast images with a 100× objective (Nikon Plan Apo 100×/1.40 oil Ph3 DM) and the Nikon Instruments Software (NIS)-Elements Advanced Research (AR) microscope imaging software program (Version 4.000.07).

**Western blot analysis.**

We collected an identical volume of cell cultures, lysed cells by boiling in protein SDS (sodium dodecyl sulfate) sample buffer, analyzed the soluble fraction using SDS-PAGE, and transferred proteins to nitrocellulose membranes using blots. Membranes were incubated in PBST blocking buffer (PBS buffer containing 5% bovine serum albumin and 0.1% Tween 20) for 1 h at 25 °C and probed with a monoclonal horseradish peroxidase (HRP)-conjugated anti-GFP antibody (Santa Cruz Biotechnology, CA) or a monoclonal HRP conjugated anti-6X His tag antibody (Santa Cruz Biotechnology, CA) at a 1:5000 dilution in PBST at 25 °C for 1 h. Unbound antibody was removed by extensive washes with PBST. The antibody-reacted proteins were visualized by chemiluminescence using ECL Western blotting detection reagents. Quantitation of protein expression levels was performed with ImageJ.

# ACKNOWLEDGMENTS

T.-Y. Lin acknowledges a William R. & Dorothy E. Sullivan Wisconsin Distinguished Graduate Fellowship and a Dr. James Chieh-Hsia Mao Wisconsin Distinguished Graduate Fellowship from the Department of Biochemistry, University of Wisconsin-Madison. The National Science Foundation (DMR-1121288), the Human Frontiers Science Program (RGY0076/2013), and Gordon and Betty Moore Foundation (5263 04) supported this research.

**Figure 1. The MreB$^{A53T}$ mutation enlarges cell volume and does not affect cell growth in nutrient-rich growth media.** (A) Images depicting the morphology of MreB$^{WT}$ and MreB$^{A53T}$ cells at log phase (absorbance of ~0.6, $\lambda$ = 600 nm). The table below the panel shows the cell shape parameters of the two strains. Each data point (mean value ± standard deviation) was determined by imaging 200 cells by phase-contrast bright-field microscopy and using ImageJ to determine cell width and length by which cell volume was calculated (see Figure S1 for details). ATP production was measured by BacTiter-Glo™ assay. Luminescent signal was normalized to CFU to obtain ATP level per cell. Mean values ± standard deviations obtained from three independent experiments are shown. (B) Schematic illustration of the hypothesis tested. *E. coli* MreB$^{A53T}$ cells have an increase in cell volume that provides additional space for the storage of recombinant proteins as either soluble or insoluble (inclusion body) form. (C) Growth curves of the MreB$^{WT}$ and MreB$^{A53T}$ strains. Cells were grown in 96-well plates at 37°C in LB media and absorbance ($\lambda$ = 600 nm) measured using a Tecan infinite M200 Pro microplate reader. Shown are mean values ± standard deviations obtained from three independent experiments.

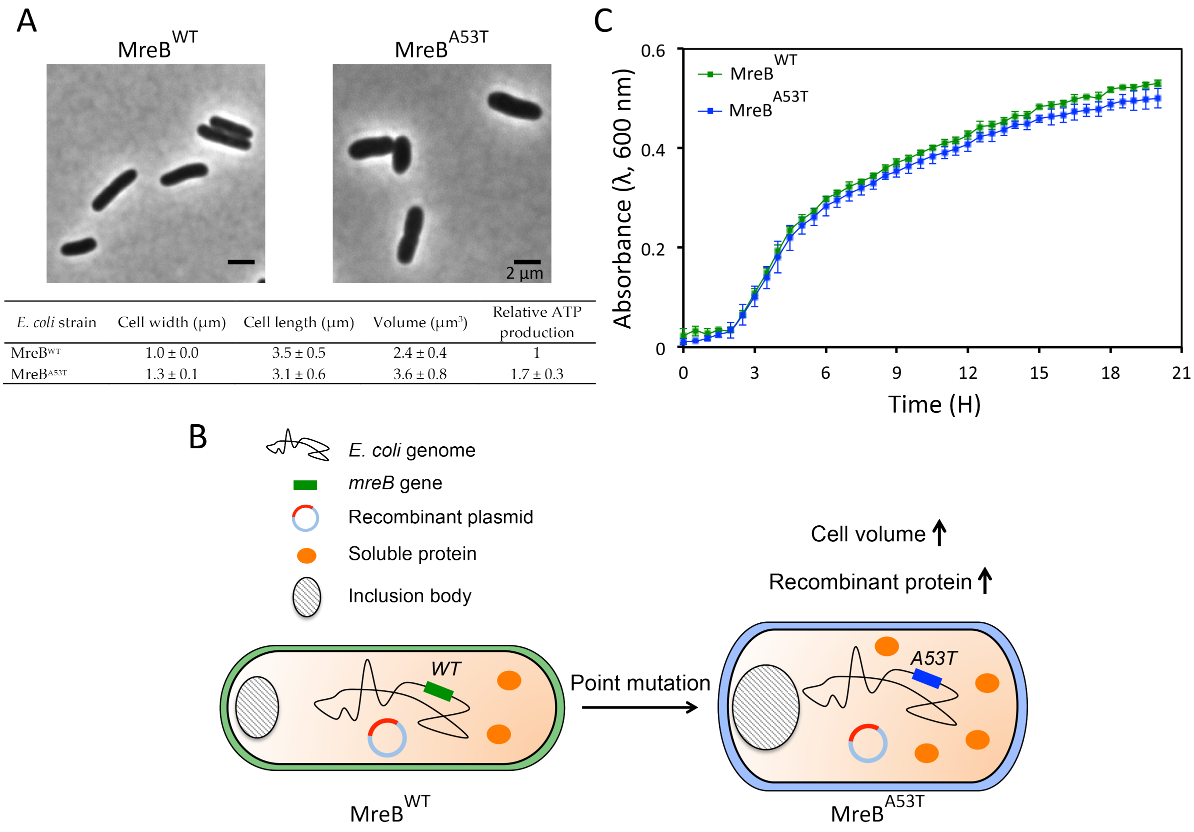

| *E. coli* strain | Cell width (µm) | Cell length (µm) | Volume (µm$^3$) | Relative ATP production |
|---|---|---|---|---|
| MreB$^{WT}$ | 1.0 ± 0.0 | 3.5 ± 0.5 | 2.4 ± 0.4 | 1 |
| MreB$^{A53T}$ | 1.3 ± 0.1 | 3.1 ± 0.6 | 3.6 ± 0.8 | 1.7 ± 0.3 |

**Figure 1**

**Figure 2. MreB$^{A53T}$ enhances GFP production in *E. coli* cells.** (A) Growth curves of MreB$^{WT}$ and MreB$^{A53T}$ cells expressing GFP from *gfp*-pIND5. Cells were grown in nutrient LB media in test tubes at 37°C with shaking. IPTG at a final concentration of 1 mM was added into the cultures when they reached log phase (absorbance of ~0.5 for MreB$^{WT}$; ~0.7 for MreB$^{A53T}$, $\lambda = 600$ nm). Mean values ± standard deviations obtained from three independent experiments are shown. (B) Images depict the morphology of MreB$^{WT}$ and MreB$^{A53T}$ cells expressing GFP from *gfp*-pIND5 before IPTG induction (upper panel) and after IPTG induction for 3 h (lower panel). Arrows indicate inclusion bodies in which GFP was misfolded and not fluorescent. (C&D) GFP expression in cells before IPTG induction at hour 3 and after IPTG induction at hourly time points was verified by Western blot (WB) analysis using an anti-GFP antibody. GFP expression levels were determined by quantifying the optical densitometry signal with ImageJ. GFP expression at each time point was normalized for wild-type cells after IPTG induction for 1 h. Mean values ± standard deviations obtained from three independent experiments are shown. We analyzed the difference between the GFP expression levels of the two strains at each time point using the Student's *t* test (two-tailed, paired). $^{*}P < 0.05$. $^{**}P < 0.01$.

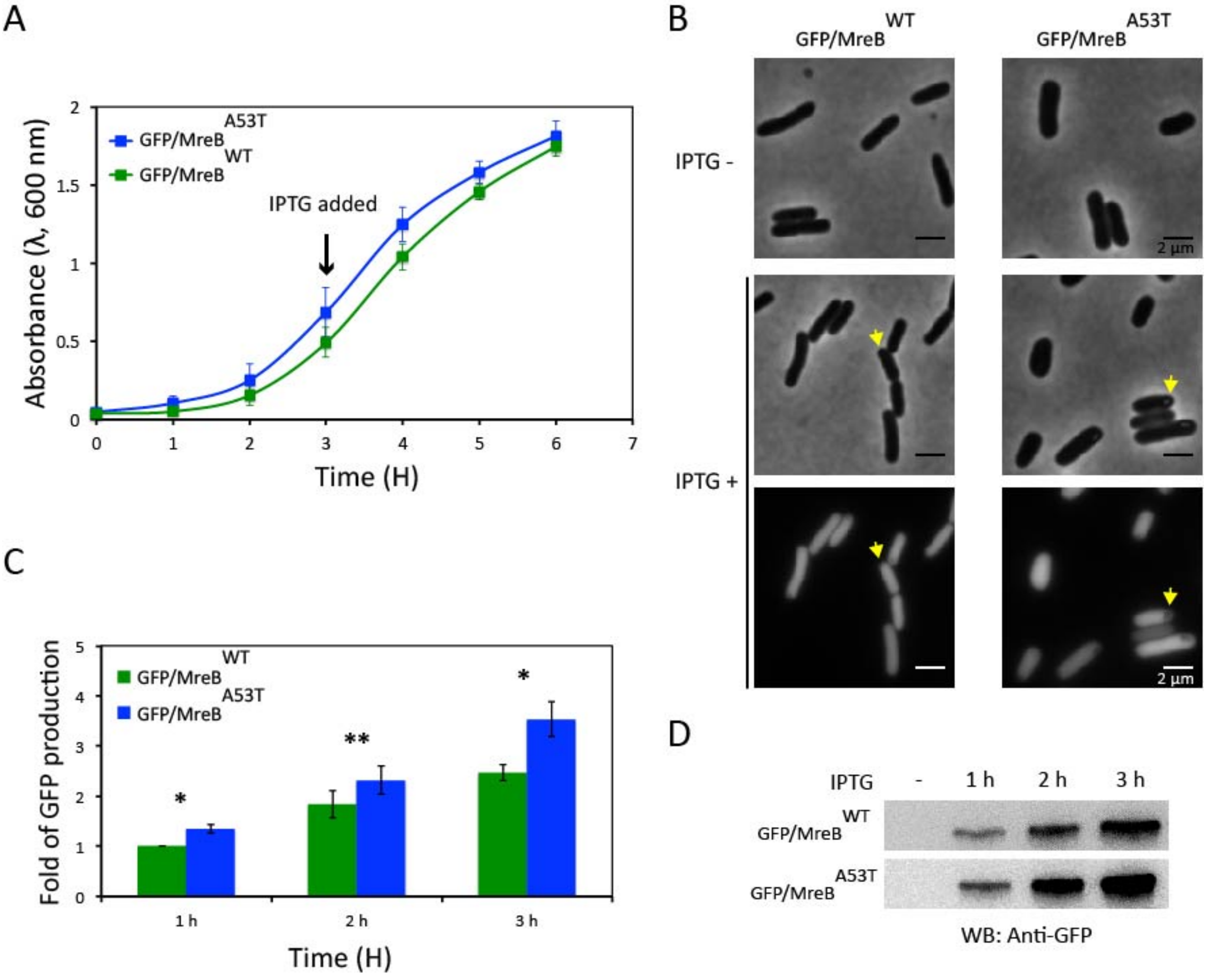
A
GFP/MreB A53T
GFP/MreB WT
IPTG added
Absorbance (λ, 600 nm)
0
0.5
1
1.5
2
0
1
2
3
4
5
6
7
Time (H)
B
GFP/MreB WT
GFP/MreB A53T
IPTG -
IPTG +
2 µm
2 µm
C
GFP/MreB WT
GFP/MreB A53T
Fold of GFP production
0
1
2
3
4
5
*
**
*
1 h
2 h
3 h
Time (H)
D
IPTG
-
1 h
2 h
3 h
GFP/MreB WT
GFP/MreB A53T
WB: Anti-GFP

**Figure 2**

**Figure 3. MreB$^{A53T}$ enhances HCAII production in *E. coli* cells.** (A) Growth curves of MreB$^{WT}$ and MreB$^{A53T}$ cells expressing HCAII from *hcaii*-pIND5. Cells were grown in LB media at 37°C with shaking. IPTG at a final concentration of 1 mM was added to cultures when they reached log phase (absorbance of ~0.4 for MreB$^{WT}$; ~0.5 for MreB$^{A53T}$, $\lambda$ = 600 nm). Mean values ± standard deviations obtained from three independent experiments are shown. (B) Images depicting the morphology of MreB$^{WT}$ and MreB$^{A53T}$ cells expressing HCAII from *hcaii*-pIND5 before IPTG induction (upper panel) and after IPTG induction for 3 h (lower panel). (C&D) HCAII expression in cells before IPTG induction at 3 h and after IPTG induction at hourly time points was verified by Western blot (WB) analysis using an anti-6X His tag antibody. HCAII expression levels were determined by quantifying the optical densitometry signal with ImageJ. HCAII expression at each time point was normalized to wild-type cells after IPTG induction for 1 h. Mean values ± standard deviations obtained from three independent experiments are shown. We analyzed the difference between the HCAII expression levels of the two strains at each time point using the Student's *t* test (two-tailed, paired). *$P < 0.05$. **$P < 0.01$.

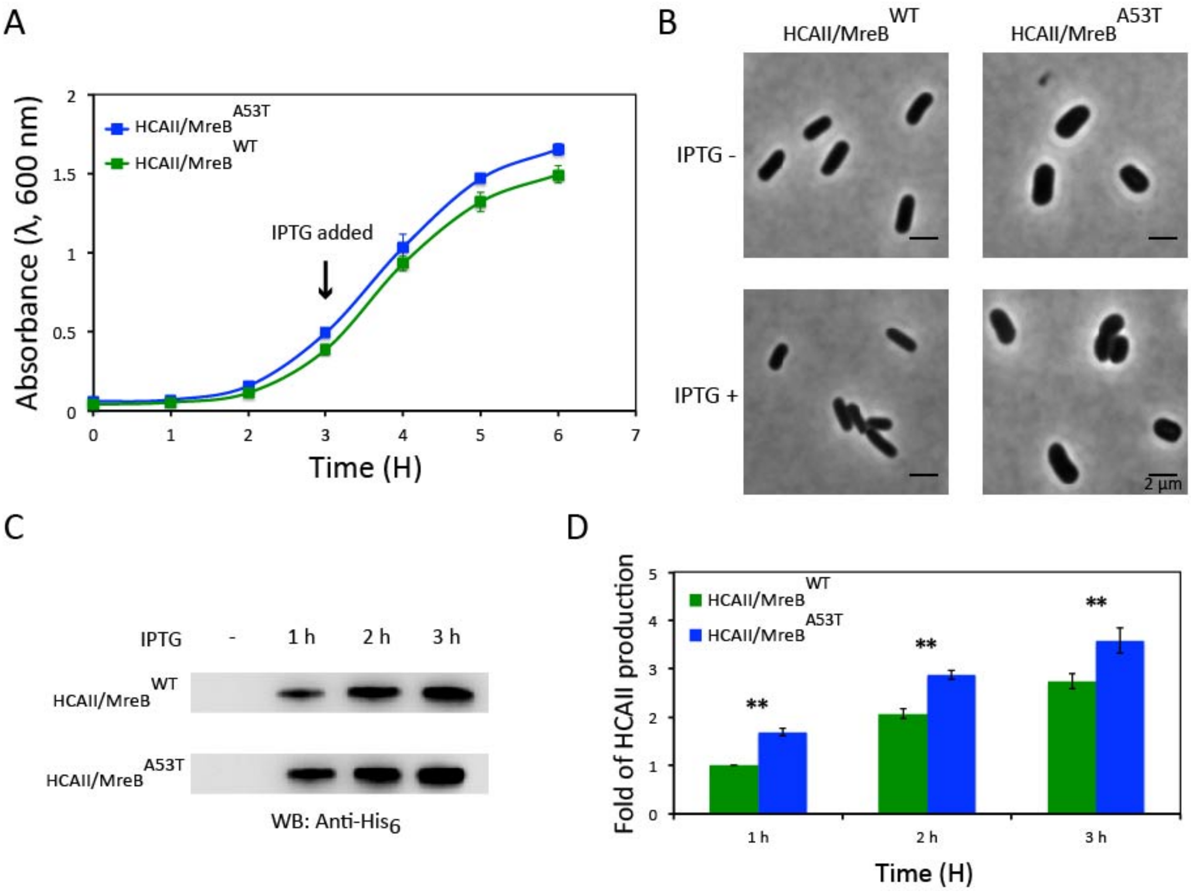
A
Absorbance (λ, 600 nm)
0
0.5
1
1.5
2
HCAII/MreB A53T
HCAII/MreB WT
IPTG added
0
1
2
3
4
5
6
7
Time (H)
B
HCAII/MreB WT
HCAII/MreB A53T
IPTG -
IPTG +
2 µm
C
IPTG
-
1 h
2 h
3 h
HCAII/MreB WT
HCAII/MreB A53T
WB: Anti-His6
D
Fold of HCAII production
0
1
2
3
4
5
HCAII/MreB WT
HCAII/MreB A53T
**
**
**
1 h
2 h
3 h
Time (H)

**Figure 3**

**Figure 4. MreB$^{A53T}$ enhances IGF-1 production in *E. coli* cells.** (A) Growth curves of MreB$^{WT}$ and MreB$^{A53T}$ cells expressing IGF-1 from *igf-1*-pIND5. Cells were grown in LB media at 37°C with shaking. IPTG at a final concentration of 1 mM was added to cultures when they reached log phase (absorbance of ~0.4 for MreB$^{WT}$; ~0.7 for MreB$^{A53T}$, $\lambda$ = 600 nm). Mean values ± standard deviations obtained from three independent experiments are shown. (B) Images depicting the morphology of MreB$^{WT}$ and MreB$^{A53T}$ cells expressing IGF-1 from *igf-1*-pIND5 before IPTG induction (upper panel) and after IPTG induction for 2 h (lower panel). Arrows indicate IGF-1 inclusion bodies. (C&D) IGF-1 expression in cells before IPTG induction at hour 4 and after IPTG induction at hourly time points was verified by Western blot (WB) analysis using an anti-6X His tag antibody. IGF-1 expression levels were determined by quantifying the optical densitometry signal with ImageJ. We normalized IGF-1 expression at each time point to expression in wild-type cells after IPTG induction for 1 h. Mean values ± standard deviations obtained from three independent experiments are shown. We analyzed the difference between the IGF-1 expression levels of the two strains at each time point using the Student's *t* test (two-tailed, paired). *$P < 0.05$. **$P < 0.01$.

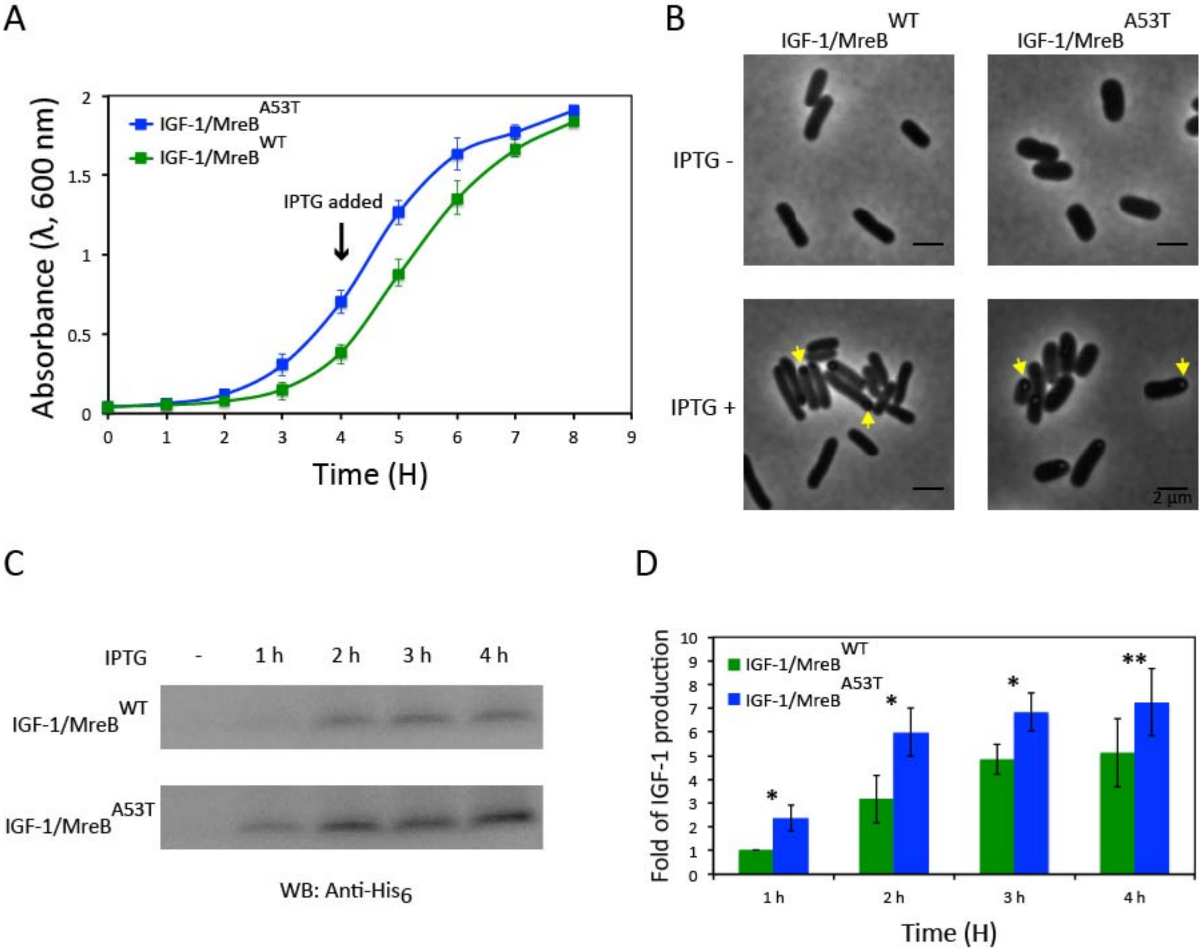
A
IGF-1/MreB^A53T
IGF-1/MreB^WT
IPTG added
Absorbance (λ, 600 nm)
Time (H)
0
0.5
1
1.5
2
0 1 2 3 4 5 6 7 8 9
B
IGF-1/MreB^WT
IGF-1/MreB^A53T
IPTG -
IPTG +
2 µm
C
IPTG
-
1 h
2 h
3 h
4 h
IGF-1/MreB^WT
IGF-1/MreB^A53T
WB: Anti-His6
D
IGF-1/MreB^WT
IGF-1/MreB^A53T
Fold of IGF-1 production
0 1 2 3 4 5 6 7 8 9 10
*
*
*
**
1 h
2 h
3 h
4 h
Time (H)

**Figure 4**

**Figure 5. The MreB$^{A53T}$ mutant enhances the production of recombinant proteins at single-cell scale.** CFUs of both MreB$^{WT}$ and MreB$^{A53T}$ cell cultures expressing the indicated proteins were counted after IPTG induction for 1 h and 3 h (GFP, HCAII), or 4 h (IGF-1). To compare how much protein a single cell produced, we normalized the protein expressions verified by Western blot analyses using CFU counts (A, B, and C). We also calculated the protein produced per unit volume by normalizing the protein produced per cell using volumes of the cells (E, F, and G). See SI for the CFU counts and cell volumes of each strain. Protein production per cell and per unit volume at each time point was normalized for wild-type cells after IPTG induction for 1 h. Shown are mean values ± standard deviations obtained from three independent experiments.

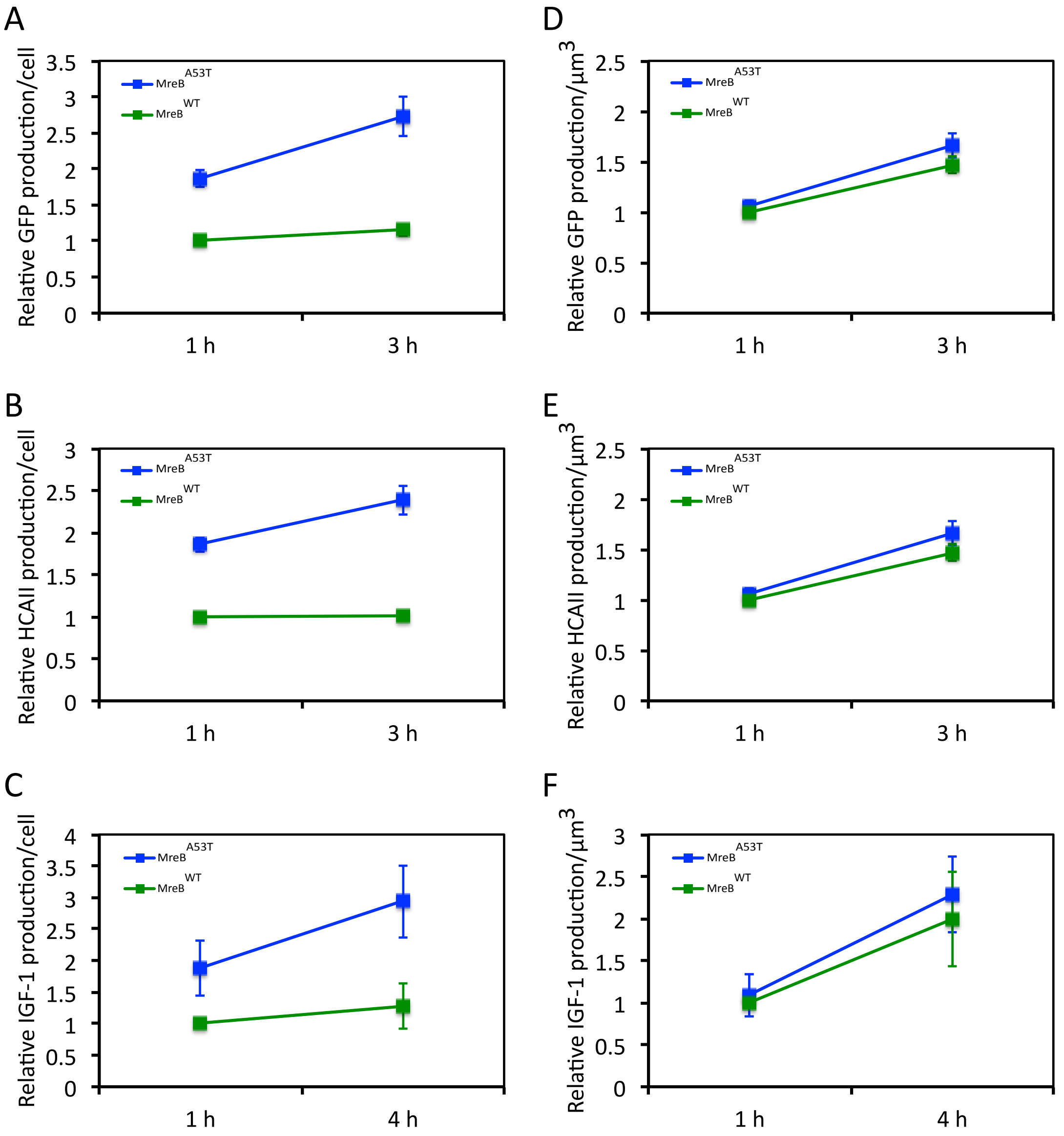
A
Relative GFP production/cell
3.5
3
2.5
2
1.5
1
0.5
0
1 h
3 h
MreB A53T
MreB WT
D
Relative GFP production/µm3
2.5
2
1.5
1
0.5
0
1 h
3 h
MreB A53T
MreB WT
B
Relative HCAII production/cell
3
2.5
2
1.5
1
0.5
0
1 h
3 h
MreB A53T
MreB WT
E
Relative HCAII production/µm3
2.5
2
1.5
1
0.5
0
1 h
3 h
MreB A53T
MreB WT
C
Relative IGF-1 production/cell
4
3.5
3
2.5
2
1.5
1
0.5
0
1 h
4 h
MreB A53T
MreB WT
F
Relative IGF-1 production/µm3
3
2.5
2
1.5
1
0.5
0
1 h
4 h
MreB A53T
MreB WT

**Figure 5**

**Table 1. Bacterial strains and plasmids used in this study**

| Strain or plasmid | Genotype or Description | Source or reference |
|---|---|---|
| *E. coli* strain | | |
| DH5α | *recA1 endA1 gyrA96 thi-1 hsdR17 supE44 relA1 deoR Δ(lacZYA-argF)U169 λ (ϕ80d lacZΔM15)* | Laboratory collection, CGSC#12384 |
| MreB$^{WT}$ | REL606. Ara(-), StrepR | KC452 |
| MreB$^{A53T}$ | REL606 with *mreB*$^{A53T}$ allele | KC453 |
| Plasmid | | |
| pIND5 | A derivative of pIND4 in which the NcoI site is replaced with an NdeI site. pIND4 is a IPTG-inducible expression vector for *R. sphaeroides* and *E. coli*, kanamycin resistance | 11, 12 |
| *gfp*-pIND5 | pIND5 containing *gfp* | This study |
| *hcaii*-pIND5 | pIND5 containing *hcaii* | This study |
| *igf-1*-pIND5 | pIND5 containing human *igf-1* | This study |

# REFERENCES

1. **Kinch MS.** 2015. An overview of FDA-approved biologics medicines. Drug Discov Today **20:**393-398.

2. **Kurland CG, Dong H.** 1996. Bacterial growth inhibition by overproduction of protein. Mol Microbiol **21:**1-4.

3. **Rosano GL, Ceccarelli EA.** 2014. Recombinant protein expression in *Escherichia coli*: advances and challenges. Front Microbiol **5:**172.

4. **Overton TW.** 2014. Recombinant protein production in bacterial hosts. Drug Discov Today **19:**590-601.

5. **Wang Y, Wu H, Jiang X, Chen GQ.** 2014. Engineering *Escherichia coli* for enhanced production of poly(3-hydroxybutyrate-co-4-hydroxybutyrate) in larger cellular space. Metab Eng **25:**183-193.

6. **Jiang XR, Wang H, Shen R, Chen GQ.** 2015. Engineering the bacterial shapes for enhanced inclusion bodies accumulation. Metab Eng **29:**227-237.

7. **Jeong KJ, Lee SY.** 2003. Enhanced production of recombinant proteins in *Escherichia coli* by filamentation suppression. Appl Environ Microbiol **69:**1295-1298.

8. **Cabeen MT, Jacobs-Wagner C.** 2005. Bacterial cell shape. Nat Rev Microbiol **3:**601-610.

9. **van Teeffelen S, Gitai Z.** 2011. Rotate into shape: MreB and bacterial morphogenesis. EMBO J **30:**4856-4857.

10. **Monds RD, Lee TK, Colavin A, Ursell T, Quan S, Cooper TF, Huang KC.** 2014. Systematic perturbation of cytoskeletal function reveals a linear scaling relationship between cell geometry and fitness. Cell Rep **9:**1528-1537.

11. **Ind AC, Porter SL, Brown MT, Byles ED, de Beyer JA, Godfrey SA, Armitage JP.** 2009. Inducible-expression plasmid for *Rhodobacter sphaeroides* and *Paracoccus denitrificans*. Appl Environ Microbiol **75:**6613-6615.

12. **Lin TY, Santos TM, Kontur WS, Donohue TJ, Weibel DB.** 2015. A Cardiolipin-Deficient Mutant of *Rhodobacter sphaeroides* Has an Altered Cell Shape and Is Impaired in Biofilm Formation. J Bacteriol **197:**3446-3455.

13. **Krishnamurthy VM, Kaufman GK, Urbach AR, Gitlin I, Gudiksen KL, Weibel DB, Whitesides GM.** 2008. Carbonic anhydrase as a model for biophysical and physical-organic studies of proteins and protein-ligand binding. Chem Rev **108:**946-1051.

14. **Takahashi Y.** 2017. The Role of Growth Hormone and Insulin-Like Growth Factor-I in the Liver. Int J Mol Sci **18**.

15. **Daegelen P, Studier FW, Lenski RE, Cure S, Kim JF.** 2009. Tracing ancestors and relatives of *Escherichia coli* B, and the derivation of B strains REL606 and BL21(DE3). J Mol Biol **394:**634-643.

16. **Zhang MM, Wang Y, Ang EL, Zhao H.** 2016. Engineering microbial hosts for production of bacterial natural products. Nat Prod Rep **33:**963-987.

17. **Jiang XR, Chen GQ.** 2016. Morphology engineering of bacteria for bio-production. Biotechnol Adv **34:**435-440.

## SUPPORTING INFORMATION

**Figure S1. Calculation for the volume of a rod-shaped *E. coli* cell.** A rod is assumed to be a central cylinder with hemispherical caps at the both ends. In this study, we used ImageJ to determine the width (W) and length (L) of an *E. coli* cell. We then calculated the cell volume (V) by the three equations listed below. $r$, radius of hemisphere. $l$, length of cylinder.

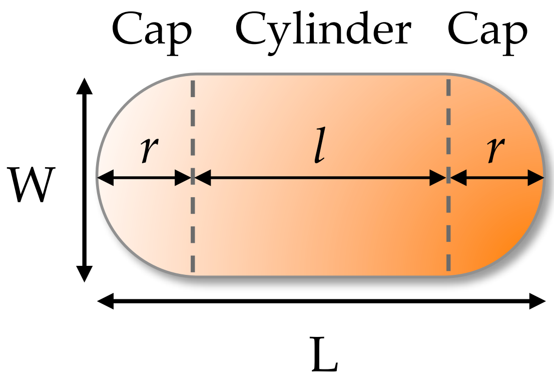

$$r \cong W/2$$

$$l = L\text{-}W$$

$$V = 1.33\pi r^3 + \pi r^2 l$$

**Figure S1**

**Figure S2. Morphology of MreB$^{WT}$ and MreB$^{A53T}$ cells expressing GFP.** Images depicting the morphology of MreB$^{WT}$ and MreB$^{A53T}$ cells expressing GFP from *gfp*-pIND5 before IPTG induction (upper panel) and after IPTG induction for 1 h and 3 h (lower panel). The table below the panel shows the cell shape parameters of the two strains. Each data point was determined by imaging 200 cells by phase-contrast bright-field microscopy and using ImageJ to determine cell width and length by which cell volume was calculated as described in Figure S1. Each data is represented as mean value ± standard deviation.

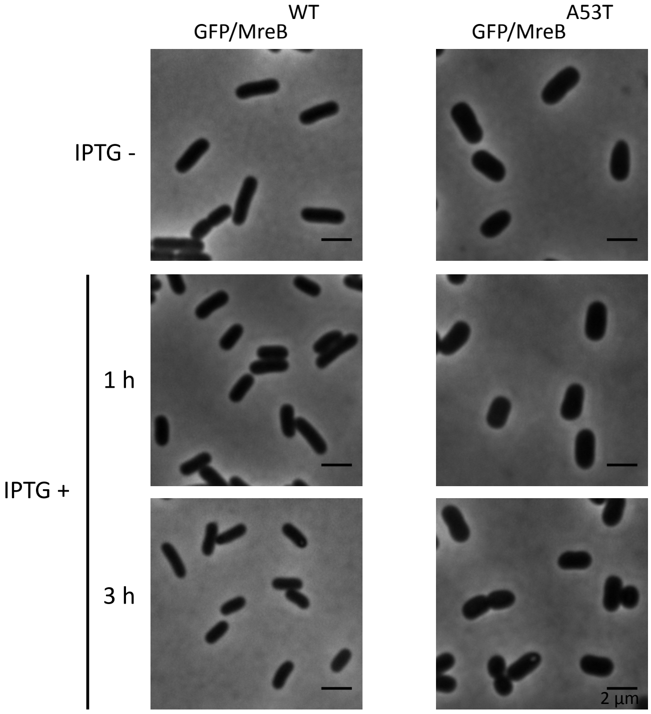

| *E. coli* strain | IPTG | Cell width (µm) | Cell length (µm) | Volume (µm$^3$) |
|---|---|---|---|---|
| MreB$^{WT}$ + *gfp*-pIND5 | − | 1.0 ± 0.0 | 3.2 ± 0.5 | 2.3 ± 0.4 |
| MreB$^{WT}$ + *gfp*-pIND5 | + (1 h) | 1.0 ± 0.0 | 2.5 ± 0.6 | 1.7 ± 0.4 |
| MreB$^{WT}$ + *gfp*-pIND5 | + (3 h) | 0.9 ± 0.1 | 2.0 ± 0.5 | 1.0 ± 0.4 |
| MreB$^{A53T}$ + *gfp*-pIND5 | − | 1.4 ± 0.1 | 2.8 ± 0.5 | 3.5 ± 0.9 |
| MreB$^{A53T}$ + *gfp*-pIND5 | + (1 h) | 1.4 ± 0.1 | 2.5 ± 0.5 | 3.0 ± 0.8 |
| MreB$^{A53T}$ + *gfp*-pIND5 | + (3 h) | 1.3 ± 0.1 | 2.0 ± 0.4 | 2.0 ± 0.5 |

**Figure S2**

**Figure S3. Morphology of MreB$^{WT}$ and MreB$^{A53T}$ cells expressing HCAII.** Images depicting the morphology of MreB$^{WT}$ and MreB$^{A53T}$ cells expressing GFP from *hcaii*-pIND5 before IPTG induction (upper panel) and after IPTG induction for 1 h and 3 h (lower panel). The table below the panel shows the cell shape parameters of the two strains. Each data point was determined by imaging 200 cells by phase-contrast bright-field microscopy and using ImageJ to determine cell width and length by which cell volume was calculated as described in Figure S1. Each data is represented as mean value ± standard deviation.

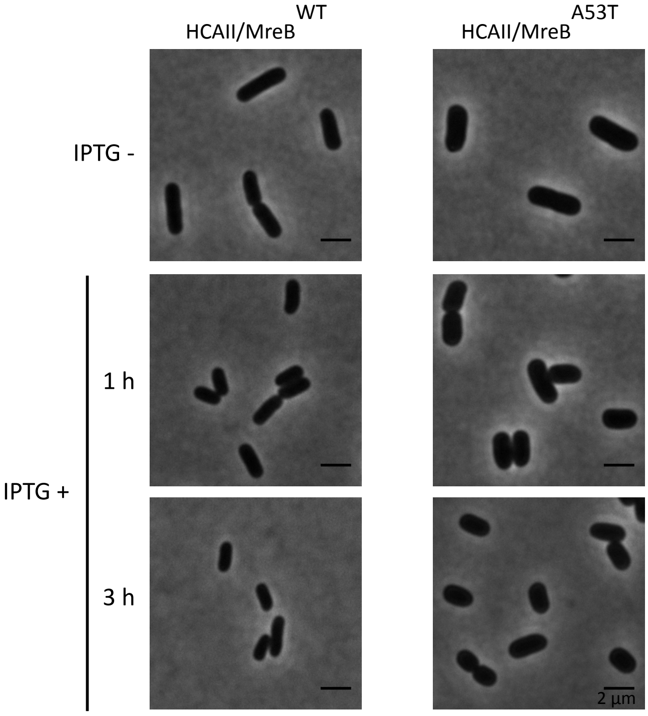

| *E. coli* strain | IPTG | Cell width (µm) | Cell length (µm) | Volume (µm$^3$) |
|---|---|---|---|---|
| MreB$^{WT}$ + *hcaii*-pIND5 | − | 1.0 ± 0.1 | 3.3 ± 0.5 | 2.4 ± 0.4 |
| MreB$^{WT}$ + *hcaii*-pIND5 | + (1 h) | 1.0 ± 0.0 | 2.5 ± 0.4 | 1.6 ± 0.3 |
| MreB$^{WT}$ + *hcaii*-pIND5 | + (3 h) | 0.9 ± 0.1 | 2.3 ± 0.5 | 1.1 ± 0.3 |
| MreB$^{A53T}$ + *hcaii*-pIND5 | − | 1.3 ± 0.1 | 3.0 ± 0.3 | 3.6 ± 0.6 |
| MreB$^{A53T}$ + *hcaii*-pIND5 | + (1 h) | 1.3 ± 0.1 | 2.5 ± 0.5 | 2.8 ± 0.7 |
| MreB$^{A53T}$ + *hcaii*-pIND5 | + (3 h) | 1.3 ± 0.1 | 2.3 ± 0.5 | 2.3 ± 0.6 |

**Figure S3**

**Figure S4. HCAII recombinant proteins produced in *E. coli* MreB$^{WT}$ and MreB$^{A53T}$ cells have the same kinetic parameters.** We purified HCAII proteins from *E. coli* MreB$^{WT}$ and MreB$^{A53T}$ cells after IPTG induction for 3 h using the Capturem™ His-Tagged Purification Miniprep Kit (Clontech) in accordance with the user manual. We determined the esterase activity of HCAII by monitoring the hydrolysis reaction of p-nitrophenyl acetate (PNPA) to p-nitrophenol (PNP). The reaction was carried out in the protein buffer (50 mM Tris-Cl, pH 8.5, 0.1 M $K_2SO_4$) with HCAII enzyme at a final concentration of 0.014 μM. The PNPA concentrations tested were 0, 0.25, 0.5, 1, 2, 4, 6, 8, and 10 mM. The rate of the reaction for each condition was obtained by measuring the absorbance of PNP at a wavelength of 405 nm per unit time ($\Delta A_{405}$/min) using spectrophotometer. The reaction for each condition was carried out in triplicate. The concentration of PNP was calculated by the Beer's Law with a molar extinction coefficient of $1.73 \times 10^4$ $M^{-1}cm^{-1}$ and an effective path length of 1.0 cm. The maximum rate $V_{max}$ and Km were obtained by Michaelis-Menten fit using GraphPad Prism 7. The rate constant $k_{cat}$ was calculated using the equation: $V_{max} = k_{cat}$ [E]. The table below shows the kinetic parameters of the HCAII recombinant proteins purified from *E. coli* MreB$^{WT}$ and MreB$^{A53T}$ cells. Each data point is represented as mean value ± standard deviation.

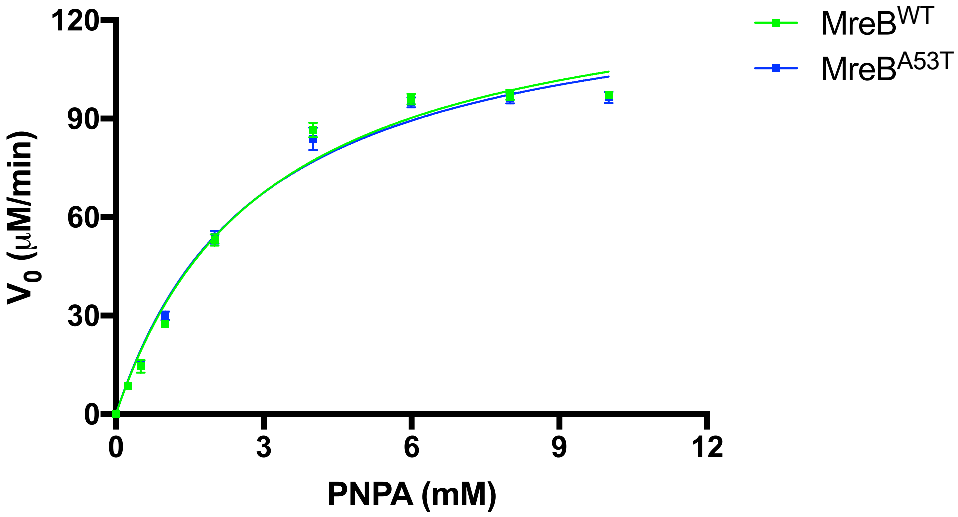

| HCAII kinetic parameters | MreB$^{WT}$ | MreB$^{A53T}$ |
|---|---|---|
| $V_{max}$ (μM/min) | 136.20 ± 10.86 | 132.60 ± 8.60 |
| Km (mM) | 3.06 ± 0.65 | 2.90 ± 0.51 |
| $k_{cat}$ (sec$^{-1}$) | 162.14 ± 12.93 | 157.86 ± 10.24 |
| $k_{cat}$/Km (mM$^{-1}$sec$^{-1}$) | 53.07 ± 4.23 | 54.45 ± 3.53 |

**Figure S4**

**Figure S5. Morphology of MreB$^{WT}$ and MreB$^{A53T}$ cells expressing IGF-1.** Images depicting the morphology of MreB$^{WT}$ and MreB$^{A53T}$ cells expressing GFP from *igf-1*-pIND5 before IPTG induction (upper panel) and after IPTG induction for 1 h and 4 h (lower panel). The table below the panel shows the cell shape parameters of the two strains. Each data point was determined by imaging 200 cells by phase-contrast bright-field microscopy and using ImageJ to determine cell width and length by which cell volume was calculated as described in Figure S1. Each data is represented as mean value ± standard deviation.

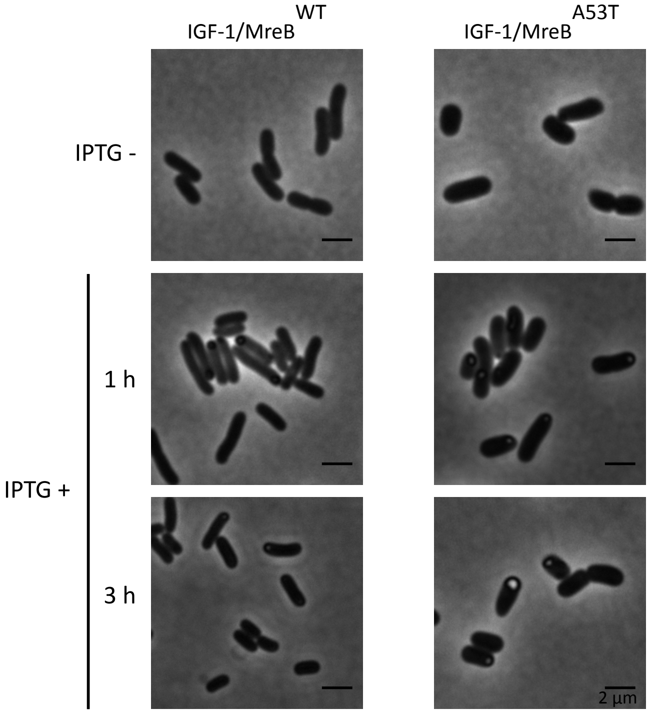

| *E. coli* strain | IPTG | Cell width (µm) | Cell length (µm) | Volume (µm$^3$) |
|---|---|---|---|---|
| MreB$^{WT}$ + *igf-1*-pIND5 | – | 0.9 ± 0.0 | 3.0 ± 0.6 | 1.8 ± 0.4 |
| MreB$^{WT}$ + *igf-1*-pIND5 | + (1 h) | 0.9 ± 0.0 | 2.4 ± 0.4 | 1.4 ± 0.3 |
| MreB$^{WT}$ + *igf-1*-pIND5 | + (3 h) | 0.8 ± 0.0 | 2.0 ± 0.4 | 0.9 ± 0.3 |
| MreB$^{A53T}$ + *igf-1*-pIND5 | – | 1.3 ± 0.1 | 2.6 ± 0.4 | 2.9 ± 0.7 |
| MreB$^{A53T}$ + *igf-1*-pIND5 | + (1 h) | 1.3 ± 0.1 | 2.2 ± 0.4 | 2.4 ± 0.6 |
| MreB$^{A53T}$ + *igf-1*-pIND5 | + (3 h) | 1.2 ± 0.1 | 1.9 ± 0.3 | 1.8 ± 0.4 |

**Figure S5**

**Table S1. CFU counts for the strains expressing GFP after IPTG induction for 1 h and 3 h.**

| *E. coli* strain | IPTG | CFU/mL ($\times 10^{8}$) |
|---|---|---|
| MreB$^{\mathrm{WT}}$ + *gfp*-pIND5 | + (1 h) | 6.5 ± 1.4 |
| MreB$^{\mathrm{WT}}$ + *gfp*-pIND5 | + (3 h) | 13.9 ± 1.6 |
| MreB$^{\mathrm{A53T}}$ + *gfp*-pIND5 | + (1 h) | 4.7 ± 1.4 |
| MreB$^{\mathrm{A53T}}$ + *gfp*-pIND5 | + (3 h) | 8.4 ± 1.1 |

**Table S2. CFU counts for the strains expressing HCAII after IPTG induction for 1 h and 3 h.**

| *E. coli* strain | IPTG | CFU/mL ($\times 10^{8}$) |
|---|---|---|
| MreB$^{\mathrm{WT}}$ + *hcaii*-pIND5 | + (1 h) | 4.4 ± 1.6 |
| MreB$^{\mathrm{WT}}$ + *hcaii*-pIND5 | + (3 h) | 12.0 ± 2.0 |
| MreB$^{\mathrm{A53T}}$ + *hcaii*-pIND5 | + (1 h) | 4.0 ± 1.7 |
| MreB$^{\mathrm{A53T}}$ + *hcaii*-pIND5 | + (3 h) | 6.6 ± 1.1 |

**Table S3. CFU counts for the strains expressing IGF-1 after IPTG induction for 1 h and 4 h.**

| *E. coli* strain | IPTG | CFU/mL ($\times 10^{8}$) |
|---|---|---|
| MreB$^{\mathrm{WT}}$ + *igf-1*-pIND5 | + (1 h) | 3.7 ± 1.3 |
| MreB$^{\mathrm{WT}}$ + *igf-1*-pIND5 | + (4 h) | 14.6 ± 1.9 |
| MreB$^{\mathrm{A53T}}$ + *igf-1*-pIND5 | + (1 h) | 4.6 ± 2.0 |
| MreB$^{\mathrm{A53T}}$ + *igf-1*-pIND5 | + (4 h) | 9.0 ± 1.2 |

**Table S4. Primers used in this study**

| | |
|---|---|
| NdeI-*gfp* | 5'-GGA GAA ATT AAC ATA TGG TGA GCA AGG GCG AGG AG-3' |
| BglII-*gfp* | 5'-GAT GGT GAT GAG ATC TCT TGT ACA GCT CGT CCA T-3' |
| NdeI-*hcaii* | 5'-AGG AGA AAT TAC ATA TGG CCC ATC ACT GGG GGT AC-3' |
| BglII-*hcaii* | 5'-GAT GGT GAT GAG ATC TTT TGA AGG AAG CTT TGA T-3' |
| NdeI-*igf-1* | 5'-AGG AGA AAT TAC ATA TGG GCC CTG AAA CTT TGT GC-3' |
| BglII-*igf-1* | 5'-GAT GGT GAT GAG ATC TGG CGG ACT TCG CCG GTT T-3' |

# CHAPTER 5

# Conclusions and Significance

## Conclusions and Significance

Van Leeuwenhoek’s microscopes ushered us into the world of bacteria and the diversity of their shape. Bacteria display a variety of shapes in nature and can change shape during their life cycle or in response to environmental changes. Cell shape has been implicated in regulating a wide range of physiological processes in bacteria, including motility, attachment, chemotaxis, virulence, and can be used as an indicator of cell health (1, 2). However, the molecular mechanisms by which bacteria control cell shape are still largely unresolved (3, 4). Understanding the molecular mechanisms underlying bacterial shape determination and the physiological relevance of cell morphology will enable a wide range of applications, including developing novel antibiotics and engineering bacterial shape for biomaterial production. This knowledge will also provide insights into biochemical principles that govern the morphology of mitochondria and other organelles in eukaryotic cells.

Microbiologists hypothesize that bacterial cell morphology is genetically encoded and bacterial cells are shaped by the orchestration of its cytoskeleton and cell wall. The cell wall is the canonical target for antibiotics that are bacterial chemotherapeutics. For example, the beta-lactam antibiotics, such as penicillin, revolutionized modern medicine by providing opportunities to kill rapidly dividing bacteria by disrupting cell wall assembly (5). The emergence of antibiotic resistance has dampened the utility of this class of antibiotics; however, the cell wall contains a large number of potential antibiotic targets that have yet to be characterized. While mitochondria evolved a different cell structure from their bacterial origins, the composition and structure of membranes in this organelle still resemble that of bacteria (6). Hence, insights into membrane structure and organization in bacteria can provide concepts of spatial membrane organization within mitochondria.

Spatiotemporal organization of bacterial membranes has been appreciated in recent years (7). Bacterial membranes contain a diverse array of lipid species that differ in head group and acyl tail (8). Similar to the membrane of mammalian cells, bacteria form raft-like membrane domains that are enriched in specific lipids. The formation of lipid domain presents a mechanism that partitions bacterial processes into specific regions of the cell at different stages of the cell cycle. This spatiotemporal compartmentalization of biochemical processes is essential for bacterial replication, growth, and many other bacterial functions (7, 9). The bacterial membrane domain is also required for the action of some antimicrobial agents (10).

Cardiolipin (CL) is an anionic phospholipid that has a large intrinsic negative curvature and forms phase-ordered lipid domains in bacterial cell membranes and mitochondrial cristae (11). These lipid domains function as landmarks for recruitment of classes of amphipathic proteins to these regions of the cell (12). In rod-shaped bacteria, CL accumulates at the cell poles and division plane due to the enhanced curvature of these cellular regions relative to the cylindrical cell body, and the localization of these curved domains is hypothesized to relax elastic stress due to membrane curvature imposed by osmotic forces and reduce the surface energy potential of this liquid crystalline material (13-15). CL domains can also be induced by the preferential interaction of CL with specific proteins and localized throughout the cell body (7, 10). CL has been shown to play important roles in diverse bacterial processes, including DNA replication, cell division, respiration, and adaptation to environmental stress (7, 16).

*Rhodobacter sphaeroides* is a rod-shaped, Gram-negative, photosynthetic bacterium member of the class $\alpha$-proteobacteria. When exposed to a reduction in oxygen tension, *R. sphaeroides* develops invaginations in its cytoplasmic membrane and forms intracytoplasmic vesicles referred to as chromatophores (17). These vesicles contain the fully assembled machinery required for photosynthesis, suggesting that this process is coupled to a mechanism for sorting membrane proteins and localizing them to the membrane site where vesicle formation occurs (18). This dramatic physiological overture requires local changes in membrane curvature, which suggests that this organism has an intrinsic biochemical system for membrane remodeling. In this dissertation, we used a multidisciplinary set of techniques from genetics, biochemistry, and chemical biology to elucidate the cellular requirement for CL and its role in determining cell shape in the model bacterium *R. sphaeroides*.

In Chapter 2, we observed that a CL deficiency in *R. sphaeroides* causes a change in the shape of cells and impairs biofilm formation. We built a new connection between CL and cellular adaptation in *R. sphaeroides*. We demonstrated that CL plays a role in regulating *R. sphaeroides* morphology and is important for the ability of this bacterium to form biofilms. This study correlates CL concentration, cell shape, and biofilm formation and provides the first example of how membrane composition in bacteria alters cell morphology and influences adaptation. This study also provides insights into the potential of phospholipid biosynthesis as a target for new chemical strategies designed to alter or prevent biofilm formation.

In Chapter 3, we continued on investigating the molecular mechanisms that connect membrane composition to cell morphology using *R. sphaeroides* as a model bacterium. Bacterial cells are outlined by a meshwork of peptidoglycan (PG), which constitutes the cell wall and has been the canonical target for antibiotics. We found that CL plays a role in bacterial cell shape determination by regulating PG precursor biosynthesis. A CL deficiency in *R. sphaeroides* not only alters cell morphology, but also increases its sensitivity to antibiotics targeting proteins involved in PG synthesis. This study suggests CL biosynthesis as a new target for bacterial chemotherapeutics.

In Chapter 4, we developed a new method for maximizing recombinant protein production in bacteria. We observed that *Escherichia coli* cells with specific point mutations in MreB have an increased cell volume. We found that an MreB point mutant (A53T) of *E. coli* is 150% larger in cell volume compared to wild-type cells, yet they have a similar growth rate. Using a conventional expression system based on a high-copy number plasmid containing a target gene of interest under control of the *lac* promoter, we demonstrated that this mutant produces 30-40% more protein produced per unit time than wild-type cells. In principle, this approach can be applied to a range of overexpression strains of bacteria that are used for recombinant protein production.

A number of cell shape determinants have been identified and their functions have been well studied in bacteria (3, 4). Those shape determinants are mostly membrane-associated proteins that convey shape information across the cytoplasmic membrane. In this perspective, the lipid bilayer is just a structurally passive solvent that does not influence cell shape. This dissertation provides evidence that the cell membrane itself can possess shape information, regulate cell shape determination, and in turn regulate bacterial functions. These findings will provide insights into the study of parallel conserved mechanisms in other microbes and the development of novel antibiotic targets.

# REFERENCES

1. **Young KD.** 2006. The selective value of bacterial shape. Microbiol Mol Biol Rev **70:**660-703.

2. **Yang DC, Blair KM, Salama NR.** 2016. Staying in Shape: the Impact of Cell Shape on Bacterial Survival in Diverse Environments. Microbiol Mol Biol Rev **80:**187-203.

3. **Cabeen MT, Jacobs-Wagner C.** 2005. Bacterial cell shape. Nat Rev Microbiol **3:**601-610.

4. **van Teeffelen S, Renner LD.** 2018. Recent advances in understanding how rod-like bacteria stably maintain their cell shapes. F1000Res **7:**241.

5. **Holten KB, Onusko EM.** 2000. Appropriate prescribing of oral beta-lactam antibiotics. Am Fam Physician **62:**611-620.

6. **Gohil VM, Greenberg ML.** 2009. Mitochondrial membrane biogenesis: phospholipids and proteins go hand in hand. J Cell Biol **184:**469-472.

7. **Lin TY, Weibel DB.** 2016. Organization and function of anionic phospholipids in bacteria. Appl Microbiol Biotechnol **100:**4255-4267.

8. **Sohlenkamp C, Geiger O.** 2016. Bacterial membrane lipids: diversity in structures and pathways. FEMS Microbiol Rev **40:**133-159.

9. **Barak I, Muchova K.** 2013. The role of lipid domains in bacterial cell processes. Int J Mol Sci **14:**4050-4065.

10. **Epand RM, Epand RF.** 2009. Domains in bacterial membranes and the action of antimicrobial agents. Mol Biosyst **5:**580-587.

11. **Mileykovskaya E, Dowhan W.** 2009. Cardiolipin membrane domains in prokaryotes and eukaryotes. Biochim Biophys Acta **1788:**2084-2091.

12. **Renner LD, Weibel DB.** 2011. Cardiolipin microdomains localize to negatively curved regions of *Escherichia coli* membranes. Proc Natl Acad Sci U S A **108:**6264-6269.

13. **Mileykovskaya E, Dowhan W.** 2000. Visualization of phospholipid domains in *Escherichia coli* by using the cardiolipin-specific fluorescent dye 10-N-nonyl acridine orange. J Bacteriol **182:**1172-1175.

14. **Kawai F, Shoda M, Harashima R, Sadaie Y, Hara H, Matsumoto K.** 2004. Cardiolipin domains in *Bacillus subtilis* marburg membranes. J Bacteriol **186:**1475-1483.

15. **Huang KC, Mukhopadhyay R, Wingreen NS.** 2006. A curvature-mediated mechanism for localization of lipids to bacterial poles. PLoS Comput Biol **2:**e151.

16. **Wood JM.** 2018. Perspective: challenges and opportunities for the study of cardiolipin, a key player in bacterial cell structure and function. Curr Genet doi:10.1007/s00294-018-0811-2.

17. **Chory J, Donohue TJ, Varga AR, Staehelin LA, Kaplan S.** 1984. Induction of the photosynthetic membranes of *Rhodopseudomonas sphaeroides*: biochemical and morphological studies. J Bacteriol **159:**540-554.

18. **Geyer T, Helms V.** 2006. A spatial model of the chromatophore vesicles of *Rhodobacter sphaeroides* and the position of the Cytochrome bc1 complex. Biophys J **91:**921-926.